Université d'Ottawa · University of Ottawa

Université d'Ottawa · University of Ottawa

FACULTÉ DE ÉTUDES SUPÉRIEURES ET POSTDOCTORALES

FACULTY OF GRADUATE AND POSTDOCTORAL STUDIES

Ishuwa SIKANETA

AUTEUR DE LA THÈSE - AUTHOR OF THESIS

Ph. D (Electrical Engineering)

GRADE - DEGREE

School of Information Technology and Engineering

FACULTÉ, ÉCOLE, DÉPARTEMENT - FACULTY, SCHOOL, DEPARTMENT

TITRE DE LA THÈSE - TITLE OF THE THESIS

Detection of Ground Moving Objects with Synthetic Aperture Radar

J-Y. Chouinard

DIRECTEUR DE LA THÈSE - THESIS SUPERVISOR

CO-DIRECTEUR DE LA THÈSE - THESIS CO-SUPERVISOR

EXAMINATEURS DE LA THÈSE - THESIS EXAMINERS

M. Bouchard

F. Danilo-Lemoine

R. Dansereau

M. Davis

J.-M. De Koninck, Ph.D.

LE DOYEN DE LA FACULTÉ DES ÉTUDES SUPÉRIEURES ET POSTDOCTORALES

DEAN OF THE FACULTY OF GRADUATE AND POSTDOCTORAL STUDIES

DETECTION OF GROUND MOVING OBJECTS WITH SYNTHETIC APERTURE RADAR

by

ISHUWA C. SIKANETA

A thesis submitted to the Faculty of Graduate and Postdoctoral Studies
of the University of Ottawa in partial fulfillment of the requirements
for the degree of Doctor of Philosophy

DOCTOR OF PHILOSOPHY

December 13, 2004

Ottawa-Carleton Institute for Electrical and Computer Engineering
School of Infromation Technology and Engineering
Faculty of Engineering, University of Ottawa
Ottawa, Ontario, Canada

Your file Votre référence
ISBN: 0-494-01760-0
Our file Notre référence
ISBN: 0-494-01760-0

To my wife Tinda who, with a great deal of patience, kept me motivated.

ACKNOWLEDGEMENTS

Thanks to the Radar Systems section at Defence Research and Development – Ottawa for the opportunity and assistance to complete this thesis. Thanks to Dr. Chuck Livingstone for steering me through. Thanks to Dr. Christoph Gierull for discussions and mentoring. Last, but not least, thanks to my supervisor Dr. Jean-Yves Chouinard for guidance, motivation and support.

ABSTRACT

This thesis investigates Ground Moving Target Indication (GMTI) using a multi-aperture Synthetic Aperture Radar (SAR). GMTI relevant methods to process the SAR data collected from a strip-map system are presented. Techniques for mitigation of processing ambiguities are proposed, and a map-drift based automatic focus algorithm for the moving targets is developed. Target detectors based on the multi-channel covariance matrix are presented. Comparisons of the proposed detectors with classical methods, such as Displaced Phase Centre Antenna (DPCA), or Along Track Interferometry (ATI), show increased capability in non-ideal terrain types. By decomposing the complex Wishart probability distribution of the covariance matrix into probability distributions of the eigenvalues and eigenvectors, we derive the receiver operating characteristics (ROCs) of the new detection metrics in ideal terrain. The complete analysis is presented for a two-channel system as well as for special cases of the three-channel system. Finally, since implementation of the Constant False Alarm Rate (CFAR) detectors using the new metrics requires estimation of the local scene parameters, a new parameter estimation method is presented. This parameter estimation technique suggests an extension of the current statistical model of the SAR data; an extension that is also examined.

TABLE OF CONTENTS

LIST OF TABLES

LIST OF FIGURES

LIST OF SYMBOLS

LIST OF ABBREVIATIONS

CHAPTER 1
INTRODUCTION

1.1 Problem statement and motivation

Both civilian and military engineers harbour interest in Ground Moving Target Indication (GMTI). In the civilian world, the engineering of highways and law enforcement represent potential applications, while for the military, the applications really need no explanation. An appealing technology for GMTI is multi-channel Synthetic Aperture Radar (SAR). SAR has the capability to monitor large areas of interest, the advantage (militarily) of large stand-off distances between the sensor and the area of interest, the natural placement of moving targets into a simultaneously generated image representing the scene, and, the capability to operate not only at night, but also through cloud cover. These advantages make a convincing case for their construction.

Along with the construction of the physical system comes the requirement to implement a system processor. Indeed, a single-channel SAR faithfully collects data that is of no consequence unless it is processed with the appropriate compression algorithms to produce a RADAR image. The multi-channel SAR-GMTI must thus process its data to produce not only the SAR image, but the GMTI information. GMTI information in this thesis is defined as the velocity vector, the time, and the position of a target along with its scene context.

Ideally, GMTI data should be processed automatically, along with indications of the quality of the information. Accurate statistical models of the SAR data are critical to realize these desires.

1.2 Thesis contributions

This thesis presents theory and algorithms to extract GMTI data from a multi-channel SAR. Among the contributions are:

- Adaptation of an autofocus algorithm for moving targets. The algorithm is based upon the well known method of map-drift [FL99].
- Application of "deramp" chirp signal processing for the detection of moving targets. This method, also known as spectral analysis (SPECAN), is not generally used for strip-map SAR

but has a great advantage over conventional SAR processing in that it naturally separates moving targets from clutter and requires less processing time.

- Definition of new detection metrics using the elements of an eigenvalue/eigenvector decomposition of the multi-channel covariance matrix. Both the eigenvalues and a novel representation of the eigenvectors are used as moving target detection metrics. The representation of the eigenvectors uses a parameterization of the Haar measure of unitary matrices. It is demonstrated that the best choice of metric depends on the type of terrain imaged by the SAR, thereby providing heretofore impossible detection flexibility.

- By simultaneously decomposing the Wishart probability distribution for complex covariance matrices, the probability distributions of both the eigenvalues and the representation of the eigenvectors are determined. Both the joint distributions and the marginal distributions are given. It is believed that this is the first time that the distributions for the eigenvalues appears in the literature without the use of zonal polynomials. Further, it is believed that the probability distribution of this representation of the eigenvectors makes its debut in this thesis. The probability distributions have application in other areas of science and engineering such as Rayleigh fading in multi-antenna channels [Gra02], or random graph theory [Ede89].

- Recombination of the decomposition elements leads to the construction of new, powerful nonlinear detection methods that provide capability in previously challenging terrain. The proposed adaptive hyperbolic and eigenprojection detectors have the capability to detect moving targets in such areas as urban terrain where conventional metrics such as the displaced phase centre antenna (DPCA) suffer due to false alarm constraints.

- A new powerful parameter estimation method based upon the moments of the cross-channel phase is presented. These estimated parameters are required for the calculation of constant false alarm (CFAR) thresholds. The technique not only simultaneously and quickly estimates all required parameters, but also estimates "effective" parameters in situations where the model of the statistical distribution for the SAR data is not valid[1]. In a sense, the technique allows for an analytic continuation of the set of valid parameters that describe the probability density function of the representation of the covariance matrix eigenvectors. It is demonstrated, in these situations, that the histograms of the unitary matrix representation parameters are accurately described by evaluating the theoretical probability distributions on the extended

[1] Where the assumptions that lead to the complex Wishart distribution fail.

set. This result allows for the implementation of a CFAR detector even in cases where the underlying statistical model fails.

- Proposal of a generalized inverse chi-squared texture statistic in cases of terrain inhomogeneity as well as methods to estimate the parameters of this statistic.

1.3 Thesis organisation

Following a literature review in chapter 2, the processing of SAR data for GMTI is presented in chapter 3. Chapter 4 presents new metrics for moving target detection after processing using an eigenvalue/eigenvector transformation of the sample covariance matrix. Chapter 5 discusses deviation from the homogeneous model and proposes a generalised inverse chi-square texture statistic to address cases of heterogeneity. Chapter 6 discusses a new approach for the estimation of parameters required for the implementation of an automatic constant false alarm rate (CFAR) detector. Estimation algorithms are proposed both for the statistics of the homogeneous metrics and the texture statistic of chapter 5. These ideas are all collected and applied to a real example of moving target detection in chapter 7. Along with the example using measured two-channel SAR data, the probabilities of target detection given signal to clutter ratios and target speeds are presented for each proposed metric. Finally, a conclusion in chapter 8, summarises the thesis results. For the sake of readability, most of the mathematical developments are moved to the trailing appendices.

CHAPTER 2
LITERATURE REVIEW

2.1 Overview

This chapter presents a summary of the literature on three topics pertinent to the problem of Ground Moving Target Identification (GMTI) using Synthetic Aperture Radar (SAR). The three topics include:

- SAR processing algorithms for GMTI
- The statistics of multi-channel SAR
- Implementation of automatic methods for GMTI

2.2 SAR processing for Moving Targets

An imaging radar system illuminates terrain with pulses of electromagnetic (EM) radiation and then measures and processes the pulse echoes to form an image. Radars are capable of measuring the reflectivity of the terrain, the phase of the response, the position of elements in the terrain, and the polarization response of targets in the terrain [HL98]. Some of the defining characteristics of a radar system are the signal wavelength, the polarization, the power, the antenna length, and the signal bandwidth. Typically, military radars are high-resolution, small-coverage-area designed, and aim to image hard targets like vehicles or other man-made structures, while civilian earth-observation radars possess low-resolution, large-coverage-area capability, and measure structures such as fields, ice floes and mountain ranges.

In its entirety, an imaging system is composed of a radar with a particular design, the terrain with particular response characteristics, and the imaging geometry. Here geometry refers not only to the spatial model, but also on how the model evolves temporally: we refer to it as a 4D geometry. In one mode, called strip-map mode, the system maintains the look direction of the radar with respect to the platform flight path and images a large area at low resolution. In another mode, termed spotlight mode, the system keeps its antenna trained on a target of interest (while it can) thus increasing the imaging resolution at the expense of a reduced coverage area.

The geometric differences between a satellite platform and an aerial platform are quite pronounced. A satellite will be at a much greater distance from its target and moving much more rapidly than an aircraft. For instance, Radarsat-2 will be $\approx$ 800,000 m above the earth travelling at 7,500 m/s [Chi00], while the General Atomics Unmanned Aerial Vehicle (UAV), called the Gnat, has a maximum altitude of 7,600 m and travels at speeds between 18 and 72 m/s [Mun00]. In concert with the platform velocity and altitude is another important temporal parameter, the Pulse Repetition Frequency (PRF), f_p, which provides the mechanism for creating the azimuthal dimension of the image.

For a side looking radar, the image formation space is defined by two "almost" orthogonal dimensions, the range dimension and the azimuthal dimension. The azimuthal dimension has a corresponding physical basis vector in the direction of flight of the radar, while the range dimension has a corresponding real basis vector in the direction that the radar antenna points. The qualifier "almost" is used because in reality, the contour of constant range on a flat earth is defined by the intersection of a sphere and a flat plane giving rise to arcs which curve into the azimuthal dimension.

2.2.1 Conventional GMTI techniques

Consider a target situated on an infinite, flat, surface and suppose that a radar, located above the surface, sends out coherent, large-bandwidth pulses at some pulse repetition frequency (PRF) while it moves along its track as illustrated in figure 2.1. At some point in "slow time" (time on the scale of the interval between pulses), a pulse will reflect off the target and return to the radar [Sou99]. The reflected pulse is measured as an amplitude, *e.g.* an induced voltage, and a phase. In the absence of sensor noise, the phase of the measured pulse depends only on the radar wavelength and the distance between the target and the radar. The time required for the pulse to travel from the radar to the target and back again at the speed of light is measured on the "fast time" scale. On the fast time scale, radar motion is small enough to consider it stationary, even for a radar on a satellite platform, [Sou99]. The measured reflected signal can be represented by the complex quantity

$$z_1(t) = A(t)e^{-j2\pi/\lambda\ 2r(t)}, \tag{2.1}$$

where t is the slow time at which the measurement is made, λ is the radar wavelength, $A(t)$ is the amplitude of the reflection, and $2r(t)$ is the length of the route taken by the pulse, there and back. We model $z_1(t)$ as a complex zero-mean stationary Gaussian process. Justification for this model can be found in [GS02, Gie01a, JWP94].

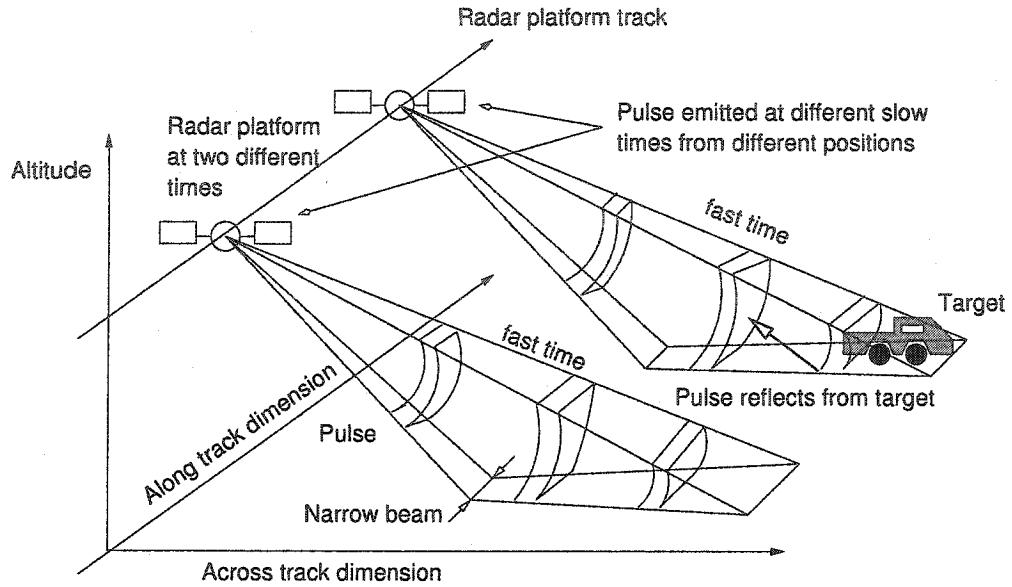

Figure 2.1. Side-looking radar geometry.

Now imagine that after a short period of time, Δt, the measurement is repeated with the radar at the same location as before. A system with two identical antennas oriented along the radar platform velocity vector can perform such time dislocated but space co-located measurements by dragging the trailing antenna into the former position of the leading antenna. The time between measurements is a function of d, the distance between the antennas, and v_p, the speed of the platform, defined by $\Delta t = d/v_p$. The signal measured by the second antenna will be

$$z_2(t + \Delta t) = A(t + \Delta t)e^{-j2\pi[2r(t+\Delta t)/\lambda]}, \tag{2.2}$$

where $r(t + \Delta t)$ may be different from $r(t)$ due to target motion. The phase and amplitude of $z_1(t)z_2^*(t+\Delta t)$, where $*$ denotes complex conjugation, are called the along-track interferometric (ATI) phase and the along-track interferometric amplitude, respectively, [FL99, Sou99]. For a stationary target, also called clutter, the ATI phase will be zero because $r(t) = r(t+\Delta t)$. A non-zero ATI phase indicates that the target is moving. In practice, however, slight differences between measurements and the addition of thermal noise can also cause the ATI phase to be non-zero. The ATI phase sample can be modelled as a random variable with zero mean[1]. The variance of the phase sample

[1] Zero-mean assumes that the underlying background clutter is stationary. On sea surfaces, for instance, the clutter has a certain self motion and the ATI phase may be non-zero mean.

defines a limit on the lowest speed at which a target is detectable since the ATI phase is proportional to target across-track speed. An automatic constant false alarm rate (CFAR) ATI phase detector can be realized by computing an appropriate phase threshold given the tolerable rate of false alarm. Computation of the threshold requires knowledge of the ATI phase statistics. Implementation of this automatic phase detector has been examined in [Gie01a].

In practice, contrary to figure 2.1, the radar sees many targets on the surface; however, the principle of superposition permits the sum of many isolated target models, with targets in different locations, to approximate the real situation. Aligning columns of fast time samples from each pulse leads to a complex radar matrix of the terrain. The slow time resolution, *i.e.* the minimum along-track distance between two targets such that they are sampled at different slow times, depends on the along-track width of the radar beam. The along-track angular width of the beam, in turn, depends upon the physical length of the antenna, [Sou99, FL99]. A longer antenna can create a narrower beam and better resolution. Unfortunately, a long antenna is more difficult to implement than a short antenna. A synthetic aperture radar (SAR) uses a wide beam to collect many slow time samples of each target and then synthesizes a narrow beam by filtering the raw radar data matrix after data collection. The slow time (also known as azimuth or Doppler) filtering is implemented on the rows of the raw radar data matrix to create a complex compressed (also called focused) radar data matrix. Whether filtered or not, plotting the absolute value of each complex sample using the row and column values as $x - y$ coordinates leads to the radar image. This image is called the raw radar image or the compressed radar image accordingly.

In along-track interferometry, two matrices are created, the first with samples of the terrain taken from the leading antenna, the second with samples taken from the trailing antenna. The second matrix may be interpolated to approximate the condition that for each element, the antennas measured the terrain from the same spatial locations at different times. These two complex valued matrices are slow time SAR filtered and combined into the interferogram by element-wise multiplication of the first matrix by the complex conjugate of the second. It should be noted that slow time filtering is not essential for GMTI, [GS03]. In a process known as multi-looking, n statistically independent neighbouring samples of the interferogram are low-pass filtered to reduce the clutter variance, thereby increasing the minimum detectable velocity [GS02]. This filtering can occur in either or both of the slow time and fast time directions, and has the unfortunate effect of reducing resolution, thus making small moving targets more difficult to detect. The low-pass filtering is often a moving average, and implementation of a CFAR detector requires computation of the statistics of the averaged or multi-looked interferogram.

The capability to detect moving targets hinges on the ability to distinguish these targets from stationary clutter. This can be achieved by performing some transformation of the data and looking for targets in clutter free regions, or enhancing the target to clutter ratio by supressing the clutter. In another GMTI technique, discussed in [LSG+02, Chi03], the slow time clutter signal is oversampled with the radar PRF. Due, mainly, to across-track target motion, the spectrum of a moving target Doppler shifts away from the clutter band. An automatic implementation of this algorithm involves identifying the clutter free spectral region and bandpass filtering the data. The residue data can then be SAR processed and thresholded in power [LSG+02].

With a multi-aperture system (also called a multi-antenna or multi-channel), clutter suppression can be achieved by making use of the correlation properties between acquisitions by each aperture. In the SAR Space Time Adaptive Processing method, (SAR-STAP) the k-channel clutter covariance matrix is adaptively estimated, inverted, and applied to the aggregate clutter plus target signal, [Bar92, Gie97, Kle98].

2.2.2 Fast-time resolution

Without going into much detail, image formation in the range direction is done by range-gating, or sampling, the returned echo followed by signal processing to provide compression gain [FL99]. Thus, in the simplest case, for each pulse echo, targets that are further from the radar are gated at a later time than targets closer to the radar. Since the gate spacing is on the order of the speed of propagation of the radiation, c, it is sometimes called the "fast-time" dimension. The range resolution is related to the bandwidth of the pulse [FL99, OQ98].

2.2.3 Slow-time resolution

Image formation in the azimuthal direction, or "slow-time" dimension, however, can be done in two ways leading to two classes of imaging radars; first, to Side Looking Aperture Radars (SLAR's)[2], and second, to Synthetic Aperture Radars (SAR's).

A SLAR creates the azimuth response based on the power contained in the pulse that has been range-gated. Thus the azimuth response is a function of the magnitude of the coherent integration of all targets illuminated by the antenna in the azimuth direction over a particular range interval. As shown in figure 2.2, for larger ranges, the azimuth beam covers more targets leading to range dependent degradation in the azimuth resolution.

[2]Also referred to as Real Aperture Radars (RAR's).

A SAR, on the other hand, records the complex range-gated response and post-process many received pulses to provide superior azimuth resolution. In both cases, the azimuth resolution is proportional to the beamwidth of the antenna in the azimuth direction which in turn is inversely related to the length of the antenna [FL99, UMF86].

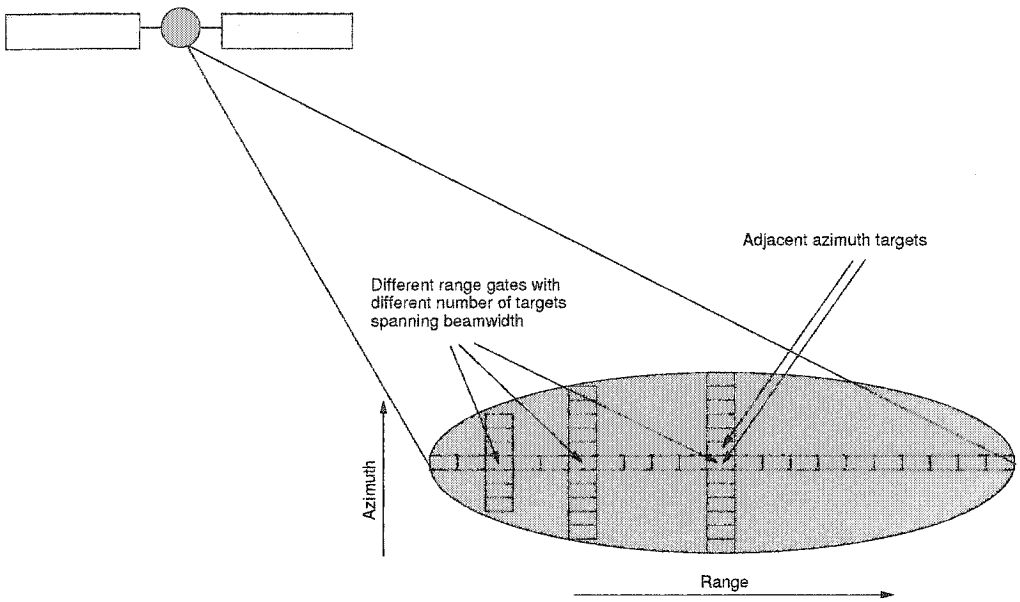

Figure 2.2. SAR dimensions.

Each SAR pulse is a measurement of the complex response of the echoes of many targets. These measurements are combined to increase azimuth resolution by noting, as illustrated in figure 2.3, that since the radar is moving, the distance, $r(t)$, between the radar and a given target evolves over time. Therefore, for a target denoted by l, the phase of the scattered echo, $\theta_l(t)$, which is some function of the range to target, $\theta_l(t) = f[r_l(t)]$, also evolves. If $\theta_l(t)$ is known, then the inner product of the complex exponential of the recorded ensemble of phases,

$$\theta^{ens}(t) \equiv \theta_l(t) + \sum_{i=-M, i\neq 0}^{M} \theta_{l-i}(t), \tag{2.3}$$

(target of interest plus $2M$ interfering signals) with the complex exponential of $\theta_l(t)$, is

$$d_l = < e^{j\theta^{ens}(t)}, e^{-j\theta_l(t)} > = \int_{-\infty}^{\infty} e^{j\theta^{ens}(t)} e^{-j\theta_l(t)} dt \tag{2.4}$$

which is proportional to the target response.

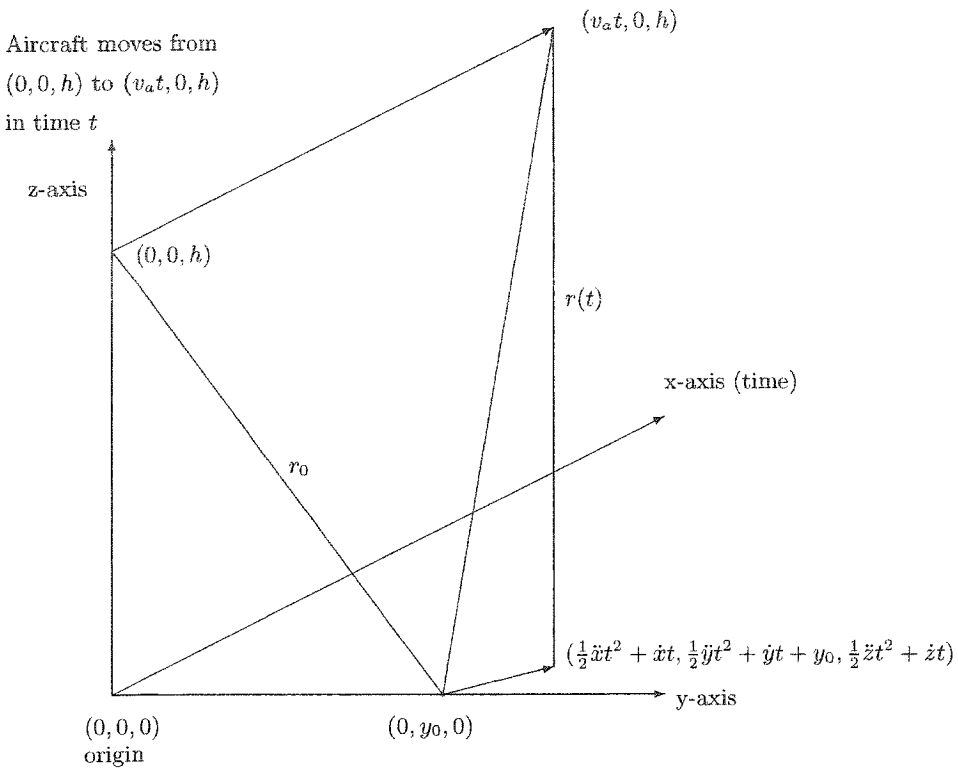

Figure 2.3. The geometry of a moving target.

The range history, $r(t)$, not only depends on the radar platform velocity, altitude and flight path, but also on the target position on the terrain as a function of time, as shown in figure 2.3. Typically, a SAR will be designed to image a target that does not move and typically, in strip-map mode, the phase histories of adjacent targets in azimuth, falling into the same range-gate, will have the same phase history function with one being a delayed version of the other:

$$\theta_{l+1}(t) = \theta_l(t+\tau), \tag{2.5}$$

where τ is the time it takes the aircraft to move the distance between the two targets. Thus, in a typical situation, the azimuth response at a given range is given by

$$d(t_0) = \int_{-T}^{T} f^{ens}(t_0+t)w(t)e^{-j\theta(t)}dt, \tag{2.6}$$

where $f^{ens}(t)$ is the recorded signal (the coherent sum of the responses from many targets), $2T$ is the time that it takes for the beam to sweep across the target, and $w(t)$ is some appropriately designed weighting function. The correlation in (2.6) is called azimuth compression or azimuth focusing and can be readily computed using Fast Fourier Transform (FFT) techniques, although it can be done in other ways as well. One interesting and intuitive method for computing (2.6) is done with optics. If the signal is recorded onto holographic film, and a lens is appropriately fashioned to represent the phase history function, then the image is created by passing coherent light through the bottom of the film and then through the lens as illustrated in figure 2.4 [Hov80, UMF86].

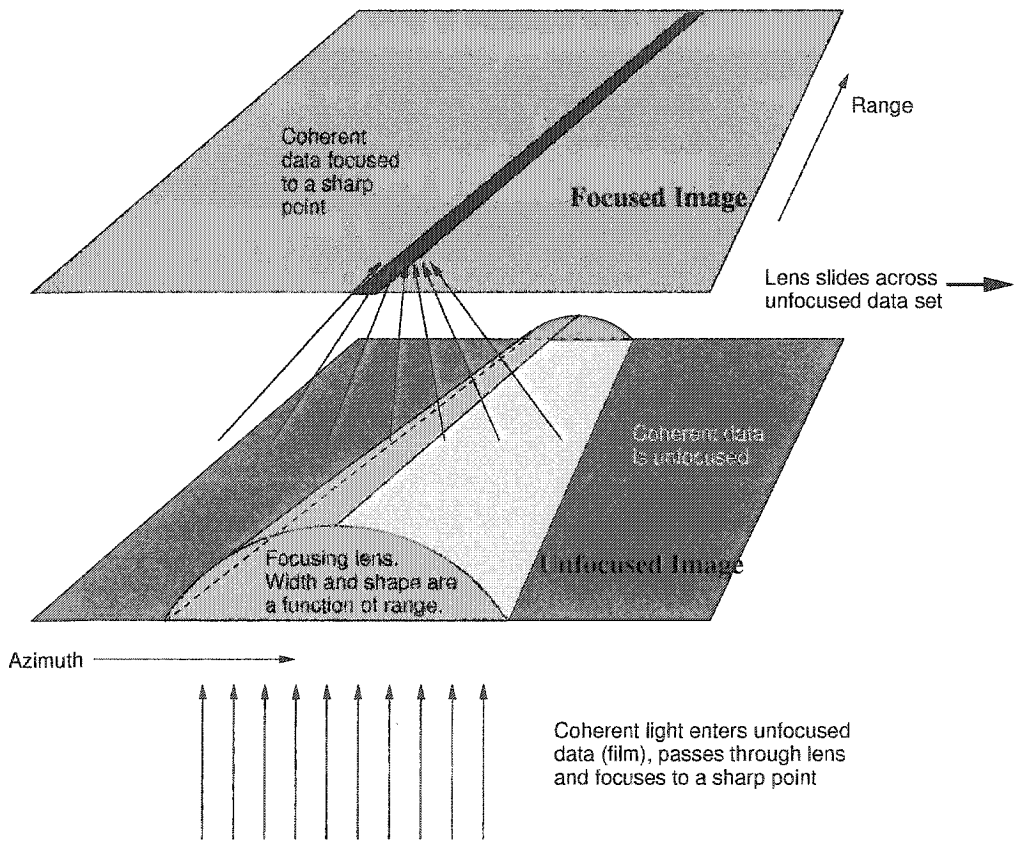

Figure 2.4. Optical SAR compression.

2.2.4 Multi-channel SAR

Just as humans have two eyes to allow for depth perception, multiple channel SAR systems allow for the extraction of information contained in dimensions that would otherwise be projected onto a 2-dimensional image. Using this approach, a two-channel SAR, for example, can take a snapshot of the scene at time t with an antenna, then take another snapshot from exactly the same point

in space at time $t + \Delta t$ with a second antenna [LSG+02]. The two antennas are generally aligned along the direction of motion vector (for the satellite or aircraft), so that each observes the scene from the same spatial position but at different times. The displacement time, Δt, is given by the speed of the platform and the physical separation, or baseline, between the antennas. Instead of configuring a system in the along-track mode as just described, a SAR system can also be configured in an across-track mode. The along-track mode allows for change detection in the time dimension while the across-track mode allows for change detection in one of the spatial dimensions. The change detection in the spatial dimension, mostly in the vertical dimension, is used to create digital elevation models [BH98].

While a multi-channel SAR is desirable for GMTI, it is still possible to detect moving targets with only a single SAR antenna. Additionally, special processing of the individual channels can enhance GMTI capability [LSG+02].

2.2.4.1 ATI

The following outlines the ATI prescription for moving target detection and measurement. Write the complex slow time samples from the leading antenna and trailing antenna as $z_1(m)$ and $z_2(m)$, respectively. Interpolate the samples from the trailing antenna so that one estimates what it would have measured from the the position of the leading antenna at time m. One thus estimates $z_2(m + \Delta t)$. The remainder of this thesis assumes that $z_2(m + \Delta t)$ has been estimated, and we simply write $z_2(m)$ to represent $z_2(m + \Delta t)$. The averaged interferometric phase is then computed as

$$\delta = \arg\left(\sum_{m=0}^{n-1} z_1^*(m) z_2(m)\right). \tag{2.7}$$

Stationary clutter should return a zero phase, while moving targets, due to a decrease or increase in range, will manifest a non zero phase. The actual measurement reflects the targets' across-track velocity component.

2.2.4.2 DPCA

The DPCA prescription computes the difference between measurements using

$$m_{DPCA} = \sum_{m=0}^{n-1} |z_1(m) - z_2(m)|^2. \tag{2.8}$$

With DPCA, one expects that two time displaced measurements of a target that does not change will yield two identical results. Thus, after subtraction, the metric should return zero. However, if

the target does change between measurements, for example in phase, then the subtraction will give a non zero result.

2.2.5 Exo-clutter SAR-GMTI techniques

Recall that a SAR generates high resolution images in the slow-time dimension by exploiting the Doppler history of illuminated targets. The span of Doppler frequencies observed by the system is determined by the radar platform speed and the imaging geometry. Typically, a SAR system oversamples the terrain reflectivity signal. In these cases, clutter, or the stationary radar data, does not occupy the available spectrum. Due to the difference in relative velocities between moving targets and the radar, versus stationary targets and the radar, it is possible to identify the clutter band and observe targets that fall outside of it. This technique can only detect targets that are separated from the clutter in the frequency band and is thus called an exo-clutter technique. It is also referred to as an incoherent detection technique [LSG+02].

$$B_{Doppler} \propto \frac{\gamma v_a}{\lambda}, \tag{2.9}$$

where γ denotes the 3dB width, the width between points 3dB down from the peak value, of the SAR azimuthal antenna pattern, v_a denotes the SAR platform velocity and λ represents the radar signal wavelength.

Sufficiently fast moving targets have Doppler frequencies outside the clutter spectrum so they can be detected with an analysis of the frequency response of the SAR data. Rough estimates of the target velocity parameters can also be estimated from the frequency analysis [LSG+02].

2.3 Statistics of multi-channel SAR

The second-order statistics of a multi-channel SAR system are adequate to define CFAR detection rules for moving targets. The statistics of the covariance matrix of a k-channel system, denoted by $\boldsymbol{R}$ in this thesis, incorporate the information necessary to construct these detection rules. Although the 2×2 covariance matrix will dominate the cases considered in this thesis, k-channel systems have already been realized, so we shall consider the statistical properties of the $k \times k$ covariance matrix. However, when considering the 2×2 case, we assume the following form for the covariance matrix

$$\boldsymbol{R} = \begin{bmatrix} \sigma_1^2 & \sigma_1\sigma_2\rho e^{j\Phi} \\ \sigma_1\sigma_2\rho e^{-j\Phi} & \sigma_2^2 \end{bmatrix}, \tag{2.10}$$

where σ_1^2 and σ_2^2 represent the power of the radar reflections measured by each antenna, Φ denotes the expected phase difference between measurements of the terrain, and ρ denotes the correlation between the two measurements. For stationary terrain, when the antennas make their measurements from the same spatial location, there should be no phase difference between measurements and $\Phi \equiv 0$.

Interest in statistical properties of the covariance matrix seems to have reached critical mass in the late 1920's. Scottish mathematician, John Wishart [Wis28], is credited with the definitive exposition. In fact, it was in 1928 that he derived the probability distribution of the covariance matrix which today is named the "Wishart distribution". His work was motivated by the characterization of multivariate population variances, but it has come to light that his work provides that basis for innumerable applications. The result derived for the case of real covariance matrices is given below.

Real Wishart Distribution: Given n identically distributed, real, zero-mean Gaussian random vectors, $\{\vec{x}_0, \ldots, \vec{x}_{n-1}\}$, each with k elements and pairwise with covariance matrix $\mathcal{E}\{\vec{x}_i \vec{x}_i^\dagger\} = \boldsymbol{R}$, the pdf of the sample covariance matrix,

$$\hat{\boldsymbol{R}} = \sum_{m=0}^{n-1} \vec{x}_m \vec{x}_m^\dagger, \tag{2.11}$$

is the real Wishart pdf, *i.e.*:

$$p(\hat{\boldsymbol{R}}) = \frac{\det \hat{\boldsymbol{R}}^{(n-k+1)/2} e^{-\mathrm{Tr}(-\frac{1}{2}\boldsymbol{R}^{-1}\hat{\boldsymbol{R}})}}{I_n(\boldsymbol{R})}, \tag{2.12}$$

with the normalization constant $I_n(\boldsymbol{R}) = 2^{k^2/2} \det \boldsymbol{R}^n / 2\Gamma(n/2)\Gamma((n-1)/2) \ldots \Gamma((n-k+1)/2)$. In the above $\mathrm{Tr}(\cdot)$ denotes the trace operator.

The sample space of the Wishart distribution is all positive definite $k \times k$ symmetric matrices. The quantity n is often referred to as the number of "looks". It is, intuitively, the number of independent samples used to estimate the covariance matrix.

Goodman [Goo63] extended the Wishart distribution to complex data in 1963. The conditions for the complex Wishart distribution are the same as for the real Wishart distribution, but the vector elements are zero-mean complex circular Gaussian random variables. In the case of the complex Wishart distribution, the sample space is the set of all positive definite $k \times k$ Hermitian matrices.

Complex Wishart Distribution: The pdf of the Hermitian sample covariance matrix,

$$\hat{\boldsymbol{R}} = \sum_{m=0}^{n-1} \vec{z}_m \vec{z}_m^\dagger = \begin{bmatrix} \hat{\sigma}_1^2 & \sigma_1 \sigma_2 \eta e^{j\delta} \\ \sigma_1 \sigma_2 \eta e^{-j\delta} & \hat{\sigma}_2^2 \end{bmatrix}, \tag{2.13}$$

estimated from n identically distributed k-element, complex zero-mean circular Gaussian random vectors, $\{\vec{z}_0, \ldots, \vec{z}_{n-1}\}$, each with complex covariance matrix, $\mathcal{E}\{\vec{z}_i \vec{z}_i^{\dagger}\} = \boldsymbol{R}$ is

$$p(\hat{\boldsymbol{R}}) = \frac{\det \hat{\boldsymbol{R}}^{n-k} e^{-\mathrm{Tr}(\boldsymbol{R}^{-1}\hat{\boldsymbol{R}})}}{I_n(\boldsymbol{R})}, \tag{2.14}$$

with normalization constant $I_n(\boldsymbol{R}) = \pi^{\frac{1}{2}k(k-1)}\Gamma(n)\Gamma(n-1)\ldots\Gamma(n-k+1)\det \boldsymbol{R}^n$. Goodman's method for deriving (2.14) [Goo63] is quite interesting. By using the joint pdf of the elements x_i, Goodman expressed the characteristic function of the complex Wishart pdf as

$$\Phi(\boldsymbol{\Omega}) = \det \boldsymbol{R}^{-n} \det[\boldsymbol{R}^{-1} - j\boldsymbol{\Omega}^{-n}]. \tag{2.15}$$

Direct inversion of (2.15) appears daunting, (although it was subsequently elegantly solved iteratively, see [JN02]), but Goodman realized that the Fourier transform of the integral

$$I_k = \int_R \det \hat{\boldsymbol{R}}^k e^{-\mathrm{Tr}(\boldsymbol{R}^{-1}\hat{\boldsymbol{R}})} = \pi^{\frac{1}{2}k(k-1)}\Gamma(n+k)\Gamma(n+k-1)\ldots\Gamma(n+1)\det \boldsymbol{R}^{k+n} \tag{2.16}$$

provided the correct characteristic function.

The Wishart distribution has often been interpreted as the generalization of the χ^2-distribution as readily seen by considering the 1×1 case. Also, from the characteristic function in (2.15), it is revealed that the sum of two Wishart random matrices with equal covariance matrices is again Wishart distributed, but with a sum of the number of looks. The important question of the form of the distribution for the sum of two Wishart distributions with different covariance matrices has been presented in the form of zonal polynomials [Jam64].

Random matrices are prevalent in the study of statistical physics. Motivated by the need to describe the distribution of eigenvalues of Hamiltonian matrices, Mehta [Meh67] in 1967, developed a very interesting theory of random matrices. His methods are general, and can be used to evaluate integrals such as (2.16) which Goodman evaluated using a Cholesky decomposition. Mehta's methods may be of use in determining the form of the sum of two Wishart distributions.

Credit for application of the Wishart distribution in SAR goes to Lee [LMH94]. In 1994, he realized that the off-diagonal elements of the complex Wishart random variable were in fact the interferogram and was able to write down the marginal pdf's in the 2×2 case for the interferometric amplitude and phase. His 1994 paper [LMH94] was concerned with polarimetric classification,

but was quickly adapted to across-track interferometry, and more recently, in 2000, to along-track interferometry [Gie01a]. Lee's result for the interferometric phase is given by

$$f_{\Delta}(\delta) = \frac{\Gamma(n+1/2)(1-\rho^2)^n\beta}{2\sqrt{\pi}\Gamma(n)(1-\beta^2)^{(n+1/2)}} + \frac{(1-\rho^2)^n}{2\pi}{}_2F_1(n,1;1/2;\beta^2), \tag{2.17}$$

for $\pi < \delta \leq \pi$, where $\beta = |\rho|\cos(\delta - \Phi)$, and where ${}_2F_1(a,b;c;z)$ is the Gauss hypergeometric function. In addition to the phase distribution, the magnitude distribution was also derived as

$$f_{\eta}(\eta) = \frac{4n^{n+1}\eta^n}{\Gamma(n)(1-\rho^2)} I_0\left(\frac{2n\eta\rho}{1-\rho^2}\right) K_{n-1}\left(\frac{2n\eta}{1-\rho^2}\right), \tag{2.18}$$

where I_0 and K_{n-1} are modified Bessel functions of the first and second kind, respectively, and of order zero and $n-1$, also respectively, [GR00]. In [Gie01a], Gierull demonstrated that the interferometric magnitude can assist with moving target detection. In fact, Gierull used both the marginal phase and marginal magnitude probability density functions to estimate constant false alarm rate thresholds. Although mathematically challenging, it may be possible to refine his results since the probability of a type I error can be reduced, while maintaining a low false alarm rate, by using the joint pdf of the phase and the magnitude rather than the marginal distributions.

Another extension of the Wishart distribution has been to consider non-central random vectors rather than zero mean random vectors. The common interpretation is to think of a matrix parallel to the non-central χ^2-distribution. In 1944, Anderson and Girshick presented the characteristic function of the non-central Wishart distribution for the real-valued rather than complex random vector case [AG44]. The corresponding pdfs are written in terms of a central Wishart distribution "damped" by a hypergeometric function with a matrix argument. It has been stated that the literature on the complex non-central Wishart distribution is sparse [Gie02], but Gierull has recently applied the rank-1 non-centrality case (the non-zero elements of $\mathcal{E}\{\vec{z}_i\}$ are identical) in describing the statistics of a deterministic moving target in random clutter.

2.4 Implementation of automatic detection algorithms

The detection of moving targets hinges upon the ability to distinguish these targets from clutter. As discussed in section 2.2.5, one way of achieving clutter cancellation is to ensure that the clutter only occupies a well defined fraction of the available bandwidth of the system leaving moving targets in the remaining regions. An automatic implementation of this algorithm involves identifying and

suppressing the clutter bandwidth region. The residue data are then SAR processed and thresholded in power [LSG+02].

With a multi aperture system, clutter cancellation can be achieved by making use of the correlation properties between the images. In the SAR Space Time Adaptive Processing method (SAR-STAP), the k-channel clutter covariance matrix is adaptively estimated, inverted, and applied to the clutter [Bar92]. For instance, if the channel samples are arranged as a vector (at slow time index m),

$$\vec{z}(m) = \begin{bmatrix} z_1(m) \\ z_2(m) \\ \vdots \\ z_k(m) \end{bmatrix} \tag{2.19}$$

with complex covariance matrix, $\boldsymbol{R} = \mathcal{E}\{\vec{z}(m)\vec{z}(m)^\dagger\}\ \forall m$, then the cross-correlations are removed by applying the "whitening" matrix, $\boldsymbol{W} = \boldsymbol{R}^{-1/2}$. If a moving target signal vector is added to the clutter signal vector, and the target signal vector has a different covariance matrix from the clutter, then $\boldsymbol{W}$ does not completely remove the target signal cross-correlations allowing for detection of the moving targets. One way to detect the targets is to apply a linear filter and detector (see figure 4.1). Mathematically, this operation can be expressed as

$$y(m) = |\vec{e}^\dagger \boldsymbol{W} \vec{z}(m)|^2, \tag{2.20}$$

where the $k-$element vector, $\vec{e}$, serves to provide a weighted sum of the decorrelated elements. It should be chosen to maximize the signal to clutter ratio. Residual moving target correlations can also be emphasised by increasing the number of apertures (so that the overall clutter variance tends to zero). Alternatively, or additionally, one could average neighbouring samples in the data space with the effect of reducing detected clutter variance at the expense of resolution. The decimated image is given by

$$y(l) = \frac{1}{n} \sum_{m=ln}^{n(l+1)-1} |\vec{e}^\dagger \boldsymbol{W} \vec{z}(m)|^2, \tag{2.21}$$

where the data have been decimated by the factor n.

Implementation of an automatic algorithm involves estimating $\boldsymbol{W}$ and applying a threshold to $y(m)$ or $y(l)$ given the statistics of the random vectors $\vec{z}(m)$. The majority of the literature considers $\vec{z}(m)$ to be a locally stationary complex, zero-mean Gaussian vector allowing the complex Wishart distribution of the covariance matrix estimates to be applied [TBQ95, LMH94, Gie01a]. In the 2-channel case, when the data from each are balanced in power, this technique leads to the DPCA

approach for GMTI. The prescription for DPCA is to subtract the two data channels and apply some norm, such as the magnitude, that maps the complex difference onto the real line. Data that are stationary should be the same for both channels and should cancel out. It can be shown that in homogenous terrain, DPCA is the optimal filter for GMTI [GL03].

In another approach, specific to a 2-channel system, the phase of the off-diagonals of the covariance matrix estimates is used as a detector. The off-diagonal elements are the product of one channel and the complex conjugate of the other. The resulting quantity is referred to as the interferogram [LSG+02]. The rationale for this approach considers the physical differences between the two time-delayed snapshots of the target under observation. If a target moves through range in between the snapshots from the two apertures, then the corresponding difference in range will manifest as a proportional difference in phase. This phase measurement divided by the displacement time can provide an estimate of the target radial velocity. However, considering detection, since most of the terrain has not changed, the phase difference between measurements should be zero. Thus by thresholding the phase difference (the argument of the covariance matrix estimate off-diagonal), another automatic detector can be implemented. It should be emphasised that the data are not linearly filtered as in the previous case. Implementation of the automatic phase detector requires calculation of the phase distribution of the interferogram. This has been done, for example, by using the complex Wishart distribution [LMH94].

2.5 Joint Interferometric Phase and Magnitude detector

In the analysis of [Gie01a], it was shown that in addition to the phase, the magnitude of the interferogram can be exploited for target detection. It was shown that the joint pdf of the magnitude and phase is given as

$$f_{\eta,\Phi}(\eta,\phi) = \frac{2n^{n+1}\eta^n}{\pi\Gamma(n)(1-\rho^2)} e^{\left(\frac{2n\eta\rho\cos\phi}{1-\rho^2}\right)} K_{n-1}\left(\frac{2n\eta}{1-\rho^2}\right), \tag{2.22}$$

where η and ϕ are the normalized (to the power) magnitude and phase, where $1 \geq \rho \in \Re \geq 0$ is the correlation coefficient, and where $K_{n-1}(\cdot)$ is the modified Bessel function of order $n-1$. The colour coded joint pdf plot is shown in figure 2.5 where it is clear that η and Φ are not statistically independent. The lack of independence means that CFAR thresholds developed for the magnitude and phase that are derived from the marginal pdfs will not be optimal in the sense of maximizing the probability of detection P_d for a given false alarm probability P_f. If these thresholds are used,

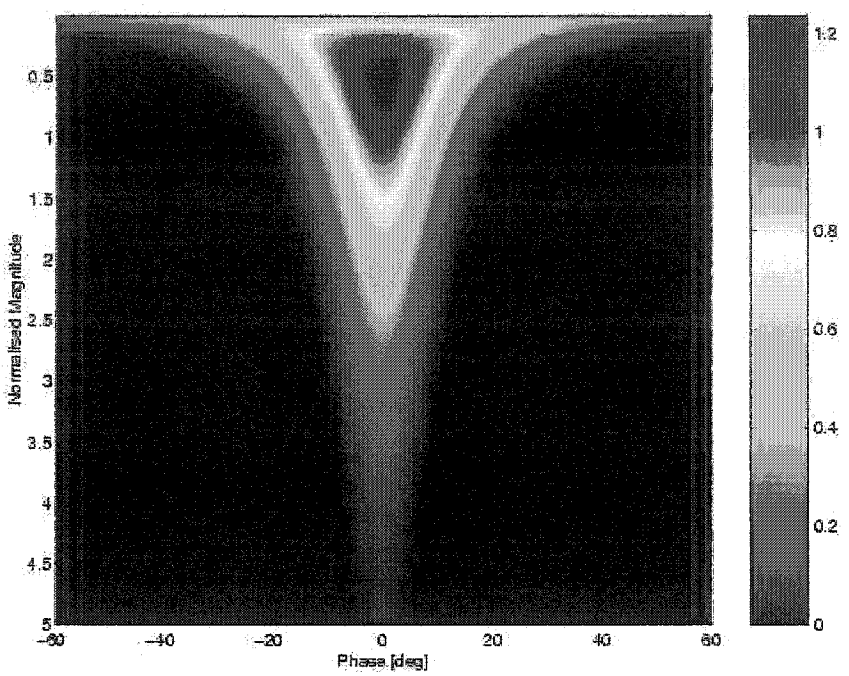

Figure 2.5. Joint pdf for the normalized ATI magnitude and the ATI phase.

as illustrated in figure 2.6, then any moving targets contained in regions 1, 2, 3, or 5 will not be detected. Only those targets in regions 4 and 6 will be detected. This "T" (regions 1,2,3,5) shaped approximation to the non-zero values of the joint probability distribution could certainly be improved. In order to increase P_d, the magnitude threshold is relaxed to smaller values. This leads, however, to a higher number of false alarms.

While it is usually true that most moving targets will have a higher Radar Cross Section (RCS) than the terrain, situating them in regions 4, 5 and 6 in figure 2.6, such will not always be the case. There are many situations where the a priori statement that, "moving targets have a relatively high RCS" is just not true. For example, over an urban area scene, metal rooftops, eaves-troughs and other man-made objects will have equally large RCSs. In addition, moving targets of low RCS are also of interest. It would not be a good idea to use a magnitude threshold for stealth-like targets as they would exhibit a measurable phase response without the magnitude response. Finally, due to the SAR focusing technique, fast moving targets will in general have low RCSs, and in some cases the magnitude response of the targets will be comparable to the clutter response. Even though passing the SAR data through filter banks designed to detect moving targets at various velocities is an option, detection via an alternate method is still justified as the filter bank method is computationally intensive.

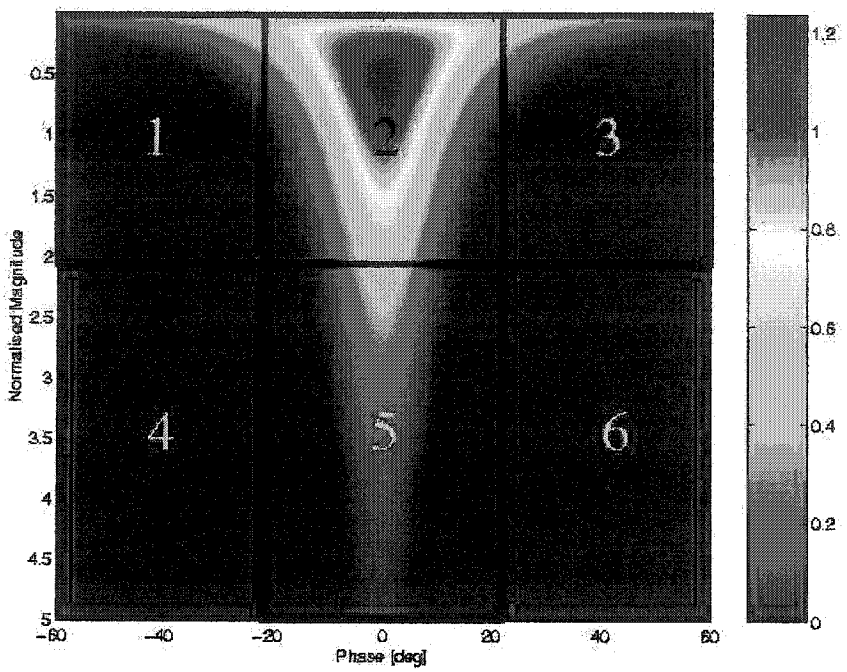

Figure 2.6. Phase CFAR thresholds, (at $\pm 20°$), filter out regions 2 and 5, while the magnitude CFAR threshold, (at 2), filters out regions 1,2 and 3.

2.6 Estimation of statistical parameters

In a multilooked SAR interferogram, the number of statistically independent samples that are averaged into each pixel is traditionally called the number of looks, n. The terminology is based upon a special SAR-image processing technique to reduce "speckle noise" [FL99, Sou99]. In this technique, the dynamic range of the random speckle is reduced by "looking" at the scene in a statistically independent way (vis à vis the noise process) and calculating the average of all the "looks."

Unfortunately, even though adjacent samples in a raw SAR dataset may be statistically independent, they become dependent once they have passed through the SAR matched filter. If, in addition, overlapping filters are used to reduce speckle at the expense of resolution, such as described in [Mor91, SCR01], additional statistical dependency is introduced. The overall effect is that the number of samples contributing to each pixel in the interferogram is more than the number of statistically independent samples that actually contribute to the pixel.

Multilook pdfs, however, are derived under the assumption of statistical independence. Indeed, analytic consideration of the correlation between samples in the derived pdfs is infeasible. When the effective, or sometimes called equivalent, number of looks is used instead of the nominal number,

the statistics of the interferogram are well represented over the whole coherence interval [JWP94]. Intuitively, the value of n should be an integer, but this is usually not the case since the mean is taken over correlated samples. It turns out, however, that all probability density functions are valid for $n \in \mathbb{R}$. Along with the number of looks, the complex coherence, $\rho e^{j\delta}$, characterizes the pdfs of both the phase and the magnitude. Taking into account that the coherence values for single pass along-track interferometry are close to one, it is safe to use the sample coherence as an estimator for ρ, citetouzi99:

$$\hat{\rho} = \frac{|\sum_{m=0}^{n-1} z_1(m) z_2^*(m)|}{\sqrt{\sum_{m=0}^{n-1} |z_1(m)|^2 \sum_{m=0}^{n-1} |z_2(m)|^2}}. \tag{2.23}$$

When the coherence value is lower, for example over water scenes, and when only a few samples are provided, a recently proposed unbiased estimator [Gie01b] can be used, thereby circumventing the bias of the sample coherence.

Given ρ, the only other parameter to estimate in the perfectly homogeneous case is n. It is proposed that n be estimated locally since the number of independent samples that are averaged into each pixel is dependent on the focusing fidelity; thus, non-stationary uncompensated error will have an effect on the effective number of looks. For instance, uncompensated range call migration will affect n.

To reduce the side-lobes, at the expense of reduced resolution, the complex interferogram is sometimes windowed before multilook averaging. The SAR processor used in this thesis [SCR01], applies overlapping Gauss weighting functions (figure 2.7) of the form

$$f(x) = \begin{cases} \exp\left(-\frac{x^2}{2(L/2.354)^2}\right) & \text{for } |x| < L, \\ 0 & \text{elsewhere,} \end{cases} \tag{2.24}$$

to the data, [SCR01]. The length of the window $L = S \cdot O$ is controlled by the two independent parameters: smoothness, S, and overlap, O. The window repeats itself after S pixels and the width is adjusted by O. Let $\Delta x = v_a / B_{Doppler}$ be the geometric SAR resolution, given as the ratio of platform velocity, v_a, to the processed Doppler bandwidth, $B_{Doppler}$, and let $\delta x = v_a / PRF$ be the pixel spacing. Then, the quotient $p = \Delta x / \delta x$ determines the number of correlated pixels in the SAR image assuming that the matched filter has been applied. Although $2L$ pixels are summed, the number of looks is therefrom roughly estimated (rule of thumb) as

$$\hat{n} = \frac{2L}{p} + 1, \tag{2.25}$$

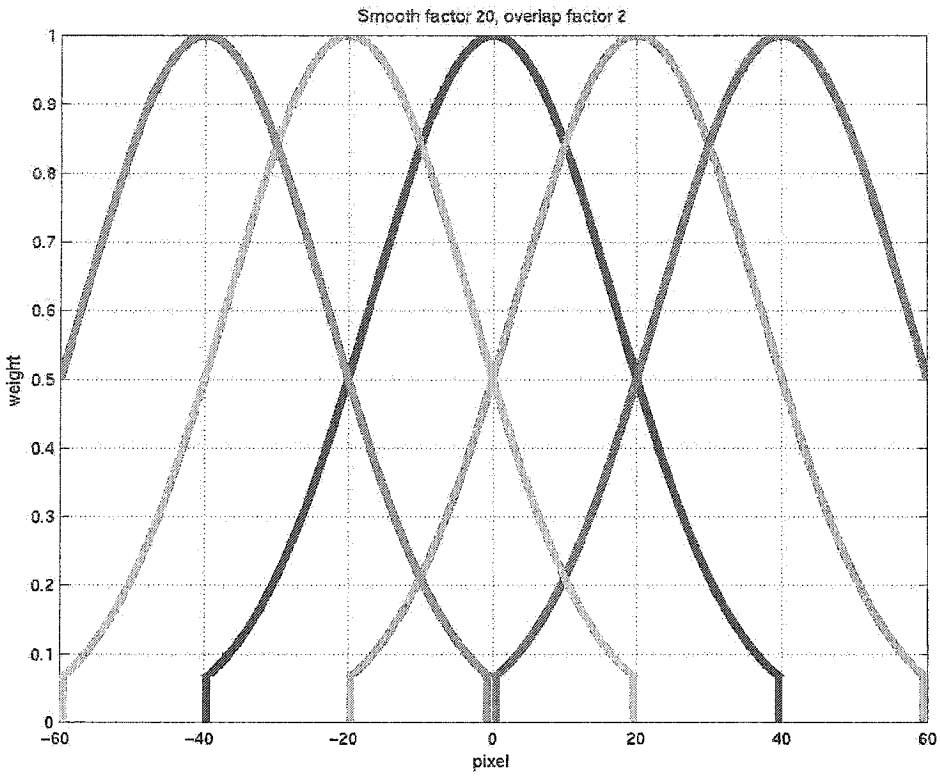

Figure 2.7. Window function of the interferometric SAR processor.

where $p = 4\text{m}/0.4\text{m} = 10$ for the Convair radar system used.

Investigations based on simulated phase data, [Gie01b] showed that the Maximum Likelihood Estimator (MLE) for n is unbiased and normal distributed. Unfortunately, one drawback of the MLE estimator for n stems from the complexity of the probability distribution function of the phase random variable (2.17).

2.7 Summary

SAR processing of moving targets is understood to cause defocus and displacement, and is subject to ambiguity in the across-track velocity component. For sufficiently high sampling frequencies coupled with a sufficiently small clutter bandwidth, moving targets can be detected in the exo-clutter region in the frequency domain.

In a multi-aperture system, correlation properties between the channels allow for the cancellation of clutter. A linear filtering of the SAR data followed by detection permits automatic GMTI, as does

a thresholding of the interferometric phase. However implementation of these algorithms requires an accurate statistical model of the multi-channel data. The most commonly used model is of a joint zero-mean complex Gaussian distribution of the channel elements, which leads to the complex Wishart distribution of the covariance matrix estimates. The complex Wishart distribution has been studied extensively, and has previously been applied to the description of multi-channel SAR data. Recently, in [Gie01a], it has been used to determine the thresholds required for automatic SAR-GMTI. Implementation of an automatic CFAR detector for SAR-GMTI requires estimation algorithms for statistical parameters, some of which are computationally expensive.

CHAPTER 3

SYNTHETIC APERTURE RADAR

In this chapter, SAR processing for GMTI is examined. Implementation of the map-drift algorithm for targets with an along-track velocity component is described, a method for ambiguity resolution is presented, and the SPECAN algorithm is adapted to the strip-map mode, particularly to enhance moving targets.

The first section describes the Convair 580 SAR system from which the majority of data in this thesis were collected. After this, the functional dependence of the target phase is presented in section 3.2 and expanded in section 3.3. Sections 3.4 and 3.5 discuss compression of moving targets using standard and automatic techniques, while section 3.6 discusses compression using the SPECAN algorithm. Finally, the inherent ambiguities of the SAR measurement system are discussed in section 3.7.

3.1 Convair 580 SAR system

SAR data presented in this thesis were collected by Environment Canada's Convair 580 aircraft configured in its along-track interferometric mode [LSG+02]. Table 3.1 lists all of the data collected for GMTI purposes over the years 1999 to 2001. Figures in this thesis may make reference to the SAR data using an "*mxlxpx*" format. The data collected are at C-band (5.3 GHz), corresponding

Table 3.1. Convair 580 SAR data summary.

July 14, 1999	November 5, 2000	November 23, 2001
m1l6p7	*m2l1p5*	*m3l1p1*
m1l6p9	*m2l1p9*	*m3l1p2*
m1l7p8	*m2l2p2*	*m3l2p9*
m1l7p10	*m2l2p6*	*m3l2p10*
	m2l3p3	*m3l2p11*
	m2l3p7	*m3l3p3*
	m2l4p4	*m3l3p4*
	m2l4p8	*m3l4p5*
		m3l4p6
		m3l5p7
		m3l5p8

to a 0.056564 m wavelength. The along-track configuration of the system consists of a main horn antenna mounted on the underbelly of the aircraft, and two sub-apertures mounted on the starboard side of the aircraft with an effective phase centre separation of 0.2704 m. The main antenna is used for transmission while the sub-apertures are used for measurement of the target echoes. These sub-apertures make measurements simultaneously, but from different spatial locations [LSG+02].

3.2 Strip-Map mode phase history function

Referring again to figure 2.3, consider now a single target that has constant acceleration on a flat-earth ground plane. As shown in [SCR01], the exponential phase of the recorded signal modelled on a target with a constant acceleration is given by

$$\exp(-j\theta(t)) = \exp\left(-j\frac{4\pi}{\lambda}r(t)\right), \tag{3.1}$$

where

$$r(t) = \sqrt{A_4t^4 + A_3t^3 + A_2t^2 + A_1t + A_0} = \sqrt{f(t)}, \tag{3.2}$$

and

$$A_4 = \frac{1}{4}\ddot{x}^2 + \frac{1}{4}\ddot{y}^2 + \frac{1}{4}\ddot{z}^2 = \frac{1}{4}\ddot{x}^2 + \frac{1}{3}\dot{r}\frac{d^3r}{dt^3} + \frac{1}{12}r\frac{d^4r}{dt^4} + \frac{1}{4}\ddot{r}^2, \tag{3.3}$$

$$A_3 = -(v_a - \dot{x})\ddot{x} + \dot{y}\ddot{y} + \dot{z}\ddot{z} = -(v_a - \dot{x})\ddot{x} + \frac{1}{3}r\frac{d^3r}{dt^3} + \dot{r}\ddot{r}, \tag{3.4}$$

$$A_2 = (v_a - \dot{x})^2 + \dot{y}^2 + y_0\ddot{y} - h\ddot{z} + \dot{z}^2 = (v_a - \dot{x})^2 + \dot{r}^2 + r\ddot{r}, \tag{3.5}$$

$$A_1 = 2y_0\dot{y} - 2h\dot{z} = 2r\dot{r}, \tag{3.6}$$

$$A_0 = y_0^2 + h^2 = r^2. \tag{3.7}$$

In the above equations, v_a denotes the speed of the radar platform, $r = r(0)$ is the range to the target at $t = 0$. The quantities $\dot{r}$, $\dot{y}$, $\dot{z}$, $\dot{x}$ are the time derivatives evaluated at $t = 0$, while $\ddot{r}$, $\ddot{y}$, $\ddot{z}$, $\ddot{x}$ are the second time derivatives evaluated at $t = 0$. Finally, the quantities d^3r/dt^3 and d^4r/dt^4 are the third and fourth derivatives of $r(t)$ evaluated at $t = 0$.

It is of interest to note that it is not possible to resolve vertical motion from ground range motion (all y and z terms and their time derivatives can be written as function of $r(t)$ and its time derivatives, $dr(t)/dt = \dot{r}$ and $d^2r(t)/dt^2 = \ddot{r}$) as the two are always defined on the surface of a cylinder. That is, the emitted radiation is cylindrically symmetric[1].

[1]Spherically symmetric radiation made cylindrically symmetric by the motion of the aircraft.

3.3 Expansion of the reference function

The signal phase function, defined by (3.1), can be expanded around $t = 0$ to get a better idea of the image formation dynamics. It is sufficient to expand

$$E(t) = \sqrt{f(t)}, \tag{3.8}$$

to get,

$$\begin{aligned} E(t) \approx\ & E(0) + \frac{1}{2E(0)} f^1(0)t + \left(-\frac{1}{4E(0)^3}[f^1(0)]^2 + \frac{1}{2E(0)} f^2(0) \right) \frac{t^2}{2!} \\ & + \left(\frac{3}{8E(0)^5}[f^1(0)]^3 - \frac{1}{4E(0)^3} 3 f^1(0) f^2(0) + \frac{1}{2E(0)} f^3(0) \right) \frac{t^3}{3!} \\ & + \left(\frac{-15}{16E(0)^7}[f^1(0)]^4 + \frac{3}{8E(0)^5} 6[f^1(0)]^2 f^2(0) - \frac{1}{4E(0)^3}[3[f^2(0)]^2 + 4 f^1(0) f^3(0)] + \frac{1}{2E(0)} f^4(0) \right) \frac{t^4}{4!} \\ & + \ldots \end{aligned} \tag{3.9}$$

It is a simple matter to calculate the derivatives of $f(t)$ since it is a 4^{th} degree polynomial. The derivative terms $f^n(0)$ can be replaced with the terms $n!A_n$ thus leading to

$$\begin{aligned} E(t) \approx\ & r + \frac{1}{2r} A_1 t + \left(-\frac{1}{4r^3} A_1^2 + \frac{1}{2r} 2A_2 \right) \frac{t^2}{2!} + \left(\frac{3}{8r^5} A_1^3 - \frac{1}{4r^3} 6 A_1 A_2 + \frac{1}{2r} 6 A_3 \right) \frac{t^3}{3!} \\ & + \left(\frac{-15}{16r^7} A_1^4 + \frac{3}{8r^5} 12 A_1^2 A_2 - \frac{1}{4r^3}[12[A_2]^2 + 24 A_1 A_3] + \frac{1}{2r} 24 A_4 \right) \frac{t^4}{4!} + \ldots \end{aligned} \tag{3.10}$$

The large quantities that appear in (3.10) are r and, through A_2 and A_3, the aircraft velocity, v_a. By omitting the small terms, the approximation becomes

$$\begin{aligned} E(t) \approx\ & r + \dot{r}t + \frac{(v_a - \dot{x})^2 t^2}{2r} + \frac{\ddot{r}t^2}{2} - \frac{(v_a - \dot{x})\ddot{x}t^3}{2r} + \frac{1}{6}\frac{d^3 r}{dt^3} t^3 - \frac{(v_a - \dot{x})^2 \dot{r} t^3}{2r^2} + \frac{\ddot{x}^2 t^4}{8r} \\ & + \frac{1}{24}\frac{d^4 r}{dt^4} t^4 - \frac{(v_a - \dot{x})^2}{4r^2} \ddot{r} t^4 - \frac{1}{8r^3}(v_a - \dot{x})^4 t^4 + \frac{1}{2r^3} \dot{r}^2 (v_a - \dot{x})^2 t^4 + \frac{1}{2r^2} \dot{r} \ddot{x} (v_a - \dot{x}) t^4. \end{aligned} \tag{3.11}$$

Once again, the large quantities are r and v_a, that is $r, v_a >> \dot{r}, \dot{x}, \ddot{r}, \ddot{x}$. Furthermore, the third and fourth derivative terms are negligible (it can be shown that the third derivative term is proportional to $1/r$ for a target travelling in a straight line with a constant acceleration). By omitting the small terms, $E(t)$ is approximated as

$$\begin{aligned} E(t) \approx\ & r + t\dot{r} + t^2 \left(\frac{\ddot{r}}{2} + \frac{(v_a - \dot{x})^2}{2r} \right) + t^3 \left(\frac{1}{6}\frac{d^3 r}{dt^3} t^3 - \frac{(v_a - \dot{x})\ddot{x}}{2r} \right), \quad \text{and} \\ \theta(t) \approx\ & a_0 + a_1 t + a_2 t^2 + a_3 t^3, \end{aligned} \tag{3.12}$$

where the $4\pi/\lambda$ has been absorbed into $a_0, \ldots, a_3$. The only term in (3.12) that is independent of a moving target's velocity characteristics is

$$a_2 = \frac{2\pi v_a^2 t^2}{\lambda r}, \tag{3.13}$$

which is exactly the parabolic approximation to the reference function of a stationary target [FL99].

All the terms in (3.12) have been grouped according to the power of t upon which they operate because it is possible to optimize the SAR filtered response of a target and determine the quantities a_1, a_2, a_3. One cannot determine a_0 because of phase wrapping. No symmetry exists between the coefficients of a polynomial[2] so it is possible to determine the radial velocity of a moving target $\dot{r}$ and the azimuthal acceleration of a moving target $\ddot{x}$. A symmetry, however, exists between the azimuthal velocity $\dot{x}$, and the radial acceleration $\ddot{r}$ as is demonstrated by the coefficient of t^2.

3.4 The SAR focusing algorithm

To second order, (3.12), states that the refelcted signal has an exponential phase given by

$$\begin{aligned} s(t) &= e^{-j4\pi/\lambda[r+\dot{r}t+(\ddot{r}/2+(v_a-\dot{x})^2/2r)t^2]} \\ &= e^{-j[(a_0+a_1t+a_2t^2]}. \end{aligned} \tag{3.14}$$

To improve the azimuthal resolution, the recorded signal, which is a sum of the contributions from many scatterers, has to be filtered by an appropriate reference function that uses the phase history to select and separate the different contributions. Based upon the phase history alone, the best reference function to use in a convolution is the complex conjugate, time reverse, of the signal function, that is [Hov80, FL99, UMF86]

$$\begin{aligned} s_{ref}(t) &= e^{j4\pi/\lambda[r_f-\dot{r}_ft+(\ddot{r}_f/2+(v_a-\dot{x}_f)^2/2r_f)t^2]} \\ &= e^{j[b_0-b_1t+b_2t^2]}, \end{aligned} \tag{3.15}$$

where, ideally, $b_1 = a_1$ and $b_2 = a_2$. The choice for b_0 does not really matter as it will only affect the phase of the compressed signal. When written as a correlation, rather than a convolution (sign of b_1), these expressions for the signal and reference functions give rise to the compressed signal

[2]Uniqueness of the Taylor, Maclaurin series expansions.

$$d(\tau) = \int_{-T}^{T} s_{ref}(t)s(t+\tau)dt \tag{3.16}$$

$$= \int_{-T}^{T} e^{j(-a_0-a_1\tau-a_2\tau^2)} e^{jt(b_1-a_1-2a_2\tau)+jt^2(b_2-a_2)}dt \tag{3.17}$$

$$= e^{j(-a_0-a_1\tau-a_2\tau^2)} \int_{-T}^{T} e^{jt(b_1-a_1-2a_2\tau)}dt \quad \text{if } b_2 = a_2 \tag{3.18}$$

$$= 2Te^{j(-a_0-a_1\tau-a_2\tau^2)}\text{sinc}[(b_1 - a_1 - 2a_2\tau)T]. \tag{3.19}$$

Expression (3.19) has sinc function magnitude which approaches a delta function as $T \to \infty$. In the realistic case of compact support, the sinc function width determines the azimuthal resolution. One of the great advantages of SAR over SLAR stems from the fact that the integration time, T, in (3.19) is proportional to the range of the target from the radar platform. The further a target from the radar, the longer it stays in the radar beam. By writing the integration time as $r\alpha/v_a$, where α is the antenna beamwidth, and by setting $b_1 = a_1$, (3.19) reveals that the determining factor in the width of the sinc function is

$$2a_2T \approx 8\pi\lambda\frac{v_a^2}{2r}\frac{r\alpha}{v_a} = \frac{4\pi v_a\alpha}{\lambda}dt. \tag{3.20}$$

One sees that the azimuth resolution does not depend on the range from the target to the radar. Thus all pixels will have equal azimuthal resolution. Furthermore, targets have a maximum response when the sinc function argument is zero, i.e.

$$\tau = \frac{b_1 - a_1}{2a_2}. \tag{3.21}$$

Since a_1 corresponds to the target radial velocity, it is clear that when a moving target is filtered with a reference function that has $b_1 = 0$, the target will compress to a location displaced from where it should really be (at $t = 0$ the target should be at $x = 0$).

It has been assumed that a_2 is known in the above analysis. In fact, for moving targets having significant azimuthal velocities or radial accelerations, a_2 is not known and an incorrect b_2 (correct for targets that are stationary) leads to a residual phase quadratic ($b_2 - a_2 \neq 0$). The compressed signal in such cases can be written as

$$d(\tau) = e^{j(-a_0-a_1\tau-a_2\tau^2)} \int_{-T}^{T} e^{jB(t+t_0)^2-jBt_0^2}dt, \tag{3.22}$$

where $B = b_2 - a_2$ and $t_0 = (b_1 - a_1 - 2a_2\tau)/(2b_2 - 2a_2)$. The squared envelope of $d(\tau)$ can be written as

$$|d(\tau)|^2 = \int_{-T}^{T}\int_{-T}^{T} e^{jB(x+t_0)^2-jB(y+t_0)^2}dxdy. \tag{3.23}$$

By changing the integration variables according to

$$u = x + y \tag{3.24}$$

$$v = x - y, \tag{3.25}$$

one can deduce, as done in appendix A, that

$$|d(\tau)|^2 = \int_0^{2T} \frac{\sin[B(2t_0 + u)(2T - u)]}{B(2t_0 + u)} du + \int_0^{2T} \frac{\sin[B(2t_0 - u)(2T - u)]}{B(2t_0 - u)} du \tag{3.26}$$

Since (3.26) is symmetric in t_0, one sees that the detected signal is symmetric around $\tau = (b_1 - a_1)/(2a_2)$ as it was before. However, the maximum of the response is not necessarily at this point.

So far it has been assumed that the recorded SAR signal has infinite extent. In reality, this is not the case as the reflected signal is modulated by the azimuth antenna pattern and is also subject to propagation losses as the range to the target increases. The symmetry in the target response, despite using an incorrect Doppler rate of change, is used in the next section to apply an autofocus technique.

3.5 Autofocus algorithm for moving targets

An important step in the automation of the GMTI process is the unsupervised target velocity estimation. For the across-track velocity component, the interferometric phase provides reliable information. For the along-track velocity, however, the interferometric phase carries little, if any, information. For this reason, most authors have not considered algorithms for estimating the along-track component of motion. In fact, historically, the GMTI problem has been addressed with non-imaging pulsed radars and estimation of the velocity vector was restricted to only one component without consideration of the other. Our presented velocity estimation technique relies upon the less sensitive measure of the "quality of focus." Among the main factors affecting the quality of focus is an accurate estimate of the Doppler rate of change in the SAR compression algorithm. Equation (3.12) shows that the second order phase coefficient which is proportional to the Doppler rate of change, depends mainly upon the along-track target component of motion. Generally, this quantity derives from the imaging geometry. Since the quality of focus measure can be examined by using only a single channel of information, with two or more channels, estimates may be averaged. The same limitations apply to estimation of target accelerations. In fact, to date, only the quality of the focus can provide any information about acceleration [Sha04]. In the following section we review

the geometry of a moving target and show how the motion characteristics translate into image characteristics by adapting the map-drift autofocus algorithm [FL99].

Among the techniques for autofocus, we adopt and adapt the map-drift algorithm found in [FL99]. With the map-drift algorithm, a stationary target with a high RCS is required as a reference. Since the Doppler rate of change depends, proportionally, on the rate of change of range between the target and the radar platform, knowledge of the radar platform velocity vector over time allows the correct Doppler rate to be estimated from the high RCS target. In our adaptation to GMTI, one starts with a model of the correct Doppler rate of change based upon the imaging geometry and the radar platform velocity vector. Estimation of the Doppler rate of a detected moving target may reveal a deviation from the model based Doppler rate, thereby allowing an estimate of the along-track motion of the target. As far as we know, adaption of the map-drift algorithm to the problem of estimating the along-track velocity of moving targets has never before been considered.

The location of a target in the compressed SAR image will be coincident with the point at which the target is broadside to the antenna. Referring to figure 3.1, this means that the location of the

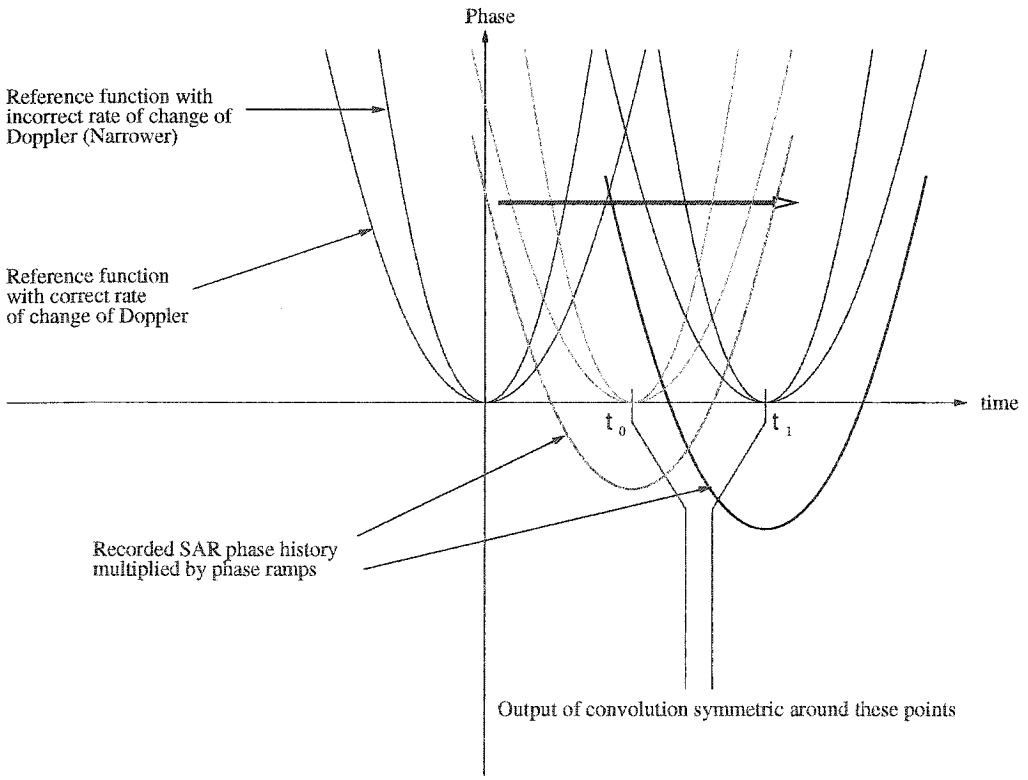

Figure 3.1. Autofocus with a phase ramp.

target will be where the recorded signal has a minimum. If the recorded signal has the form of

(3.14), the location of the minimum in phase is given by $\tau_1 = (a_1)/(2a_2)$, and the phase value at the minimum is $\Theta_1 = a_0 + a_1^2/(4a_2)$. The location of this minimum can be moved by applying a phase ramp to the data. So, for example, if the signal is multiplied by $e^{j\Delta t}$, then the minimum will occur at $\tau_2 = (a_1 - \Delta)/(2a_2)$. At this point, the parabola will have phase $\Theta_2 = a_0 + (a_1 - \Delta)^2/(4a_2)$. Now although it is not possible to measure τ_1 and τ_2, the difference can be estimated simply by calculating the drift in the response of the target. Thus, an estimate for a_2 can be obtained via

$$a_2 \cong \frac{-\Delta}{2(\tau_2 - \tau_1)}. \tag{3.27}$$

By measuring the difference in phase, one can also obtain

$$a_1 \cong \frac{\Delta^2 - 4a_2(\Theta_2 - \Theta_1)}{2\Delta}. \tag{3.28}$$

Unfortunately, due to additive noise, an unwrapped measurement of the two phases is virtually impossible with real SAR data. An alternative uses the phase difference measurement from a two-channel system to estimate the across-track velocity of the target; for instance, see [LSG+02].

The following describes the displacement technique to automatically estimate the Doppler rate to focus a moving target. The target in question is observed in the dataset *m2l1p5*. Figure 3.2 shows the fore antenna image of this moving target. The algorithm for automatic focus follows the flow

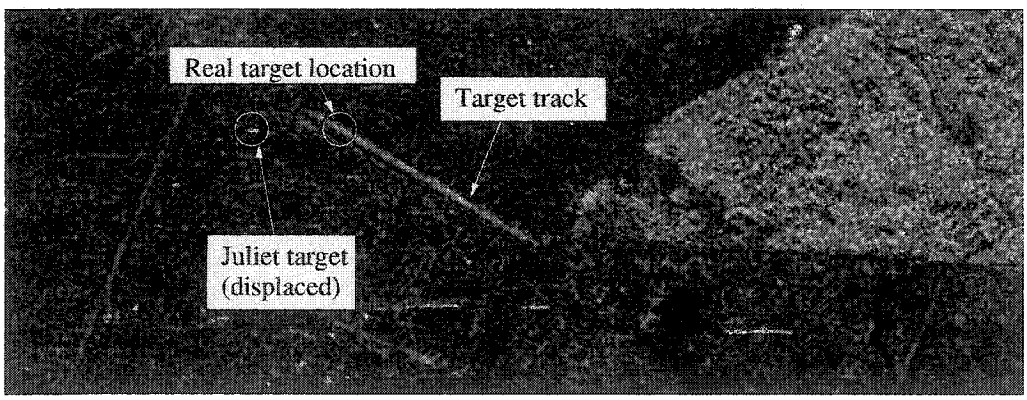

Figure 3.2. Autofocus target candidate (target named Juliet): file *m2l1p5*.

diagram depicted in figure 3.3. The first step is to SAR focus the target when a phase ramp has been applied to the data. The next step measures the displacement between the target in the first image versus the second image. This task is accomplished by measuring the integer number of pixels

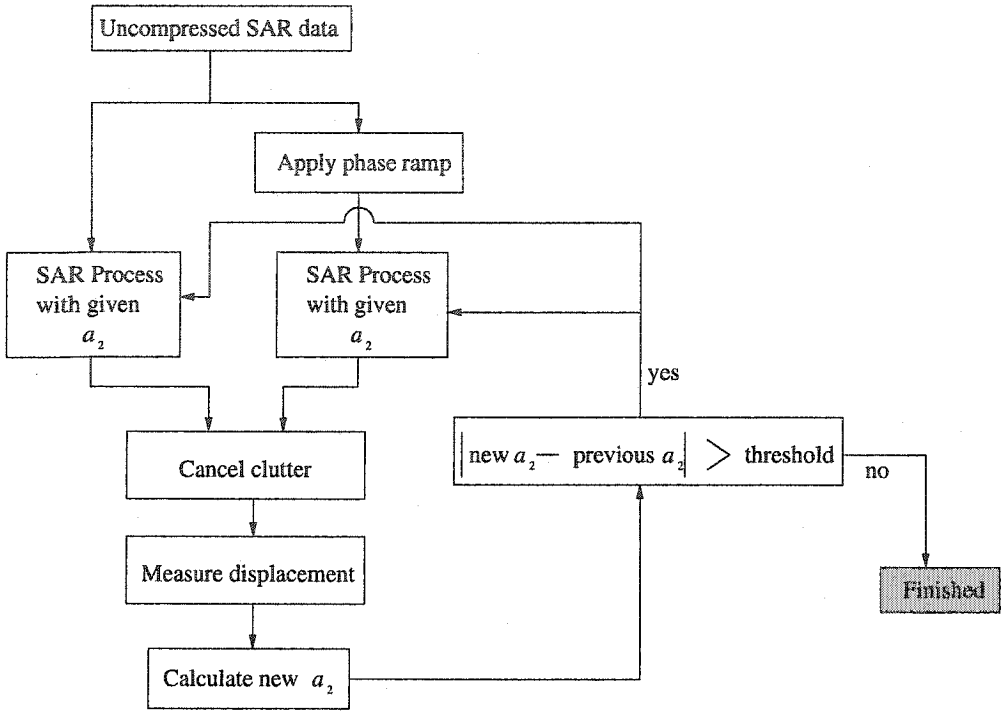

Figure 3.3. Autofocus algorithm flowchart.

by which they are offset followed by an estimate of residual sub-pixel displacement. The subpixel displacement is determined by interpolating one of the images at sub-pixel values, and maximising the cross-correlation between the two images. The cross-correlation is measured on an area local to the target so as to avoid contributions from high Radar Cross-Section (RCS) clutter targets.

The characteristics of the SAR system used for this illustration are outlined in table 3.2. After

Table 3.2. SAR system parameters for autofocus: file *m2l1p5*.

SAR System	Convair 580
Platform speed	121.038 m/s
Range to target	9838.19 m
Sample spacing	0.19455 m
Phase ramp applied	3 m/s
Measured displacement	1328.109 pixels

the first iteration, it is found that $\hat{a}_2 = 0.702655$ whereas the value used was $a_2 = v^2/(2r) = 0.74456$. The difference is accounted for by solving for $\dot{x}$ in

$$\frac{(v - \dot{x})^2}{2r} = 0.702655. \tag{3.29}$$

The solution gives $\dot{x} = 3.455$ m/s. Repeated back-substitution of the estimate shows rapid convergence to $\dot{x} = 6.0893$ m/s. Figure 3.4 illustrates the algorithm convergence.

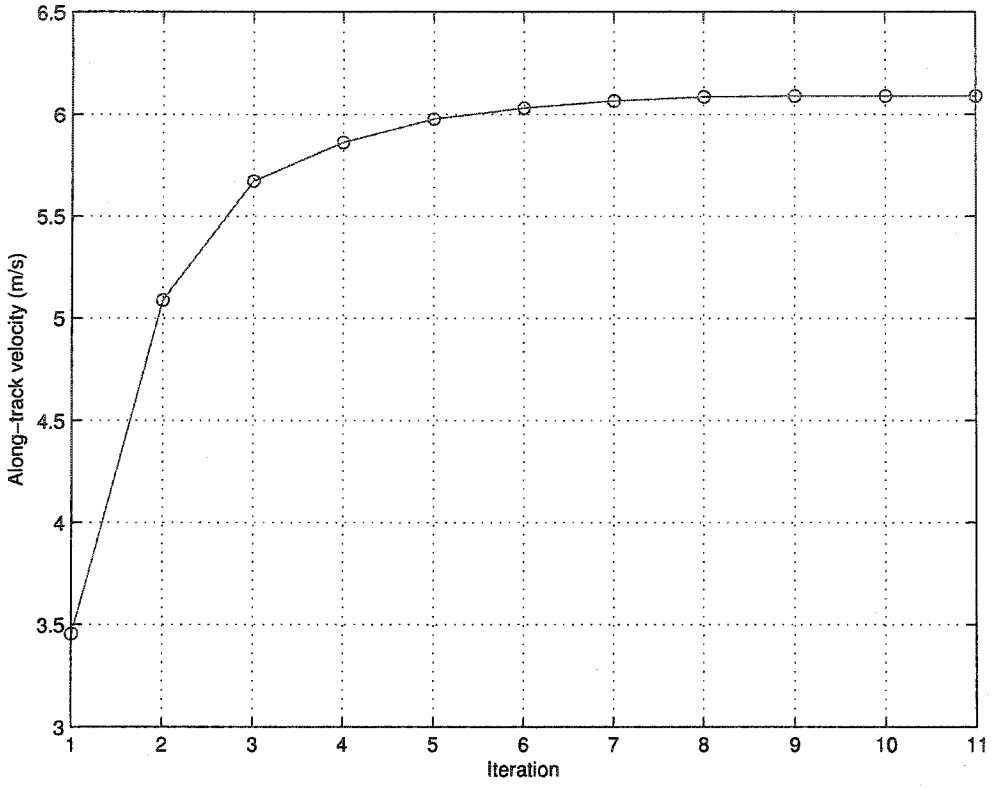

Figure 3.4. Convergence of autofocus algorithm.

3.6 SPECAN SAR processing

Full azimuth compression can be achieved by generating an appropriate reference function and performing the convolution with the recorded SAR signal. Another way to azimuth compress the signal is to apply the so-called *deramp* or SPECAN algorithm. This algorithm is "quick", in that it is fast, and "dirty" in that it does not produce the same quality of result as full compression.

Equation (3.14) describes how the phase of the SAR signal evolves through time for a particular target located at $t = 0$. Figure 3.5 shows, in fact, that the recorded SAR signal also depends on the antenna pattern and the terrain reflectivity. One can write the expression for the reflected signal from a target that is measured at broadside time $t_0 \neq 0$ as

$$s(t) = g(t_0)a(t - t_0)e^{-j[a_0 + a_1(t-t_0) + a_2(t-t_0)^2]}, \tag{3.30}$$

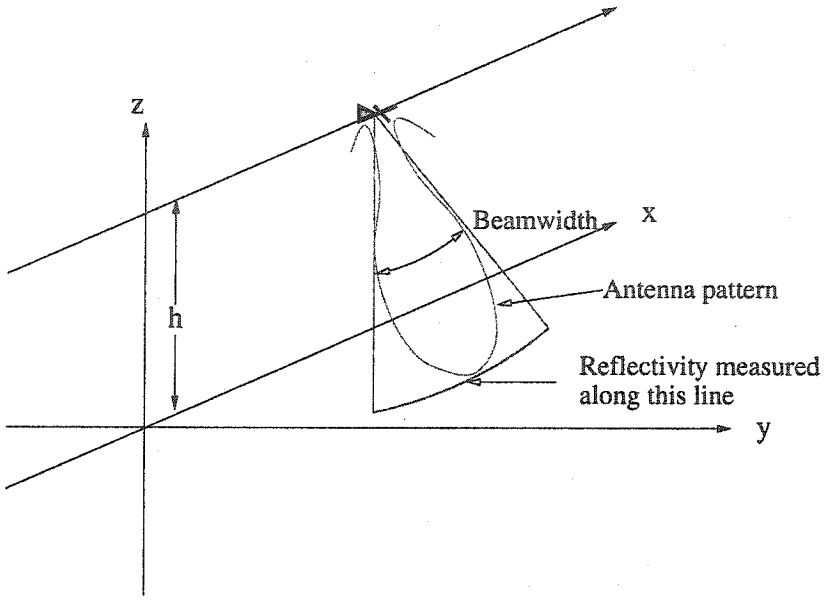

Figure 3.5. Radar sampling of target.

where $a(t)$ represents the antenna pattern (which is symmetric and has support $2T$), and $g(t)$ represents the target reflectivity. Although the actual antenna pattern is a function of angle, the equivalent function of time is defined as the antenna gain that a target experiences as the aircraft passes by. This function will depend on the speed of the aircraft, and on the range between the target and the radar. It is assumed that during observation the intersection of the beam with the earth (as seen in in figure 3.5) aligns along the $x-$axis, and that curvature is negligible. It should be made clear that the data are range compressed. Multiply both sides of (3.30) by $\exp(ja_2t^2)$ and expand the exponential argument to get

$$s(t)e^{ja_2t^2} = q(t) = g(t_0)a(t-t_0)e^{-j(a_0-a_1t_0+a_2t_0^2)}e^{-j(a_1-2a_2t_0)t} \tag{3.31}$$

Now take the Fourier transform of both sides to see

$$\begin{aligned} Q(\omega) = \mathcal{F}\{q(t)\} &= g(t_0)e^{-j(a_0-a_1t_0+a_2t_0^2)}\mathcal{F}\{a(t-t_0)e^{-j(a_1-2a_2t_0)t}\} \\ &= g(t_0)e^{-j(a_0-a_1t_0+a_2t_0^2)}\int_{-\infty}^{\infty} a(t-t_0)e^{-j(a_1-2a_2t_0)t}e^{-j\omega t}\mathrm{d}t \\ &= g(t_0)e^{-j(a_0-a_2t_0^2+\omega t_0)}\int_{-\infty}^{\infty} a(t)e^{-j(a_1-2a_2t_0+\omega)t}\mathrm{d}t \\ &= g(t_0)e^{-j(a_0-a_2t_0^2+\omega t_0)}A(a_1-2a_2t_0+\omega) \end{aligned}, \tag{3.32}$$

where $A(\omega)$ denotes the Fourier transform of the antenna pattern. One notes that for a large time extent antenna pattern, say $2T$, $A(\omega)$ will have a width approximately equal to $1/2T$. For an antenna pattern modelled as a rectangular window, the response will be a sinc function evaluated at $a_1 - 2a_2t_0 + \omega$. This function will experience a peak value at $\omega = 2a_2t_0 - a_1$. Recall that for stationary terrain, $a_1 = 0$, thus, to a good approximation, $Q(\omega)$ well represents the compressed SAR scene, although the image map is scaled by $2a_2$.

Since

$$2a_2 = \frac{2\pi v_a^2}{\lambda r}, \tag{3.33}$$

the scaling, or squashing factor depends on the range. For larger range, the sample spacing of the compressed image becomes spatially narrower. However, for increasing range, $2T$ increases, therefore, $A(\omega)$ becomes narrower. On the whole, the one effect balances the other, revealing the independence of the compressed resolution on range. As shown in figure 3.7, for a relatively small scene, the change in scale is not really apparent.

Although the analysis assumes a single target, we have strictly used linear operations; therefore, the principle of superposition applies yielding compression for all targets in the scene. In practice, one would multiply each line of constant range with the appropriate phase quadratic defined using a_2.

The effect of finite limits on the Fourier integral, as experienced in reality, is seen on the edges of the compressed image. Due to compact support on the antenna pattern, the only targets affected by the finite limits are those incompletely swept by the antenna pattern. These incomplete data manifest as targets with smaller compression gain that eventually diminish to zero for targets that are only measured by the edge of the antenna pattern.

If a target has an across-track velocity, then $a_1 \neq 0$, and the target will not appear where corresponding stationary data appear; however, it will experience the same compression gain as the stationary terrain. By situating the moving target in regions where the stationary data have less gain, one increases the target to clutter ratio. One achieves this effect by windowing the recorded data with a window of length slightly larger than the antenna beamwidth, thereby selecting a full synthetic aperture only for a narrow range targets in the middle of the window. Targets further away from the middle will experience less compression gain allowing superimposed moving targets, displaced from the central regions, to show more clearly. For this thesis, a rectangular window has been selected. Future work might seek to define this window more advantageously for GMTI.

An illustration of SPECAN processing with a moving target is illustrated in figure 3.7. For comparative purposes, the raw data image is also shown in figure 3.6. As seen in figure 3.7 the moving target has a good signal to clutter ratio.

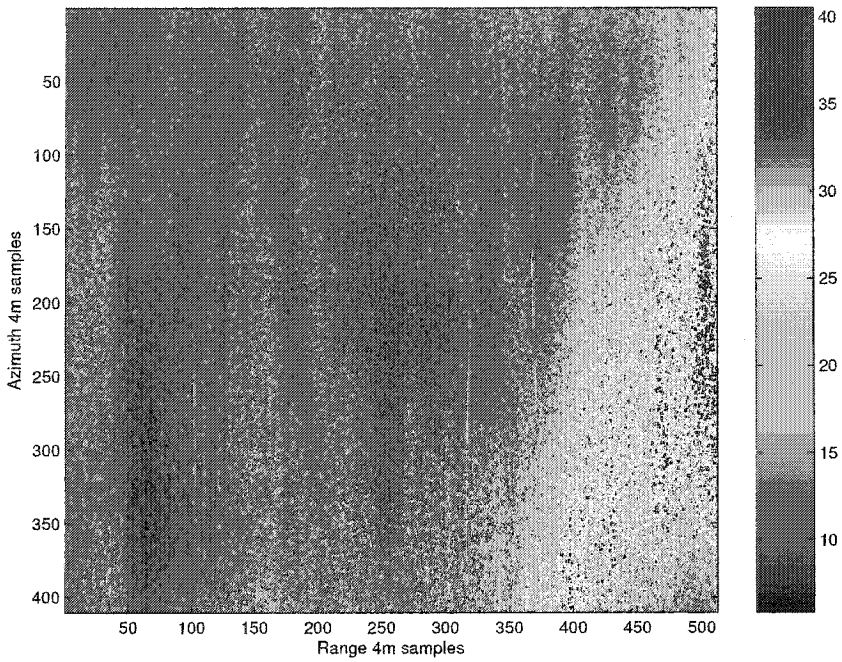

Figure 3.6. Raw data before processing: file *m2l1p5*.

3.7 Dual ambiguities

Trials confirm the evidence of SAR processing ambiguities that stem from the sampled nature of both the SAR signal and the matched filter used for compression [Liv03]. Oddly, interferometric pairs show a phase jump at the junction between ambiguities. By proceeding with an analysis of the phases of the compressed signals, it becomes clear that the phase jumps are due to the time resampling of one of the channels. The reason for actually doing the time resampling stems from the fact that the physical GMTI system consists of two antenna apertures aligned along-track that are designed to sample the returned signal at the same instant in time. In effect, the fore antenna measures what the aft antenna does at a later time. The difference in time is determined by how long it takes the aircraft to move the aft antenna into the previous position of the fore antenna. This time depends on the physical separation between the antenna phase centres and the speed of the aircraft. From a SAR processing point of view, this geometry is easy to accommodate; one simply processes the aft channel to return the response of the measurement at a delayed time.

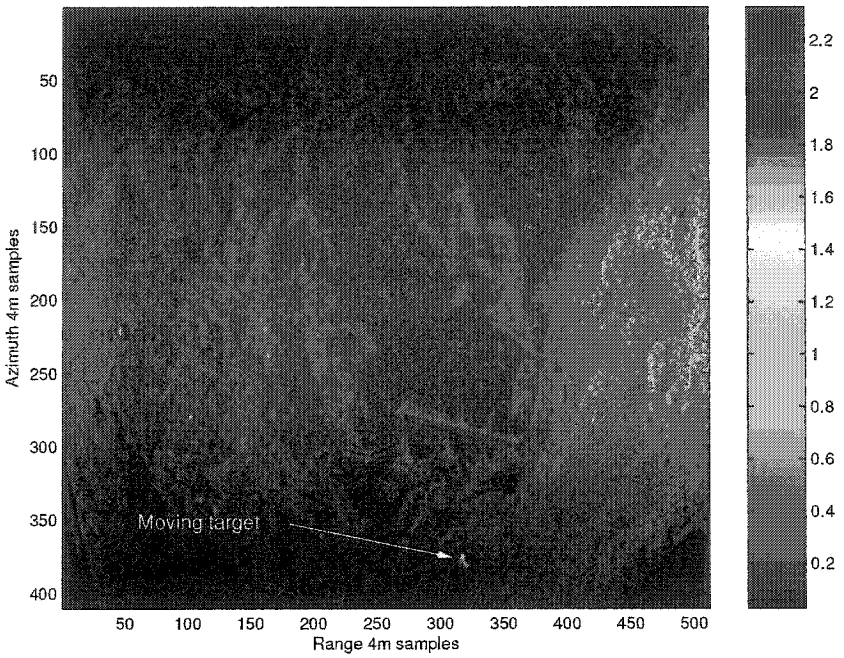

Figure 3.7. "Quick" and "dirty" image: file *m2l1p5*.

3.7.1 Reference function

As shown previously [SCR01, LSG+02], the expression for the reference function for a target with only an across-track velocity can be written as

$$s_{ref}(t) = \exp\left[j\beta(\sqrt{(v_a t)^2 + (r_0 + \dot{r}_f t)^2} - r_0)\right], \tag{3.34}$$

where v_a is the aircraft velocity, r_0 is the target broadside range, $\beta = 4\pi/\lambda$, λ is the radar wavelength, and $\dot{r}_f$ is the target candidate radial velocity. This equation can be understood by considering the target positioned at $r_0 + \dot{r}_f t$ in the slant range dimension, the aircraft positioned at $v_a t$ in the perpendicular along-track direction, and then applying Pythagoras' theorem. In this model, the aircraft sits at along track position, 0, when $t = 0$. Now, in order to know the response of SAR processing at a position displaced from $t = 0$, one only needs to introduce a time delay into the reference function. Spatially, we desire an offset of the phase centre separation, d, but this corresponds to a time delay of d/v_a where v_a is the aircraft speed. Since one also desires to place the target into the same time reference, the overall, new, reference function is

$$s_{ref}(t) = \exp\left[j\beta(\sqrt{(v_a(t + d/v_a))^2 + (r_0 + \dot{r}_f(t + d/v_a))^2} - r_0)\right]. \tag{3.35}$$

Expansion of the square root function using $\sqrt{1+x} \approx 1 + 1/2x + \mathrm{O}(x^2)$ for $x \ll 1$ yields

$$s_{ref}(t) \approx \exp\left[j\beta\left(\frac{v_a^2 t^2}{2r_0} + t\left(\frac{v_a d}{r_0} + \dot{r}_f + \frac{\dot{r}_f^2 d}{v_a r_0}\right) + \frac{\dot{r}_f d}{v_a} + \frac{\dot{r}_f^2 d^2}{2r_0 v_a^2}\right)\right], \tag{3.36}$$

where a couple of very small terms have been discarded.

Recall that in reality, only a sampled version of the signal is recorded, and in the computer, a sampled version of the reference function is used for compression. Let the sampling frequency be denoted by f_p so that $t = m/f_p$. Also recall that the recorded signal also has, effectively, compact support (so does the reference function). Therefore, to ensure this condition, multiply (3.36) by a rectangular ($\mathrm{rect}_L(x)$) function:

$$s_{ref}(m) = \mathrm{rect}_L(m) \exp\left[j\beta\left(\frac{v_a^2 m^2}{2r_0 f_p^2} + \frac{m}{f_p}\left(\frac{v_a d}{r_0} + \dot{r}_f + \frac{\dot{r}_f^2 d}{v_a r_0}\right) + \frac{\dot{r}_f d}{v_a} + \frac{\dot{r}_f^2 d^2}{2r_0 v_a^2}\right)\right], \tag{3.37}$$

where,

$$\mathrm{rect}_L(m) = \begin{cases} 1/L & \text{if } |m| \le L \\ 0 & \text{otherwise} \end{cases} \tag{3.38}$$

Equation (3.37) is modelled on the actual recorded signal,

$$s(m) = \mathrm{rect}_L(m) \exp\left[-j\beta\left(r_0 + \frac{v_a^2 m^2}{2r_0 f_p^2} + \frac{m}{f_p}\left(\frac{v_a d}{r_0} + \dot{r} + \frac{\dot{r}^2 d}{v_a r_0}\right) + \frac{\dot{r} d}{v_a} + \frac{\dot{r}^2 d^2}{2r_0 v_a^2}\right)\right], \tag{3.39}$$

where $\dot{r}$ is the actual target radial velocity.

3.7.2 Discrete azimuth compression

By using the approach of SAR compression as the application of a correlator [UMF86], one can write the output of the compression as

$$d(\tilde{m}) = \sum_{m=-\infty}^{\infty} r(m) s(m + \tilde{m}). \tag{3.40}$$

However, because of the compact support, the infinite limits can really be replaced by some appropriate choice of $a > 0$ and $b > 0$ such that

$$d(\tilde{m}) = \sum_{m=-a}^{b} r(m) s(m + \tilde{m}). \tag{3.41}$$

Substituting our representation for the reference function, (3.37), and the signal, (3.39), into (3.41) gives

$$\begin{aligned} d(\tilde{m}) &= \sum_{m=-a}^{b} \exp\left[j\beta\left(\frac{v_a^2 m^2}{2r_0 f_p^2} + \frac{m}{f_p}\left(\frac{v_a d}{r_0} + \dot{r}_f + \frac{\dot{r}_f^2 d}{v_a r_0}\right) + \frac{\dot{r}_f d}{v_a} + \frac{\dot{r}_f^2 d^2}{2r_0 v_a^2}\right)\right] \\ &\cdot \exp\left[-j\beta\left(r_0 + \frac{v_a^2(m+\tilde{m})^2}{2r_0 f_p^2} + \frac{(m+\tilde{m})}{f_p}\left(\frac{v_a d}{r_0} + \dot{r} + \frac{\dot{r}^2 d}{v_a r_0}\right) + \frac{\dot{r} d}{v_a} + \frac{\dot{r}^2 d^2}{2r_0 v_a^2}\right)\right] \\ &= \exp\left[j\beta\left(-r_0 + \frac{\dot{r}_f d}{v_a} + \frac{\dot{r}_f^2 d^2}{2r_0 v_a^2} - \frac{v_a^2 \tilde{m}^2}{2r_0 f_p^2} - \frac{\tilde{m}}{f_p}\left(\frac{v_a d}{r_0} + \dot{r} + \frac{\dot{r}^2 d}{v_a r_0}\right) - \frac{\dot{r} d}{v_a} - \frac{\dot{r}^2 d^2}{2r_0 v_a^2}\right)\right] \\ &\cdot \sum_{m=-a}^{b} \exp\left[-j\beta m\left(\frac{v_a^2 \tilde{m}}{r_0 f_p^2} - \frac{1}{f_p}\left(\dot{r}_f - \dot{r} + \frac{\dot{r}_f^2 d}{v_a r_0} - \frac{\dot{r}^2 d}{v_a r_0}\right)\right)\right]. \end{aligned} \tag{3.42}$$

Careful examination of the sum shows that it is a finite geometric series [FL99] of $a+b+1$ elements, so one derives, for only the sum part that

$$\begin{aligned} &\sum_{m=-a}^{b} \exp\left[-j\beta m\left(\frac{v_a^2 \tilde{m}}{r_0 f_p^2} - \frac{1}{f_p}\left(\dot{r}_f - \dot{r} + \frac{\dot{r}_f^2 d}{v_a r_0} - \frac{\dot{r}^2 d}{v_a r_0}\right)\right)\right] \\ &\quad = \exp\left[j\beta\left(\frac{v_a^2 \tilde{m}}{r_0 f_p^2} - \frac{1}{f_p}\left(\dot{r}_f - \dot{r} + \frac{\dot{r}_f^2 d}{v_a r_0} - \frac{\dot{r}^2 d}{v_a r_0}\right)\right)\left(\frac{a-b}{2}\right)\right] \\ &\quad \cdot \frac{\sin\left[\beta\left(\frac{v_a^2 \tilde{m}}{r_0 f_p^2} - \frac{1}{f_p}\left(\dot{r}_f - \dot{r} + \frac{\dot{r}_f^2 d}{v_a r_0} - \frac{\dot{r}^2 d}{v_a r_0}\right)\right)\left(\frac{a+b+1}{2}\right)\right]}{\sin\frac{\beta}{2}\left(\frac{v_a^2 \tilde{m}}{r_0 f_p^2} - \frac{1}{f_p}\left(\dot{r}_f - \dot{r} + \frac{\dot{r}_f^2 d}{v_a r_0} - \frac{\dot{r}^2 d}{v_a r_0}\right)\right)} \end{aligned} \tag{3.43}$$

Overall, the output of the correlator will have a magnitude given by the ratio of sinusoids, and a phase given by

$$\begin{aligned} \Theta(\tilde{m}) &= \left(\frac{a-b}{2}\right)\frac{\beta}{f_p}\left(\frac{v_a^2 \tilde{m}}{r_0 f_p} - \dot{r}_f + \dot{r} - \frac{\dot{r}_f^2 d}{v_a r_0} + \frac{\dot{r}^2 d}{v_a r_0}\right) \\ &\quad + \beta\left(-r_0 + \frac{\dot{r}_f d}{v_a} + \frac{\dot{r}_f^2 d^2}{2r_0 v_a^2} - \frac{v_a^2 \tilde{m}^2}{2r_0 f_p^2} - \frac{\tilde{m}}{f_p}\left(\frac{v_a d}{r_0} + \dot{r} + \frac{\dot{r}^2 d}{v_a r_0}\right) - \frac{\dot{r} d}{v_a} - \frac{\dot{r}^2 d^2}{2r_0 v_a^2}\right) \end{aligned} \tag{3.44}$$

3.7.3 Target position and phase

The correlator magnitude is given by

$$\frac{\sin\left[\beta\left(\frac{v_a^2 \tilde{m}}{r_0 f_p^2} - \frac{1}{f_p}\left(\dot{r}_f - \dot{r} + \frac{\dot{r}_f^2 d}{v_a r_0} - \frac{\dot{r}^2 d}{v_a r_0}\right)\right)\left(\frac{a+b+1}{2}\right)\right]}{\sin\frac{\beta}{2}\left(\frac{v_a^2 \tilde{m}}{r_0 f_p^2} - \frac{1}{f_p}\left(\dot{r}_f - \dot{r} + \frac{\dot{r}_f^2 d}{v_a r_0} - \frac{\dot{r}^2 d}{v_a r_0}\right)\right)}, \tag{3.45}$$

and by using l'Hôpital's rule, one finds a maximum value of $(a+b+1)/2$ when

$$\beta\left(\frac{v_a^2\tilde{m}}{r_0 f_p^2} - \frac{1}{f_p}(\dot{r}_f - \dot{r} + \frac{\dot{r}_f^2 d}{v_a r_0} - \frac{\dot{r}^2 d}{v_a r_0})\right) \rightarrow 2l\pi, \quad l \in \mathcal{I} \tag{3.46}$$

This periodicity gives rise to SAR image ambiguities. The greatest maximum occurs when there is maximal overlap between the recorded SAR signal and the reference function. At this point, one finds that $a = b$ at half the length of the reference function and that $\tilde{m} = 0$. These values give rise to the condition that

$$\dot{r}_f - \dot{r} + \frac{d}{v_a r_0}(\dot{r}_f^2 - \dot{r}^2) = \frac{2l\pi f_p}{\beta} \tag{3.47}$$

which, in turn, predicts that

$$\Theta(0) = -\beta r_0 + 2l\pi d\frac{f_p}{v_a}. \tag{3.48}$$

In words, a suitable choice for the reference function radial velocity can make it appear as though the SAR scene were processed with a stationary world matched filter. This appearance is only in the magnitude and position of the target. When $d \neq 0$, the symmetry is broken by the phase because it then depends on l. Stated another way, $\forall l \in \mathcal{I}$, $\exists \dot{r}_f$ such that $\tilde{m} = 0$. Since $\tilde{m} = 0$, the target is always at the same position as it is in the stationary image, (which is $\tilde{m} = 0$), and has the same magnitude because of l'Hôpital's rule. The phase of the target, however, is not the same if $d \neq 0$. Recall that for different choices of $\dot{r}_f$ the position of the target in the compressed SAR image is seen to change. A natural question is why not choose a different $\tilde{m} \neq 0$ to satisfy the condition of (3.46)? The answer, of course, is that $\tilde{m} \leq L$ where $L < \infty$ because of the compact support of the recorded signal and reference function.

3.7.4 Phase jump on Convair 580 SAR-GMTI data

Data collected by the CV580 has either been collected with a f_p/v_a ratio of 5.14 m^{-1} or 4.64 m^{-1} [LSG+02]. It has also been determined that the phase centre separation is $d = 0.2704$ m [LSG+02]. These parameters lead to a phase jump of either 8.7327 rad $= -220°$ or 7.8832 rad $= -268°$ **only** for the channel which is time resampled. The channel which is not time resampled has $d = 0$, so the phase does not change with the ambiguity. An interferogram will, of course, show the phase jumps.

3.7.5 Effect on fast moving targets

Let us imagine that a moving target is situated in one of the ambiguities because of its radial velocity. Estimation of the radial velocity with the interferometric phase, even unwrapped, will **not**

provide the correct radial velocity unless the phase jump is considered. Estimation of the radial velocity with non-coherent techniques such as time-frequency analysis or maximum likelihood will be free of the phase jump phenomenon, allowing the ambiguous region to be identified, which, in turn, will allow for correct accounting of the phase jump.

3.8 Summary

Moving target that have an along-track velocity component cause defocus error in the compressed image. This defocus error can be corrected by applying the map-drift autofocus algorithm adapted to moving targets. By estimating the displacement of the moving targets after injecting a phase ramp into the data, the Doppler rate of change can be estimated. In order to measure the target displacement at the sub-pixel level, the compressed image candidates are first clutter suppressed so that correlation maximization in the map drift algorithm corresponds only to the moving target.

Two forms of ambiguity are natural to a two-channel SAR system. The first is inherent in the sampling nature of the SAR system and corresponds to an along-track velocity component that has a wrap velocity of

$$\frac{f_p \lambda}{2}. \tag{3.49}$$

The second ambiguity is dependent on the physical phase centre separation between the two antenna apertures. It has a wrap velocity given by

$$\frac{v_a \lambda}{2d}. \tag{3.50}$$

A combination of these different wrap velocities can be used to mitigate the ambiguous velocity problem. In effect, the overall wrap velocity is raised to a sufficiently high value to unambiguously measure the across-track velocity component of ground moving targets.

The deramp or SPECAN algorithm can be used to SAR process the individual channels and has the capability of simultaneously combining exo-clutter suppression and multi-channel clutter suppression. In addition, the technique requires the computation of only one FFT, thereby reducing computation time.

CHAPTER 4

EIGEN DECOMPOSITION

This chapter presents a decomposition of the multi-channel sample covariance matrix into eigenvalues and a representation of the eigenvectors. It also presents an accompanying decomposition of the Wishart probability distribution of the sample covariance matrix into the distributions of the decomposition elements.

4.1 Motivation for new GMTI detectors based on eigen-decomposition of the covariance matrix

To motivate the decomposition, consider the linear filter depicted in figure 4.1 at slow time index m. By expressing the linear filter and the input channels as column vectors,

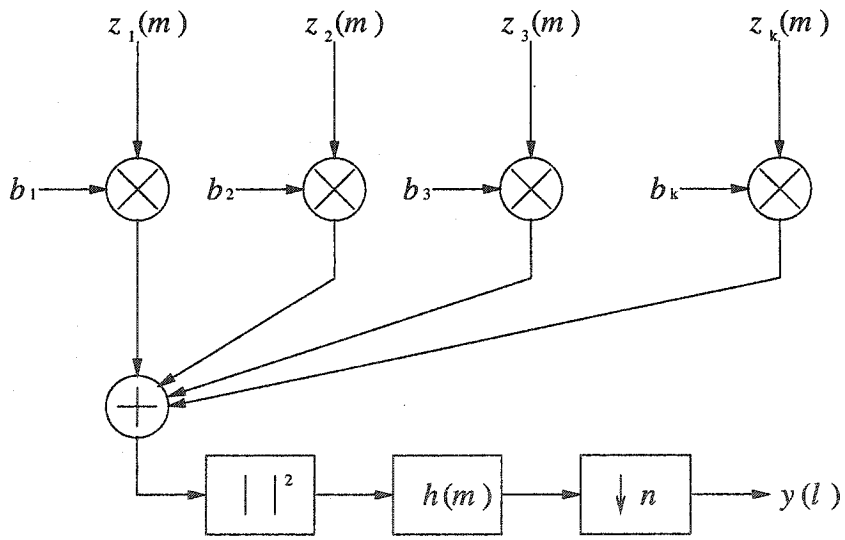

Figure 4.1. Processing schematic: multiple SAR channels for GMTI.

$$\vec{z}(m) = \begin{bmatrix} z_1(m) \\ z_2(m) \\ \vdots \\ z_k(m) \end{bmatrix}, \quad \vec{b}(m) = \begin{bmatrix} b_1(m) \\ b_2(m) \\ \vdots \\ b_k(m) \end{bmatrix}, \tag{4.1}$$

the quantity passed to the square law detector can be expressed as

$$y(m) = \vec{b}^{\dagger}(m)\vec{z}(m). \tag{4.2}$$

The adaptive nature of Space Time Adaptive Processing (STAP) is incorporated in the time dependence of the filter $\vec{b}(m)$; however, for the sake of compact notation, the time dependence, from here onwards, shall be omitted. If $\vec{z} = \vec{c} + \vec{s}$, where $\vec{c}$ represents zero-mean complex Gaussian clutter plus white sensor noise, and $\vec{s}$ represents a statistically independent target, then one can calculate the statistical expectation of $|y|^2$ as

$$\begin{aligned} \mathcal{E}\{|y|^2\} &= \mathcal{E}\{|\vec{b}^{\dagger}\vec{z}|^2\} \\ &= \vec{b}^{\dagger}\mathcal{E}\{\vec{z}\vec{z}^{\dagger}\}\vec{b} \\ &= \vec{b}^{\dagger}\boldsymbol{R}\vec{b}, \\ &= \vec{b}^{\dagger}(\boldsymbol{R}_c + \boldsymbol{R}_s)\vec{b}, \end{aligned} \tag{4.3}$$

where $\boldsymbol{R}_c$ is the clutter plus noise covariance matrix, and $\boldsymbol{R}_s$ is the target covariance matrix. The linear processing filter that maximizes the Signal to Clutter plus noise Ratio (SCR) is given by $\vec{b} = \gamma \boldsymbol{R}_c^{-1}\vec{s}$ where $\gamma \in \mathcal{C}$, [Kle98]. Adoption of this approach leads to the optimal SCR of $\vec{s}^{\dagger}\boldsymbol{R}_c^{-1}\vec{s}$ for a discrete target.

In the 2-channel case, when the data are balanced in power (the average power of the signal measured by each antenna is the same) and the correlation between channels is $\rho \approx 1$, the optimal linear filter technique leads to the Displaced Phase Centre Antenna approach to GMTI. The prescription for DPCA is to subtract the two data channels and apply some norm, such as the magnitude squared, that maps the complex difference to $\mathcal{R}$. Data that are stationary should be the same for both channels and therefore mostly cancel out.

It has been shown in [Kle98] that by examining a Cholesky factorization of $\boldsymbol{R}_c$, the optimal linear filter, $\vec{b} = \gamma \boldsymbol{R}_c^{-1}\vec{s}$, operates by eliminating the known correlations in the clutter process. This filter, however, does not "whiten" the moving target signal; hence, residual correlations may be emphasized and used to detect the moving target.

Residual moving target correlations can be further emphasized by increasing the number of apertures (so that more residual correlations can be utilized). Alternatively, or additionally, one can average neighbouring samples in the data space with the effect of reducing detected clutter variance at the expense of resolution. The decimated image is given by

$$y(l) = \frac{1}{n} \sum_{m=nl}^{n(l+1)-1} |\vec{b}(m)^\dagger \vec{z}(m)|^2, \tag{4.4}$$

where the data have been decimated by the factor n and the slow time index is $l = \text{floor}(m/n)$.

Eigen-decomposition of the 2-channel sample covariance matrix yields

$$\mathcal{E}\{|y|^2\} = \vec{b}^\dagger (s_1 \vec{v}_1 \vec{v}_1^\dagger + s_2 \vec{v}_2 \vec{v}_2^\dagger) \vec{b} \tag{4.5}$$

where $\boldsymbol{R}$, has eigenvalues $s_1 > s_2 > 0$, and corresponding eigenvectors, $\vec{v}_1$ and $\vec{v}_2$.

Instead of maximizing the SCR, another criterion for GMTI is to minimize $|y|^2$ when only clutter is present. When $\rho \approx 1$, most of the clutter energy is contained in the largest eigenvalue, and a non-trivial solution to $\min_{\vec{b}}\{\vec{b}^\dagger \boldsymbol{R} \vec{b}\}$ is to choose $\vec{b}$ to be the second eigenvector of $\boldsymbol{R}$ giving a minimum value of s_2. Indeed, when the channels are balanced in power, and when there is no average phase difference between the channels, the second eigenvector will always be

$$\vec{v}_2 = \begin{bmatrix} 1 \\ -1 \end{bmatrix}. \tag{4.6}$$

In this case, choosing $\vec{b} = \vec{v}_2$ is equivalent to specifying DPCA.

The value of s_2 depends upon the degree of singularity of $\boldsymbol{R}$, which, in turn, depends upon whether or not a target is present. If it is assumed that the clutter covariance matrix is practically singular, then the addition of $\boldsymbol{R}_s$ increases the linear independence of the rows of $\boldsymbol{R}_c + \boldsymbol{R}_s$ as compared to $\boldsymbol{R}_c$, thereby raising the value of the smallest eigenvalue of $\boldsymbol{R}$. The smallest eigenvalue, Λ_2, of the *estimated* covariance matrix, $\hat{\boldsymbol{R}}$, is therefore proposed as a GMTI metric. Additionally, since the overall covariance matrix, as an addition of target and clutter covariance matrices, has a structure different from clutter alone, each element of a complete eigen-decomposition of $\hat{\boldsymbol{R}}$ is considered for GMTI.

It will be shown that the DPCA and the ATI phase can be considered as combinations of the elements of the eigen-decomposition of $\hat{\boldsymbol{R}}$. It will also be shown that the probability density

function for the sample covariance matrix can be decomposed to yield the density functions for each component.

4.2 Decomposition of covariance matrix into GMTI metrics

This section presents a decomposition of the multi-channel sample covariance matrix into eigenvalues and a representation of the eigenvectors. It also presents an accompanying decomposition of the Wishart probability distribution of the sample covariance matrix into the distributions of the decomposition elements. It is essential to specify the method of decomposition as the mathematical structure is required to create a meaningful probability measure for the eigenvectors.

The task at hand is to decompose the sample covariance matrix defined by

$$\hat{\boldsymbol{R}} = \sum_{m=0}^{n-1} \vec{z}(m)\vec{z}^{\dagger}(m). \tag{4.7}$$

Since $\hat{\boldsymbol{R}}$ is Hermitian, real eigenvalues are assured and the diagonalization gives

$$\hat{\boldsymbol{R}} = \boldsymbol{U}\boldsymbol{D}\boldsymbol{U}^{\dagger}, \tag{4.8}$$

where $\boldsymbol{D}$ is a diagonal matrix of eigenvalues and $\boldsymbol{U}^{\dagger}\boldsymbol{U} = \boldsymbol{U}^{-1}\boldsymbol{U} = \boldsymbol{I}_k$.

To allow for the definition of a probability distribution of eigenvalues, it is necessary to define the order of eigenvalues in $\boldsymbol{D}$. One such arrangement is in order of largest eigenvalue to smallest, $0 < \Lambda_k \leq \Lambda_{k-1} \ldots \leq \Lambda_1 < \infty$,

$$\boldsymbol{D} = \begin{bmatrix} \Lambda_1 & 0 & \ldots & 0 \\ 0 & \Lambda_2 & \ldots & 0 \\ \vdots & \vdots & \ddots & \vdots \\ 0 & 0 & \ldots & \Lambda_k \end{bmatrix} \tag{4.9}$$

Since $\hat{\boldsymbol{R}}$ has k^2 random entries, corresponding to k real diagonal elements and $k(k-1)/2$ complex off-diagonal elements (each with random real and imaginary components), the transformation to k eigenvalues has to be accompanied by $k(k-1)$ random parameters, α_i, that represent the random eigenvectors. These eigenvectors align to form the random matrix $\boldsymbol{U}$.

It is well known that the matrices $\boldsymbol{U}$ that diagonalize a Hermitian matrix are unitary and that $|\det \boldsymbol{U}| = 1$. These matrices can be represented by a subset of the generators of the special unitary group of dimension k, SU(k) as shown in [CP96]. The generator matrices for the 2×2 case and the 3×3 case are the Pauli spin matrices and the Dirac matrices, respectively.

The generator matrices for SU(2) and SU(3) are listed in (4.10) and (4.11) respectively. This is one approach adopted, for example, in [CP96].

$$\sigma_1 = \begin{bmatrix} 0 & 1 \\ 1 & 0 \end{bmatrix}, \ \sigma_2 = \begin{bmatrix} 0 & -j \\ j & 0 \end{bmatrix}, \ \sigma_3 = \begin{bmatrix} 1 & 0 \\ 0 & -1 \end{bmatrix}, \tag{4.10}$$

$$\begin{aligned} \beta_1 &= \begin{bmatrix} 0 & 1 & 0 \\ 1 & 0 & 0 \\ 0 & 0 & 0 \end{bmatrix}, \ \beta_2 = \begin{bmatrix} 0 & -j & 0 \\ j & 0 & 0 \\ 0 & 0 & 0 \end{bmatrix}, \ \beta_3 = \begin{bmatrix} 1 & 0 & 0 \\ 0 & -1 & 0 \\ 0 & 0 & 0 \end{bmatrix}, \\ \beta_4 &= \begin{bmatrix} 0 & 0 & 1 \\ 0 & 0 & 0 \\ 1 & 0 & 0 \end{bmatrix}, \ \beta_5 = \begin{bmatrix} 0 & 0 & -j \\ 0 & 0 & 0 \\ j & 0 & 0 \end{bmatrix}, \ \beta_6 = \begin{bmatrix} 0 & 0 & 0 \\ 0 & 0 & 1 \\ 0 & 1 & 0 \end{bmatrix}, \\ \beta_7 &= \begin{bmatrix} 0 & 0 & 0 \\ 0 & 0 & -j \\ 0 & j & 0 \end{bmatrix}, \ \beta_8 = \frac{1}{\sqrt{3}} \begin{bmatrix} 1 & 0 & 0 \\ 0 & 1 & 0 \\ 0 & 0 & -2 \end{bmatrix}. \end{aligned} \tag{4.11}$$

$\boldsymbol{U}$ is represented in the 2×2 case by using 3 real parameters $\alpha_1, \alpha_2, \alpha_3$,

$$\boldsymbol{U} = \exp\left(j \sum_{l=1}^{3} \alpha_l \sigma_l \right), \tag{4.12}$$

and for the 3×3 case using 8 real parameters $\alpha_i | i \in \{1, 2, \ldots, 8\}$ as

$$\boldsymbol{U} = \exp\left(j \sum_{l=1}^{8} \alpha_l \beta_l \right). \tag{4.13}$$

Further simplification is made by noting that the diagonal basis matrices, namely, σ_3, β_3 and β_8 all have weight zero [CP96], as $\boldsymbol{U}$ diagonalizes a Hermitian matrix. Thus, for the 2×2 case, two parameters are required, and for the 3×3 case, six parameters are required.

Another representation, similar in form to that outlined in [Gir90], is realized with the aid of the following Hermitian unitary matrix

$$\boldsymbol{P} = \begin{bmatrix} \cos\theta & e^{j\delta} \sin\theta \\ e^{-j\delta} \sin\theta & -\cos\theta \end{bmatrix}, \tag{4.14}$$

which is a complex Householder reflection matrix, [GVL96]. Construct the following matrix

$$\boldsymbol{P}^{mn} = \begin{bmatrix} \ddots & \vdots & \vdots & \ddots & \vdots & \vdots & \ddots \\ \dots 1 & 0 & 0 & \dots & 0 & 0 & 0 \dots \\ \dots 0 & \cos\theta_{mn} & 0 & \dots & 0 & e^{j\delta_{mn}}\sin\theta_{mn} & 0 \dots \\ \dots 0 & 0 & 1 & \dots & 0 & 0 & 0 \dots \\ \ddots & \vdots & \vdots & \ddots & \vdots & \vdots & \ddots \\ \dots 0 & 0 & 0 & \dots & 1 & 0 & 0 \dots \\ \dots 0 & e^{-j\delta_{mn}}\sin\theta_{mn} & 0 & \dots & 0 & -\cos\theta_{mn} & 0 \dots \\ \dots 0 & 0 & 0 & \dots & 0 & 0 & 1 \dots \\ \ddots & \vdots & \vdots & \ddots & \vdots & \vdots & \ddots \end{bmatrix}, \tag{4.15}$$

where m and n are indices not powers, and where $\cos\theta_{mn}$ is on row m, column m, $e^{j\delta_{mn}}\sin\theta_{mn}$ is on row m, column n, $e^{-j\delta_{mn}}\sin\theta_{mn}$ is on row n, column m, and $-\cos\theta_{mn}$ is on row n, column n. Of course, $n > m$. If one post-multiplies $\boldsymbol{U}^\dagger$ by $\boldsymbol{P}^{12}$, one can choose $\theta_{12} \in [0, \pi/2)$ and $\delta_{12} \in [-\pi, \pi)$ such that the element on row 1, column 2 of the product is zero. One can then post-multiply $\boldsymbol{U}^\dagger\boldsymbol{P}^{12}$ by $\boldsymbol{P}^{13}$ and choose θ_{13} and δ_{13} such that the element on row 1, column 3 of the product is zero. The element on row 1, column 2 will still be zero. This process can be carried out until all the entries except for the one on row 1, column 1 are zero. Since $\boldsymbol{P}^{mn\dagger}\boldsymbol{P}^{mn} = \boldsymbol{I}_k$, $\boldsymbol{U}^{1\dagger} = \boldsymbol{U}^\dagger\prod_{n=2}^{k}\boldsymbol{P}^{1n}$ is also unitary. Therefore, the elements $U^{1\dagger}_{m1}$ for $m > 1$ will also be zero, i.e.,

$$\boldsymbol{U}^{1\dagger} = \begin{bmatrix} e^{j\omega_1} & \vec{0}^\dagger \\ \vec{0} & \boldsymbol{H}^1 \end{bmatrix}. \tag{4.16}$$

The procedure can be continued until $\boldsymbol{U}^{k\dagger}$ is diagonal with diagonal elements of the form $e^{j\omega_i}$, $i = 1\dots, k$. The above procedure describes a QR decomposition of $\boldsymbol{U}^\dagger$, and given that $\boldsymbol{U}^\dagger$ is unitary, the result is a diagonal matrix of complex phases. These phase residues are extra degrees of freedom for $\boldsymbol{U}^\dagger$. That is, if

$$\boldsymbol{E}^\dagger = \begin{bmatrix} e^{j\omega_1} & 0 & 0 & \dots & 0 \\ 0 & e^{j\omega_2} & 0 & \dots & 0 \\ 0 & 0 & e^{j\omega_3} & \dots & 0 \\ \vdots & \vdots & \vdots & \ddots & \vdots \\ 0 & 0 & 0 & \dots & e^{j\omega_k} \end{bmatrix} \tag{4.17}$$

pre-multiplies $\boldsymbol{U}^\dagger$, then

$$\boldsymbol{UEDE}^\dagger\boldsymbol{U}^\dagger = \boldsymbol{UDU}^\dagger. \tag{4.18}$$

These unwanted degrees of freedom can be systematically eliminated by choosing the diagonal elements to be real. By using this representation for $\boldsymbol{U}$, one can derive the Jacobian of the transformation by evaluating (4.24).

An example of a set of the matrices $\boldsymbol{P}^{mn}$, for the 3×3 case, is

$$\begin{aligned}
\boldsymbol{P}^{12} &= \begin{bmatrix} \cos\theta_{12} & e^{j\delta_{12}}\sin\theta_{12} & 0 \\ e^{-j\delta_{12}}\sin\theta_{12} & -\cos\theta_{12} & 0 \\ 0 & 0 & 1 \end{bmatrix}, \\
\boldsymbol{P}^{13} &= \begin{bmatrix} \cos\theta_{13} & 0 & e^{j\delta_{13}}\sin\theta_{13} \\ 0 & 1 & 0 \\ e^{-j\delta_{13}}\sin\theta_{13} & 0 & -\cos\theta_{13} \end{bmatrix}, \\
\boldsymbol{P}^{23} &= \begin{bmatrix} 1 & 0 & 0 \\ 0 & \cos\theta_{23} & e^{j\delta_{23}}\sin\theta_{23} \\ 0 & e^{-j\delta_{23}}\sin\theta_{23} & -\cos\theta_{23} \end{bmatrix}.
\end{aligned} \tag{4.19}$$

All matrices $\boldsymbol{U}$ that diagonalize a complex 3×3 Hermitian matrix can be written as $\boldsymbol{U}^\dagger\boldsymbol{P}^{12}\boldsymbol{P}^{13}\boldsymbol{P}^{23} = \boldsymbol{I}_3$, or $\boldsymbol{U} = \boldsymbol{P}^{12}\boldsymbol{P}^{13}\boldsymbol{P}^{23}$.

4.3 Joint probability distribution for the two-channel system

For the remainder of this thesis, the covariance matrix in the 2×2 case is written as

$$\boldsymbol{R} = \begin{bmatrix} \sigma_1^2 & \sigma_1\sigma_2\rho e^{j\Phi} \\ \sigma_1\sigma_2\rho e^{-j\Phi} & \sigma_2^2 \end{bmatrix}, \tag{4.20}$$

where σ_1^2 denotes the power of the first channel, σ_2^2 denotes the power of the second channel, and $\rho e^{j\Phi}$ the complex correlation between channels. For stationary terrain $\Phi = 0$. Later we focus on a power balanced system where $\sigma_1^2 = \sigma_2^2 = \sigma^2$. The diagonalisation transformation of the sample covariance matrix is given by

$$\hat{\boldsymbol{R}} = \begin{bmatrix} \hat{R}_{11} & \hat{R}_{12} \\ \hat{R}^\dagger{}_{12} & \hat{R}_{22} \end{bmatrix} = \boldsymbol{UDU}^\dagger = \begin{bmatrix} u_{11} & u_{12} \\ u_{12}{}^\dagger & u_{22} \end{bmatrix} \begin{bmatrix} \Lambda_1 & 0 \\ 0 & \Lambda_2 \end{bmatrix} \begin{bmatrix} u_{11} & u_{12} \\ u_{12}{}^\dagger & u_{22} \end{bmatrix}, \tag{4.21}$$

where the four random variables, $\hat{R}_{11}$, $\hat{R}_{22}$, Real($\hat{R}_{12}$) and Imag($\hat{R}^{\dagger}{}_{12}$), are transformed into two random eigenvalues Λ_1, Λ_2, and the two variables Δ and Θ that describe $\boldsymbol{U}$. Representation (4.15), as opposed to (4.12), is used for $\boldsymbol{U}$. Of importance is the fact that $\boldsymbol{U}$ can be written as a linear combination of the Pauli spin matrices

$$\begin{aligned} \boldsymbol{U} &= \sin\Theta\cos\Delta \begin{bmatrix} 0 & 1 \\ 1 & 0 \end{bmatrix} - \sin\Theta\sin\Delta \begin{bmatrix} 0 & -j \\ j & 0 \end{bmatrix} + \cos\Theta \begin{bmatrix} 1 & 0 \\ 0 & -1 \end{bmatrix} \\ &= \sin\Theta\cos\Delta\boldsymbol{\sigma}_1 - \sin\Theta\sin\Delta\boldsymbol{\sigma}_2 + \cos\Theta\boldsymbol{\sigma}_3. \end{aligned} \tag{4.22}$$

In fact, $\boldsymbol{U}$ can be represented by a point on the unit sphere when the basis "vectors" are the Pauli spin matrices (the above $\boldsymbol{\sigma}$'s are different from the previously encountered channel powers, σ_1 and σ_2). Thus, Δ and Θ are the two random variables that describe the random eigenvector matrix $\boldsymbol{U}$.

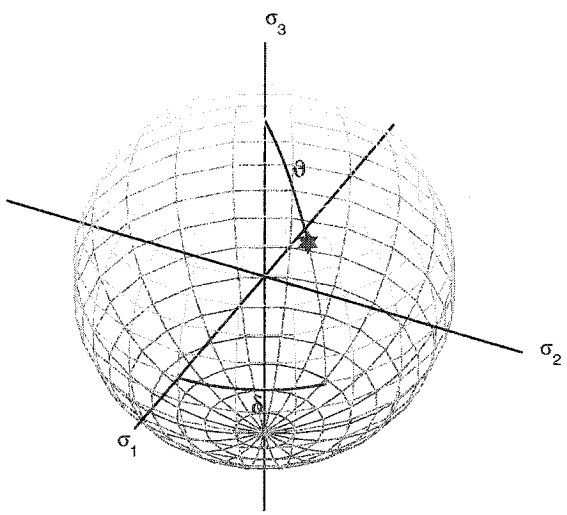

Figure 4.2. Diagonalising matrix is represented by a point on the 3-dimensional sphere for the 2×2 Hermitian matrix case.

After expanding $\boldsymbol{U}^{\dagger}\hat{\boldsymbol{R}}\boldsymbol{U}$, the desired transformation is revealed as

$$\begin{aligned} \Lambda_1 &= \frac{1}{2}\left(\hat{R}_{11} + \hat{R}_{22} + \sqrt{4|\hat{R}_{12}|^2 + (\hat{R}_{11} - \hat{R}_{22})^2}\right) \\ \Lambda_2 &= \frac{1}{2}\left(\hat{R}_{11} + \hat{R}_{22} - \sqrt{4|\hat{R}_{12}|^2 + (\hat{R}_{11} - \hat{R}_{22})^2}\right) \\ \Delta &= \arg(\hat{R}_{12}) \\ \Theta &= \frac{1}{2}\arctan\left(\frac{2|\hat{R}_{12}|}{\hat{R}_{11} - \hat{R}_{22}}\right), \end{aligned} \tag{4.23}$$

where $0 < A_2 < A_1 < \infty$, $\Delta \in [-\pi, \pi)$ and $\Theta \in [0, \pi/2)$.

Figures 4.3 to 4.6 illustrate the decomposition elements as images. The largest eigenvalue looks very much like a SAR image of the terrain. The small eigenvalue, figure 4.4 picks out a convoy of moving vehicles, as do Δ and Θ. The latter three metrics emphasise a highway that runs down the left side of the scene. On this highway, one sees blurred and spread responses from targets moving relatively quickly in the radar along-track direction. The difference in the Doppler rate of change for the highway targets compared to stationary terrain causes the misfocus.

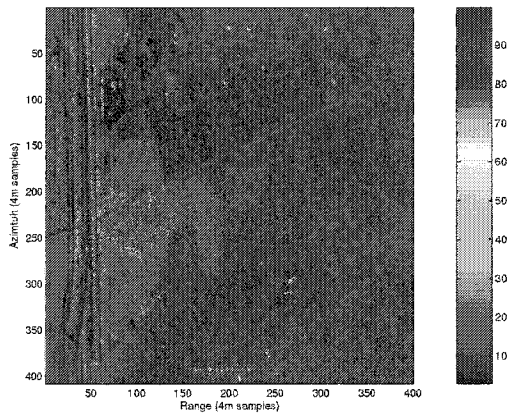

Figure 4.3. λ_1 eigenvalue image of terrain. Image from *m2l3p3*.

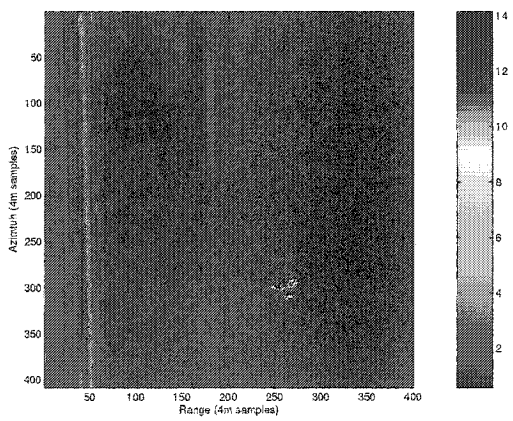

Figure 4.4. λ_2 eigenvalue image of terrain. Image from *m2l3p3*.

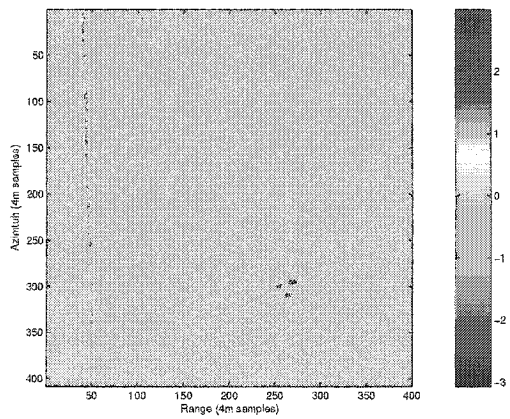

Figure 4.5. Δ image of terrain. Image from *m2l3p3*.

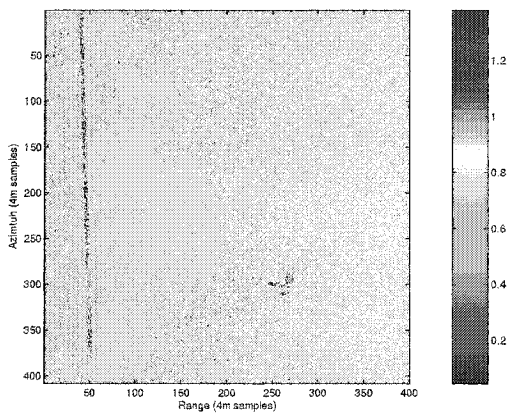

Figure 4.6. Θ image of terrain. Image from *m2l3p3*.

4.4 Joint probability distribution of the decomposition elements

This section discusses and examines a decomposition of the probability distribution of the sample covariance matrix into the probability distributions of its eigenvalues and eigenvectors.

We follow the same lines as Wigner [Wig67] and Mehta [Meh67]; however, a notable difference between what is presented in this paper centres on the explicit requirement to calculate the eigenvector matrix, U. In many considerations of the distribution of the eigenvalues of a Wishart matrix, the channels are assumed to be statistically identical and independent [Meh67, JN02, Gra02, HT03, Ede89]. This assumption eliminates the need for an expression for U when considering the probability distribution of eigenvalues since it cancels out. Statistical correlation, or the non-identity covariance matrix has been considered by James [Jam64], where his results are expressed in terms of zonal polynomials, which, although mathematically interesting are generally intractable. This

section expresses the marginal and joint probability distributions of eigenvalues and eigenvectors without recourse to the zonal polynomials for the 2×2 case.

The probability density function of the sample covariance matrix is the previously discussed expression of (2.14).

As with most transformations of random variables, a Jacobian has to be computed. This task is undertaken in appendix B.1 leading to the following result

$$\det \boldsymbol{J} = \left[\prod_{p,q}(\Lambda_q - \Lambda_p)^2\right] \det \begin{bmatrix} \begin{bmatrix} S_{pq}^{1(0)} & \cdots \\ S_{pq}^{2(0)} & \cdots \\ \vdots & \ddots \\ S_{pq}^{k(k-1)(0)} & \cdots \end{bmatrix} & \begin{bmatrix} S_{pq}^{1(1)} & \cdots \\ S_{pq}^{2(1)} & \cdots \\ \vdots & \ddots \\ S_{pq}^{k(k-1)(1)} & \cdots \end{bmatrix} \end{bmatrix}, \tag{4.24}$$

where

$$\boldsymbol{S}^i = \boldsymbol{U}^\dagger \frac{\partial \boldsymbol{U}}{\partial \alpha_i}, \tag{4.25}$$

and the indices are such that $k \geq p > q \geq 1$. The superscript (0) means the *real part of* while the superscript (1) means the *imaginary part of*. The actual Jacobian is, of course, $|\det \boldsymbol{J}|$.

4.5 Statistics for two-channel case

In order to calculate the Jacobian of the two-dimensional transformation, the upper off-diagonal elements of

$$\boldsymbol{U}\frac{\partial \boldsymbol{U}^\dagger}{\partial \Theta} = \begin{bmatrix} 0 & e^{j\Delta} \\ e^{-j\Delta} & 0 \end{bmatrix}, \tag{4.26}$$

and

$$\boldsymbol{U}\frac{\partial \boldsymbol{U}^\dagger}{\partial \Delta} = \begin{bmatrix} -j\sin^2\Theta & je^{j\Delta}\sin\Theta\cos\Theta \\ je^{-j\Delta}\sin\Theta\cos\Theta & j\sin^2\Theta. \end{bmatrix} \tag{4.27}$$

are required for insertion into (4.24). The yield is

$$\det \begin{bmatrix} \cos\Delta & \sin\Delta \\ -\sin\Delta\cos\Theta\sin\Theta & \cos\Delta\cos\Theta\sin\Theta \end{bmatrix} = \frac{\sin(2\Theta)}{2}. \tag{4.28}$$

The Jacobian is therefore

$$(\lambda_1 - \lambda_2)^2 \left|\frac{\sin(2\Theta)}{2}\right|. \tag{4.29}$$

By substituting the transformed variables into (2.14), the pdf for the eigenvalues and eigenvectors can be written, for the 2×2 case, as

$$f_{\Lambda_1,\Lambda_2,\Theta,\Delta}(\lambda_1,\lambda_2,\theta,\delta) = \frac{(\lambda_1\lambda_2)^{n-2}(\lambda_1-\lambda_2)^2}{2\pi\Gamma(n)\Gamma(n-1)\det(\boldsymbol{R})^n}|\sin 2\theta|\mathrm{etr}\left(-\boldsymbol{U}^\dagger\boldsymbol{R}^{-1}\boldsymbol{U}\begin{bmatrix}\lambda_1 & 0\\ 0 & \lambda_2\end{bmatrix}\right), \tag{4.30}$$

where $\mathrm{etr}() = \exp(\mathrm{Tr}(\cdot))$ stands for exponential trace. The limits are $0 < \lambda_2 \leq \lambda_1 < \infty$, $\delta \in [-\pi, \pi)$, and $\theta \in [0, \pi/2)$.

4.6 Marginal probability distributions of the two-channel decomposition elements

From (4.23) we see that the random variable Δ is none other than the well known interferometric phase. The marginal probability density function for the phase has been previously stated in (2.17).

The marginal pdf for Θ, which we shall term the "similarity", can be computed when it is assumed that the two channels are balanced in power (i.e. that the power in each channel is the same). We use the term similarity because (4.23) shows that when $\hat{R}_{11} = \hat{R}_{22}$, then $\Theta = \pi/4$, hence the degree to which the two channel realizations are similar is reflected in this metric. Marginalization, as carried out in appendix B.2, yields

$$f_\Theta(\theta) = (1-\rho^2)^n \sin(2\theta)\Big[2n\ {}_2F_1(1+n, 1/2; 1; \rho^2\sin^2(2\theta)) + (1-2n)\ {}_2F_1(n, 1/2; 1; \rho^2\sin^2(2\theta))\Big]. \tag{4.31}$$

The assumption that the two channels are balanced in power is not very demanding. If the channels are not balanced, they may be balanced by estimating the difference between their transfer functions as a function of time and adjusting one to the other as done in [Gie03].

The joint pdf for Θ and Δ can also be computed in closed form as done in appendix B.3 to yield

$$f_{\Theta\Delta}(\theta,\delta) = \frac{\sin(2\theta)\Gamma(n+1/2)(1-\rho^2)^n}{2\pi^{3/2}\Gamma(n+2)}\,{}_2F_1(2n, 3; n+2; (1+\rho\cos(\delta-\Phi)\sin(2\theta))/2), \tag{4.32}$$

where Φ is defined in (4.20). This joint probability density function is illustrated in figure 4.7 for the parameters $n = 5$, and $\rho = 0.95$. While (4.32) cannot be factored to show that the two variables are independent, the joint pdf plot is highly elliptical.

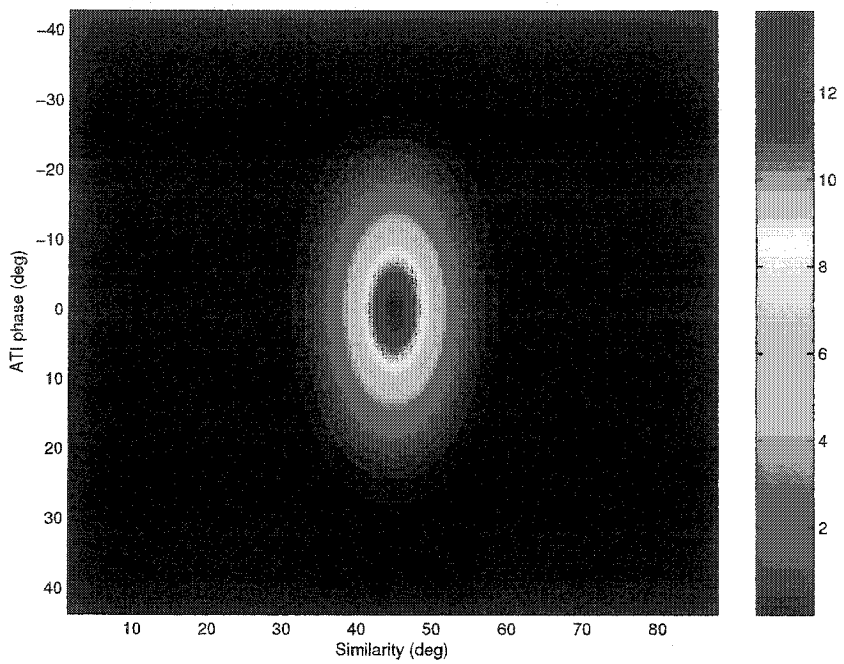

Figure 4.7. Joint pdf of similarity and ATI phase with $\rho = 0.95, \sigma^2 = 1, n = 5$.

The probability density function of A_2 is computed in appendix B.5 with the result

$$\begin{aligned} f_{A_2}(\lambda_2) = &\frac{(\lambda_2/s_2)^{n-2} e^{-\lambda_2/s_2} \Gamma(n, \lambda_2/s_1)}{\Gamma(n)\Gamma(n-1)(s_1 - s_2)} \left(\frac{s_1}{s_2} - \frac{\lambda_2/s_2}{n-1} \right) \\ &- \frac{(\lambda_2/s_1)^{n-2} e^{-\lambda_2/s_1} \Gamma(n, \lambda_2/s_2)}{\Gamma(n)\Gamma(n-1)(s_1 - s_2)} \left(\frac{s_2}{s_1} - \frac{\lambda_2/s_1}{n-1} \right), \end{aligned} \tag{4.33}$$

where,

$$\Gamma(n, z) = \int_z^\infty x^{n-1} e^{-x} \mathrm{d}x \tag{4.34}$$

is an[1] incomplete gamma function, and $s_1 > s_2$ are the eigenvalues of the underlying covariance matrix. [GR00].

The joint density function of A_2 and the ATI phase has not been calculated in closed form due to the mathematical difficulty of doing so. However, using numerical methods, it is possible to calculate the joint density function by evaluating the joint density function of similarity, ATI phase and A_2.

$$\begin{aligned} f_{A_2,\Delta}(\lambda_2, \delta) = &\frac{\lambda_2^{n-2}}{2\pi\Gamma(n)\Gamma(n-1)(s_1 s_2)^n} \cdot \\ &\int_0^{\pi/2} \sin(2\theta) e^{-B\lambda_2} \left[\frac{\Gamma(n+1, A\lambda_2)}{A^{n+1}} - \frac{2\lambda_2 \Gamma(n, A\lambda_2)}{A^n} + \frac{\lambda_2^2 \Gamma(n-1, A\lambda_2)}{A^{n-1}} \right] \mathrm{d}\theta, \end{aligned} \tag{4.35}$$

[1]The article "an" is used instead of "the" because there are different definitions of the incomplete gamma function.

where,

$$A = \frac{(s_1 + s_2) - (s_1 - s_2)\cos\delta\sin(2\theta)}{2s_1 s_2}$$
$$B = \frac{(s_1 + s_2) + (s_1 - s_2)\cos\delta\sin(2\theta)}{2s_1 s_2}. \tag{4.36}$$

To determine the degree of independence between A_2 and the ATI phase, the "independent" joint

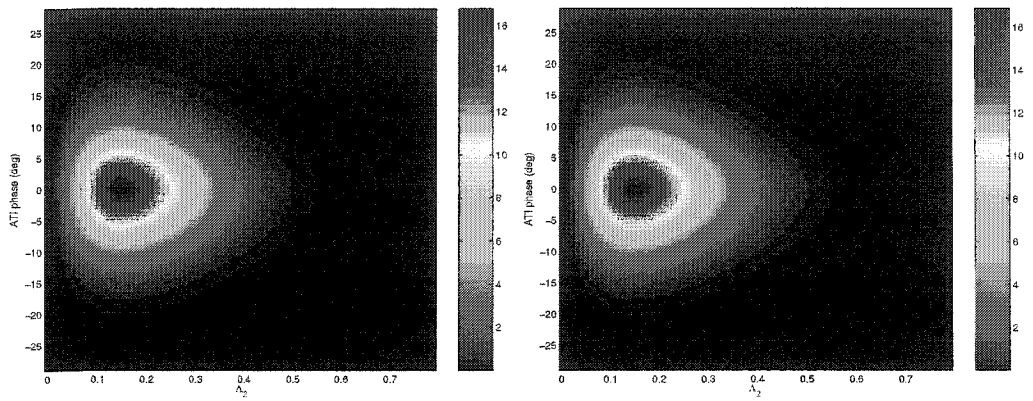

(a) Joint probability density

(b) Product of marginal densities

Figure 4.8. Comparison of joint density and product of marginal densities of A_2 and ATI phase with $\rho = 0.95, \sigma^2 = 1, n = 5$.

density function, or the product of the marginal density functions, can be computed and compared with the numerical approximation of the joint density function. Figure 4.8 shows that the joint density function and the product of marginal density functions are very similar. Although the joint probability density function cannot be factored to show that the metrics are independent, figure 4.8 indicates only a small statistical dependence.

4.7 Comparison with simulated and real SAR data

Measured and simulated SAR data are compared with the decomposition elements. These comparisons validate the underlying physical model as the theoretical probability distributions accurately model the data histograms. Both the measured and simulated data illustrate the capability of the decomposition elements to detect moving targets.

4.7.1 Similarity

In figure 4.6, Θ is computed for real SAR data and illustrated as an image. This image demonstrates that Θ has a response to moving targets. Such a response makes sense as the expression for Θ has the quantity $(\hat{R}_{11} - \hat{R}_{22})$ in the denominator of the arctangent function (4.23). Since $\hat{R}_{11}$ and $\hat{R}_{22}$ correspond to the powers of the two channels, if the two channels are highly correlated, then θ will be close to $\pi/4$. On the other hand, if they are not highly correlated, the angle will be closer to zero.

It turns out that Θ is not a good measure of whether or not a target is present. Its degree of sensitivity to moving targets is too low (see section 7.2). But it does provide information about what probably is not a target. The power of the test for the presence of a target increases if we can determine that certain detections with the interferometric phase are false alarms. This may prove critical for masking out false alarms in urban areas where many targets are detected only on the basis of the interferometric phase.

The fit of the theoretical marginal pdf of the similarity and some real SAR data is shown in figure 4.9. It is clear that the fit with the real data is excellent.

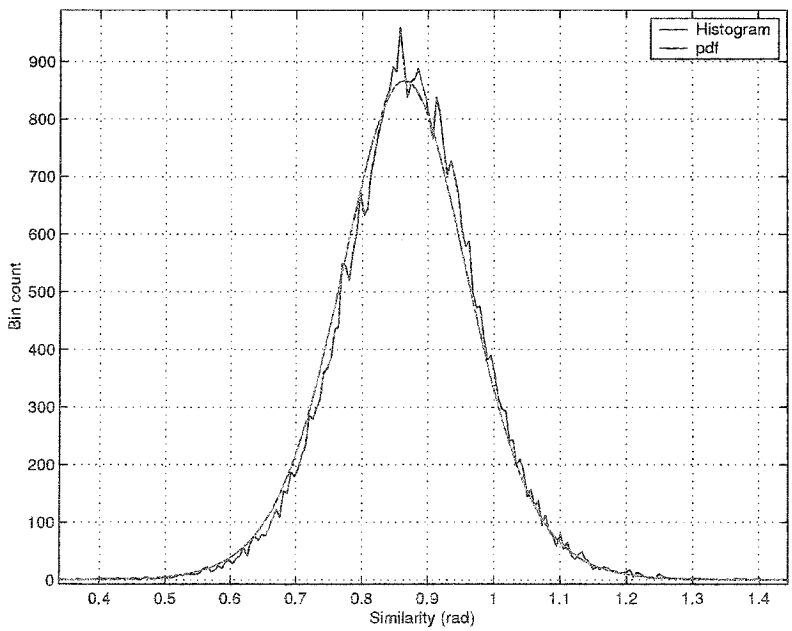

Figure 4.9. Theoretical marginal pdf for Θ plotted with real SAR data. Data extracted from file *m2li1p5* ($\rho = 0.98$, $n = 6.4754$)

4.7.2 Small eigenvalue

In figure 4.10, Λ_2 has been computed for a simulated and measured data set. The simulated data were generated by assuming that the signals were circularly Gaussian distributed with a given covariance matrix. The correlated data were created by using a Cholesky decomposition of the supplied covariance matrix and Matlab's^{TM}randn function. In essence, the data represent the situation of perfect homogeneity. In the adjacent image, Λ_2 for real SAR data is compared to the theoretical probability density function. Clearly, the histogram and the pdf are not identical. The reason for the mismatch stems from the fact that the real SAR data are not perfectly homogeneous and therefore the eigenvalue statistic must be "texturized", as well explained in [Gie01a]. In this thesis the ideas of [Gie01a] are adopted and modified in a new proposed texture statistic presented in chapter 5.

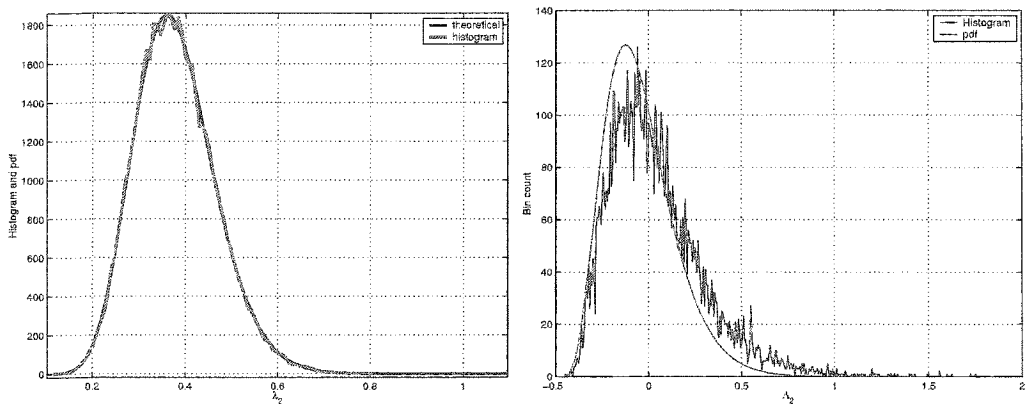

Figure 4.10. Histograms of simulated, measured and theoretical distributions of Λ_2. Left, simulated $n = 20$, $\rho = 0.95$, $\sigma^2 = 8$; right, measured $n = 6.4754$, $\rho = 0.98$, $\sigma^2 = 1580$.

4.8 Recombination of decomposition elements into new GMTI metrics

In anticipation of application to SAR-GMTI, elements can be recombined into new GMTI metrics. Two such recombinations are called the independent unitary phase detector and the hyperbolic detector.

4.8.1 Independent unitary phase detector

It has been demonstrated in section 4.3 that the similarity and the ATI phase are capable of detecting moving targets. We have already seen from (4.22) that these two variables can be represented as coordinates on the unit sphere. We now introduce a new metric that simultaneously

combines the GMTI information previously conveyed by the separate metrics and transforms the two random variables into two new, statistically independent, random variables.

Recall from section 4.2 that the basic building block of the diagonalizing matrix is given by

$$\boldsymbol{P} = \begin{bmatrix} \cos\theta & e^{j\delta}\sin\theta \\ e^{-j\delta}\sin\theta & -\cos\theta \end{bmatrix}. \tag{4.37}$$

This matrix is unitary, traceless and has determinant -1. It is special unitary in all regards except for the sign of the determinant. It was stated in section 4.2, that any 2×2 diagonalizing matrix can be represented in the form

$$\begin{bmatrix} \cos\theta & e^{j\delta}\sin\theta \\ e^{-j\delta}\sin\theta & -\cos\theta \end{bmatrix} \begin{bmatrix} e^{j\eta_1} & 0 \\ 0 & e^{j\eta_2} \end{bmatrix}, \tag{4.38}$$

where η_1 and η_2 are spurious phases that play no role in the diagonalization operation. Let $\mathcal{G}$ be the set of matrices that can be written in the form of (4.38). The product of $\boldsymbol{P}_1, \boldsymbol{P}_2 \in \mathcal{G}$. The proof of this is already given in section 4.2, but we explicitly show it here again.

Proof. Let $\boldsymbol{P}_3^\dagger = \boldsymbol{P}_1\boldsymbol{P}_2$, then $\boldsymbol{P}_3^\dagger\boldsymbol{P}_3 = \boldsymbol{P}_1\boldsymbol{P}_2\boldsymbol{P}_2^\dagger\boldsymbol{P}_1^\dagger = \boldsymbol{I}_2$. Now post-multiply $\boldsymbol{P}_3$ by

$$\begin{bmatrix} \cos\theta & e^{j\delta}\sin\theta \\ e^{-j\delta}\sin\theta & -\cos\theta \end{bmatrix}, \tag{4.39}$$

to get

$$\begin{aligned} \boldsymbol{P}_3^\dagger \begin{bmatrix} \cos\theta & e^{j\delta}\sin\theta \\ e^{-j\delta}\sin\theta & -\cos\theta \end{bmatrix} &= \begin{bmatrix} p_{11} & p_{12} \\ p_{21} & p_{22} \end{bmatrix} \begin{bmatrix} \cos\theta & e^{j\delta}\sin\theta \\ e^{-j\delta}\sin\theta & -\cos\theta \end{bmatrix} \\ &= \begin{bmatrix} p_{11}\cos\theta + p_{12}e^{-j\delta}\sin\theta & p_{11}e^{j\delta}\sin\theta - p_{12}\cos\theta \\ p_{21}\cos\theta + p_{22}e^{-j\delta}\sin\theta & p_{21}e^{j\delta}\sin\theta - p_{22}\cos\theta \end{bmatrix}. \end{aligned} \tag{4.40}$$

To make the upper off-diagonal element zero, set

$$\begin{aligned} 0 &= p_{11}e^{j\delta}\sin\theta - p_{12}\cos\theta \\ 0 &= r_{11}e^{j\delta_{11}}e^{j\delta}\sin\theta - r_{12}e^{j\delta_{12}}\cos\theta \end{aligned}, \tag{4.41}$$

where $p_{11} = r_{11} \exp j\delta_{11}$ and $p_{12} = r_{12} \exp j\delta_{12}$. Choose δ such that $\delta_{11} + \delta = \delta_{12}$ to make exponential phases cancel out, and choose θ such that

$$\begin{aligned} 0 &= r_{11} \sin\theta - r_{12} \cos\theta \\ \tan\theta &= \frac{r_{12}}{r_{11}} \end{aligned} \tag{4.42}$$

At this stage, one finds that the matrix product yields a quantity of the form

$$\begin{bmatrix} q_{11} & 0 \\ q_{21} & q_{22} \end{bmatrix}. \tag{4.43}$$

But we know that $\boldsymbol{P}_3^\dagger \boldsymbol{P}_3 = \boldsymbol{I}_2$, therefore

$$\begin{bmatrix} q_{11}^* & q_{21}^* \\ 0 & q_{22}^* \end{bmatrix} \begin{bmatrix} q_{11} & 0 \\ q_{21} & q_{22} \end{bmatrix} = \begin{bmatrix} q_{11}^* q_{11} + q_{21}^* q_{21} & q_{21}^* q_{22} \\ q_{22}^* q_{21} & q_{22}^* q_{22} \end{bmatrix} = \begin{bmatrix} 1 & 0 \\ 0 & 1 \end{bmatrix}. \tag{4.44}$$

This means $|q_{22}| = 1$. Therefore $q_{21} = 0$, and $|q_{11}| = 1$. We now see that the matrix product of (4.40) yields a diagonal matrix of values on the complex unit circle. Therefore

$$\begin{aligned} \boldsymbol{P}_3^\dagger \begin{bmatrix} \cos\theta & e^{j\delta}\sin\theta \\ e^{-j\delta}\sin\theta & -\cos\theta \end{bmatrix} &= \begin{bmatrix} e^{-j\eta_1} & 0 \\ 0 & e^{-j\eta_2} \end{bmatrix} \\ &\Longrightarrow \\ \boldsymbol{P}_3 &= \begin{bmatrix} \cos\theta & e^{j\delta}\sin\theta \\ e^{-j\delta}\sin\theta & -\cos\theta \end{bmatrix} \begin{bmatrix} e^{j\eta_1} & 0 \\ 0 & e^{j\eta_2} \end{bmatrix} \end{aligned} \tag{4.45}$$

□

Any $\boldsymbol{P}_1 \in \mathcal{G}$ has inverse $\boldsymbol{P}_1^\dagger$ which, again, can be written in the form of (4.38). Choosing $\theta = 0, \delta = 0, \eta_1 = 0, \eta_2 = \pi$ reveals the identity element. Thus the set of all such matrices forms a group under the operation of matrix multiplication.

In the derivation of the probability distribution of the eigenvalues in appendix B.5, the invariance of the Haar measure was used to demonstrate that the eigenvalue distribution only depends upon

the eigenvalues of the underlying covariance matrix. This property becomes more clear by recalling that the argument of the exponential in the Wishart distribution can be written as

$$E = \mathrm{Tr}\left(\boldsymbol{U}^{\dagger}\boldsymbol{R}^{-1}\boldsymbol{U}\begin{bmatrix}\lambda_1 & 0\\ 0 & \lambda_2\end{bmatrix}\right) \tag{4.46}$$

$$= \mathrm{Tr}\left(\boldsymbol{U}^{\dagger}\boldsymbol{V}\begin{bmatrix}s_1^{-1} & 0\\ 0 & s_2^{-1}\end{bmatrix}\boldsymbol{V}^{\dagger}\boldsymbol{U}\begin{bmatrix}\lambda_1 & 0\\ 0 & \lambda_2\end{bmatrix}\right) \tag{4.47}$$

$$= \mathrm{Tr}\left(\boldsymbol{W}^{\dagger}\begin{bmatrix}s_1^{-1} & 0\\ 0 & s_2^{-1}\end{bmatrix}\boldsymbol{W}\begin{bmatrix}\lambda_1 & 0\\ 0 & \lambda_2\end{bmatrix}\right), \tag{4.48}$$

where $\boldsymbol{V}$ diagonalizes $\boldsymbol{R}$, $\boldsymbol{U}$ diagonalizes $\hat{\boldsymbol{R}}$, s_1 and s_2 are the eigenvalues of $\boldsymbol{R}$ and $\boldsymbol{W} = \boldsymbol{V}^{\dagger}\boldsymbol{U} \in \mathcal{G}$ can be written as

$$\boldsymbol{W} = \begin{bmatrix}\cos\vartheta & e^{j\varphi}\sin\vartheta\\ e^{-j\varphi}\sin\vartheta & -\cos\vartheta\end{bmatrix}. \tag{4.49}$$

when the diagonal matrix of complex exponentials is neglected. This approach transforms the original random variables describing the eigenvectors into a new set of random variables. The transformation is implicitly included in the derivation of appendix B.5 leading to the following expression for the trace component of the complex Wishart distribution

$$\mathrm{Tr}\left(\boldsymbol{W}^{\dagger}\begin{bmatrix}s_1^{-1} & 0\\ 0 & s_2^{-1}\end{bmatrix}\boldsymbol{W}\begin{bmatrix}\lambda_1 & 0\\ 0 & \lambda_2\end{bmatrix}\right) = \left(\frac{\lambda_1}{s_1}+\frac{\lambda_2}{s_2}\right)\cos^2\vartheta + \left(\frac{\lambda_1}{s_2}+\frac{\lambda_2}{s_1}\right)\sin^2\vartheta. \tag{4.50}$$

Equation (4.50) does not depend on the new random variable φ. It should be made explicit that the $\sin(2\theta)$ factor in the Jacobian of (4.29) transforms into $\sin(2\vartheta)$. This can be seen by either returning to the initial derivation of the Jacobian using the new random variables, (ϑ, φ), or actually computing the Jacobian of the transformation. Since φ does not appear in the transformed joint probability density function, $(\delta, \theta) \rightarrow (\varphi, \vartheta)$ in (4.30), and since it isn't in the Jacobian of the transformation, one can immediately conclude that not only is it independent of all the other random variables, but that it is uniformly distributed. The uniform distribution does not permit it to convey any GMTI information. Therefore one can conclude that the GMTI capability of both the similarity and the ATI phase have been combined into the metric ϑ.

The new detector which we call the Independent Unitary Phase (IUP) detector is thus defined by the new variable ϑ. Figure 4.11 illustrates this metric on the same data used in figure 4.3.

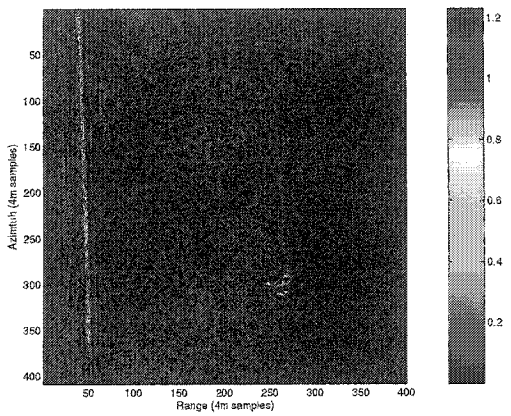

Figure 4.11. Independent unitary phase image of terrain. Image from *m2l3p3*.

The joint probability distribution between Λ_2 and ϑ is calculated in appendix B.6 to give the following result

$$f_{\vartheta\Lambda_2}(\vartheta,\lambda_2) = \frac{2\sin(2\vartheta)}{\Gamma(n)\Gamma(n-1)(s_1 s_2)^n}\lambda_2^{2n-1}e^{-(s_1^{-1}+s_2^{-1})\lambda_2}\Psi(3,n+2;A\lambda_2), \tag{4.51}$$

where

$$A = \frac{\cos^2\vartheta}{s_1} + \frac{\sin^2\vartheta}{s_2}, \tag{4.52}$$

and $\Psi(a,b;z)$ is a degenerate hypergeometric function of the second kind (formula 9.210 in [GR00]).

The probability density function of the unitary phase is calculated in appendix B.4 to give

$$f_\vartheta(\vartheta) = \frac{2\sin(2\vartheta)\Gamma(2n)(s_1 s_2)^n}{\Gamma(n)\Gamma(n-1)(s_1+s_2)^{2n}}\frac{\Gamma(n-1)}{\Gamma(n+2)}{}_2F_1(2n,3;n+2;\frac{s_2\sin^2\vartheta + s_1\cos^2\vartheta}{s_1+s_2}). \tag{4.53}$$

4.8.2 Hyperbolic detector

Anticipation of the results of sections 7.2 and 7.3 which show that moving targets can be detected with both Λ_2 and ϑ, motivates the proposal of a new combined detector,

$$m_h = {\Lambda_2}^p\left(\frac{\cos^2\vartheta}{s_1} + \frac{\sin^2\vartheta}{s_2}\right), \tag{4.54}$$

where p serves to weight the contribution from Λ_2. A theoretical analysis of the optimal choice for p is beyond the scope of this thesis. It would have to consider the properties of both Λ_2 and

m_h under different conditions; for example, for different types of terrain. From here onwards, for the sake of mathematical tractability, we choose $p = 1$. By making a formal change of variables $V = \cos^2\vartheta/s_1 + \sin^2\vartheta/s_2$, one sees that threshold values for $\Lambda_2 \cdot V \gtrless \gamma$ correspond to hyperbolas in the $\Lambda_2 \times V$ plane, hence the name "hyperbolic" detector. Figure 4.12 shows an image of the hyperbolic metric for the same data used in figure 4.3.

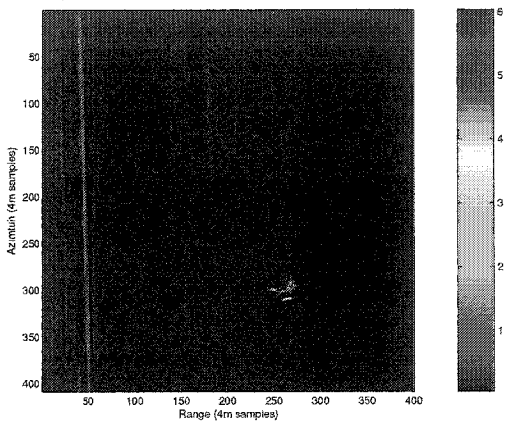

Figure 4.12. Hyperbolic metric image of terrain. Image from *m2l3p3*.

The probability distribution of the hyperbolic detector is calculated in appendix B.7 for the special case $p = 1$ with the following result

$$f_U(u) = \frac{2u^{2n-1}\Psi(3, n+2; u)}{\Gamma(n)\Gamma(n-1)(s_1 - s_2)}\Big[s_1 e^{-u\mathrm{Tr}\boldsymbol{R}/s_1}(s_2/s_1)^n\Psi(1, 2n; u\mathrm{Tr}\boldsymbol{R}/s_1) - s_2 e^{-u\mathrm{Tr}\boldsymbol{R}/s_2}(s_1/s_2)^n\Psi(1, 2n; u\mathrm{Tr}\boldsymbol{R}/s_2)\Big]. \quad (4.55)$$

Given that the distribution function is known, implementation of CFAR detection with this powerful new detector is possible.

4.8.3 Modified eigen-projection

In the same vein as the eigenprojection of [GL03], a comparison can also be made as follows: consider the eigen-decompositions of the true clutter covariance matrix, $\boldsymbol{R} = \boldsymbol{V}\boldsymbol{S}\boldsymbol{V}^\dagger$, and of the clutter plus target sample covariance matrix, $\hat{\boldsymbol{R}} = \boldsymbol{U}\boldsymbol{D}\boldsymbol{U}^\dagger$. Since we can find $\boldsymbol{W}$ such that $\boldsymbol{W}\boldsymbol{V}^\dagger = \boldsymbol{U}^\dagger$, we can write that $\hat{\boldsymbol{R}} = \boldsymbol{V}\boldsymbol{W}^\dagger\boldsymbol{D}\boldsymbol{W}\boldsymbol{V}^\dagger = \boldsymbol{V}\boldsymbol{F}\boldsymbol{V}^\dagger$. Thus,

$$\boldsymbol{R} = \sum_{l=1}^{k} s_l \vec{v}_l \vec{v}_l^{\dagger}, \tag{4.56}$$

$$\hat{\boldsymbol{R}} = \sum_{l=1}^{k} \sum_{m=1}^{k} F_{lm} \vec{v}_l \vec{v}_m^{\dagger} \tag{4.57}$$

$$= \sum_{l=1}^{k} F_{ll} \vec{v}_l \vec{v}_l^{\dagger} + \sum_{l=1}^{k} \sum_{m \neq l}^{k} F_{lm} \vec{v}_l \vec{v}_m^{\dagger}, \tag{4.58}$$

where $\vec{v}_k$ are the eigenvectors that align to form $\boldsymbol{V}$, and $s_1 > s_2 > \ldots s_k > 0$ are the eigenvalues of $\boldsymbol{R}$. By considering that the outer product matrices, $\vec{v}_l \vec{v}_l^{\dagger}$, $l \in \{1, 2, \ldots, k\}$, form a basis, the clutter eigenvalues form a vector that can be compared to the sample matrix eigenvalue vector. The eigen-projection metric is illustrated in figure 4.13. The cross term outer products matrices, $\vec{v}_l \vec{v}_m^{\dagger}$,

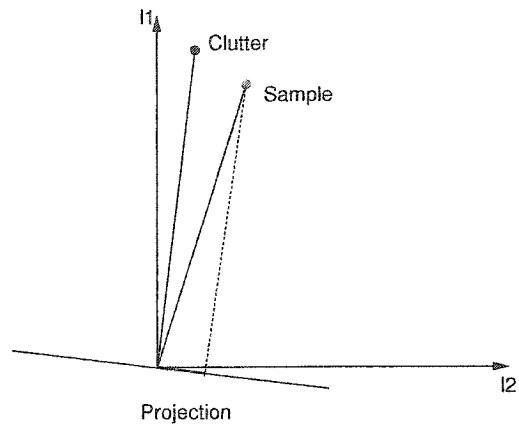

Figure 4.13. Illustration of eigen-projection metric.

$l \neq m$, represent quantities with zero energy as their traces vanish.

The eigen-projection method can be used to find the component of the sample covariance matrix that is orthogonal to the clutter covariance matrix. Since $\sqrt{\mathrm{Tr}(\boldsymbol{D}^2)} = \sqrt{\mathrm{Tr}(\boldsymbol{R}^{\dagger}\boldsymbol{R})}$ is the length of the clutter energy vector, and the inner product of the sample matrix vector and the clutter vector is given by $\mathrm{Tr}(\hat{\boldsymbol{R}}^{\dagger}\boldsymbol{R})$, the component of the sample covariance matrix energy vector that is perpendicular to the clutter covariance matrix energy vector is given by the diagonal elements of

$$\boldsymbol{M} = \boldsymbol{F} - \frac{\mathrm{Tr}(\hat{\boldsymbol{R}}^{\dagger}\boldsymbol{R})}{\mathrm{Tr}(\boldsymbol{R}^{\dagger}\boldsymbol{R})}\boldsymbol{D}. \tag{4.59}$$

Numerous metrics are contained in $\boldsymbol{M}$. Since $\boldsymbol{D}$ is diagonal, the off-diagonal elements of $\boldsymbol{F}$ are automatic candidates. Additionally, the metric defined by

$$m_\perp = \sum_{l=1}^{k} M_{ll}^\dagger M_{ll}, \tag{4.60}$$

detects targets that have energy components on the subspace orthogonal to the clutter energy vector.

In the 2×2 case, when it is assumed that the channels are power balanced, application of the above prescription leads to a perpendicular component given by

$$\begin{aligned} m_\perp = s_1[\lambda_1(1 - \cos\delta\sin(2\theta)) + \lambda_2(1 + \cos\delta\sin(2\theta))] \\ -s_2[\lambda_1(1 + \cos\delta\sin(2\theta)) + \lambda_2(1 - \cos\delta\sin(2\theta))]. \end{aligned} \tag{4.61}$$

In this case we have used that

$$\boldsymbol{R} = \begin{bmatrix} \sigma^2 & \rho\sigma^2 \\ \rho\sigma^2 & \sigma^2 \end{bmatrix}, \tag{4.62}$$

where the phase of stationary terrain is assumed equal to zero (i.e. $\phi = 0$ in (2.10)). For the special case where $\boldsymbol{R}$ is singular (or nearly so $\rho \approx 1$), one can substitute $s_2 = 0$ and conclude that

$$m_\perp \propto m_{DPCA}, \tag{4.63}$$

as seen by comparing with (7.4). In the general case, however, the detector can be written equivalently as

$$\begin{aligned} m_\perp &= s_1 \sum_{m=0}^{n-1} |z_1(m) - z_2(m)|^2 - s_2 \sum_{m=0}^{n-1} |z_1(m) + z_2(m)|^2 \\ &= \sum_{m=0}^{n-1} \vec{z}^\dagger(m) \boldsymbol{V}^\dagger \begin{bmatrix} -s_2 & 0 \\ 0 & s_1 \end{bmatrix} \boldsymbol{V} \vec{z}(m) \\ &= \mathrm{Tr}\left(\boldsymbol{V}^\dagger \begin{bmatrix} -s_2 & 0 \\ 0 & s_1 \end{bmatrix} \boldsymbol{V} \hat{\boldsymbol{R}} \right), \end{aligned} \tag{4.64}$$

where the second line above takes the trace of both sides. Equation (4.64) specifies that the detector is the multilooked (by n) difference between two detected $|\cdot|^2$ linearly filtered outputs of the input data. It is not possible to re-write (4.64) as a single linear filter of the input data that is subsequently passed to a detector and decimator, hence, in a sense, the aggregate operation is non-linear.

In magnitude, $m_\perp$, represents the length of the component of the sample covariance matrix that is orthogonal to the average clutter covariance matrix. As for the sign, examples show that bright

stationary targets have large negative values while moving targets have large positive values. Since λ_2 detects targets quite well, this behavior is consistent.

Figure 4.14 illustrates the eigenvalue projection metric as an image on the same data presented in figure 4.3. It is seen that the projection metric responds to targets quite well.

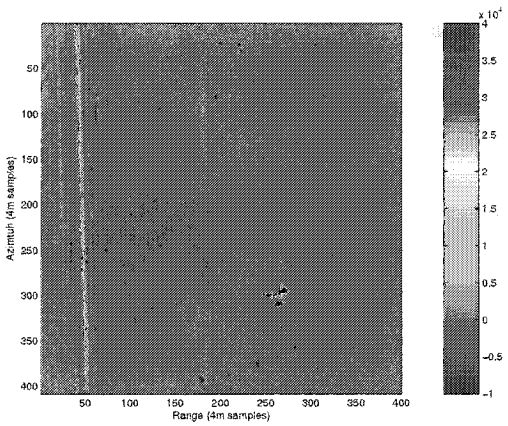

Figure 4.14. Eigen-projection metric image of terrain. Image from *m2l3p3*.

4.8.4 Eigenprojection statistics

In the homogenous case, the statistics of the eigenprojector detector follow from the zero-mean complex Gaussian statistics of the correlated antenna samples. Although presented here as a double integral, it can be stated as a single integral where the integrand involves an incomplete gamma function [GR00]. The following result is derived in appendix B.8.

$$f_{M_\perp}(m_\perp) = \begin{cases} \int_0^{\infty} \int_{\frac{-m_\perp}{2s_2}+\frac{s_1\lambda_2}{s_2}}^{\infty} f_{\lambda_1,\lambda_2,m_\perp}(\lambda_1,\lambda_2,m_\perp)\mathrm{d}\lambda_1\mathrm{d}\lambda_2, & \text{for } m_\perp \leq 0, \\ \int_0^{\frac{m_\perp}{2(s_1-s_2)}} \int_{\frac{m_\perp}{2s_1}+\frac{s_2\lambda_2}{s_1}}^{\infty} f_{\lambda_1,\lambda_2,m_\perp}(\lambda_1,\lambda_2,m_\perp)\mathrm{d}\lambda_1\mathrm{d}\lambda_2 + & \\ \int_{\frac{m_\perp}{2(s_1-s_2)}}^{\infty} \int_{\frac{-m_\perp}{2s_2}+\frac{s_1\lambda_2}{s_2}}^{\infty} f_{\lambda_1,\lambda_2,m_-}(\lambda_1,\lambda_2,m_\perp)\mathrm{d}\lambda_1\mathrm{d}\lambda_2, & \text{for } m_\perp > 0, \end{cases} \tag{4.65}$$

where

$$f_{\lambda_1,\lambda_2,m_\perp}(\lambda_1,\lambda_2,m_\perp) = \frac{(\lambda_1\lambda_2)^{n-2}(\lambda_1-\lambda_2)}{4\sigma^2\Gamma(n)\Gamma(n-1)(s_1s_2)^n} \exp\left(-\frac{\lambda_1}{\sigma^2}-\frac{\lambda_2}{\sigma^2}-\frac{m_\perp\rho}{2s_1s_2}\right). \tag{4.66}$$

Figure 4.15 illustrates this probability distribution for $s_1 = 100$ and $s_2 = 1.5$, and the number of looks, $n = 3.5$.

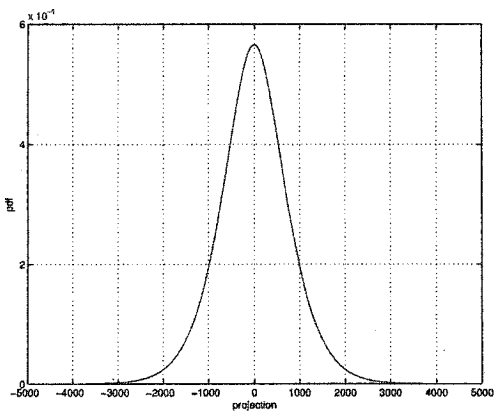

Figure 4.15. Sample probability distribution of projection metric

4.9 Detection using more than two channels

The purpose of this section is to demonstrate that the mathematics for the two-channel system can be extended to the three channels. Unfortunately this extension rapidly introduces algebraic complexity; thus, the final result is left as a joint probability distribution function. Application of the joint probability density function to real data could be accomplished with numerical integration. Most of the analysis in this section for a three-channel system relied upon a symbolic mathematics software package.

A concern that immediately arises stems from the uniqueness of the random variables introduced in (4.19). It has been shown that three spurious phase terms arise when the diagonalizing matrix is written as $\boldsymbol{U} = \boldsymbol{P}^{23}\boldsymbol{P}^{13}\boldsymbol{P}^{12}$. Is there only one choice for $\theta_{ij} \in [0, \pi/2)$, $\delta_{ij} \in [-\pi, \pi)$ when the eigenvalues are defined in descending order, the spurious phase terms are discarded, and the order of the $\boldsymbol{P}^{ij}$ is chosen in a fixed pattern?

Consider $\boldsymbol{U}\boldsymbol{D}\boldsymbol{U}^\dagger = \boldsymbol{R}$ and $\boldsymbol{V}\boldsymbol{D}\boldsymbol{V}^\dagger = \boldsymbol{R}$. Assuming that $\boldsymbol{D}$ contains the eigenvalues in descending order, one can derive that $[\boldsymbol{D}, \boldsymbol{U}^\dagger\boldsymbol{V}] = 0$ where the square brackets denote the commutation operator,

$[\boldsymbol{X}, \boldsymbol{Y}] = \boldsymbol{XY} - \boldsymbol{YX}$. Writing, for the time being, that $\boldsymbol{E} = \boldsymbol{U}^\dagger \boldsymbol{V}$, one can then derive the following expressions

$$(\lambda_1 - \lambda_2) E_{12} = 0, \tag{4.67}$$

$$(\lambda_1 - \lambda_3) E_{13} = 0, \tag{4.68}$$

$$(\lambda_2 - \lambda_3) E_{23} = 0. \tag{4.69}$$

Since the $(\lambda_i - \lambda_j)$ differences are zero measure events, one is almost sure that $E_{ij} = 0$ (for $i \neq j$), and, hence, that $\boldsymbol{E}$ is almost surely diagonal. Therefore, $\exists \boldsymbol{Q}$ diagonal such that $\boldsymbol{Q} = \boldsymbol{U}^\dagger \boldsymbol{V}$. By denoting the diagonal terms of $\boldsymbol{Q}$ as $r_m e^{j\xi_m}$ and inserting into $\boldsymbol{U}^\dagger \boldsymbol{R} \boldsymbol{U} = \boldsymbol{Q} \boldsymbol{V}^\dagger \boldsymbol{R} \boldsymbol{V} \boldsymbol{Q}^\dagger = \boldsymbol{Q} \boldsymbol{D} \boldsymbol{Q}^\dagger = \boldsymbol{D}$, it is revealed that $|r_i| = 1$, and that the matrix $\boldsymbol{Q}$ only corresponds to the spurious phase terms encountered earlier. There is thus only one way of writing $\boldsymbol{U}$ when $\boldsymbol{Q} = \boldsymbol{I}_k$.

By exploiting the invariance of the Haar measure, the covariance matrix in the general $k \times k$ formulation can be assumed to be diagonal. Practical assimilation of this condition simply corresponds to a unitary transformation of the diagonalizing matrix. That is, if the probability density function of $\boldsymbol{U}$ is known for a diagonal covariance matrix, then application to a practical situation would involve first estimating the covariance matrix (if it isn't already known) followed by a unitary transformation on $\boldsymbol{U}$. In mathematical terms, if the distribution of a unitary transformation of $\boldsymbol{U}$ is known, then either the real data is made useful by applying the unitary transformation, or the sample space in the probability measure is transformed.

Therefore, without loss of generality, the covariance matrix can be assumed to be diagonal and the expression for the Jacobian in the 3×3 case, determined from appendix B.1, is

$$|\det J| = (\lambda_1 - \lambda_2)^2 (\lambda_1 - \lambda_3)^2 (\lambda_2 - \lambda_3)^2 \frac{\sin(2\theta_2) \cos^2 \theta_2 \sin(2\theta_1) \sin(2\theta_3)}{8}, \tag{4.70}$$

where s_1, s_2, s_3 are the eigenvalues of $\boldsymbol{R}$ in no particular order. Inserting the above two expressions into the Wishart distribution leads to

$$f_{\Lambda_1\Lambda_2\Lambda_3\Theta_1\Theta_2\Theta_3\Delta_1\Delta_2\Delta_3}(\lambda_1,\lambda_2,\lambda_3,\theta_1,\theta_2,\theta_3,\delta_1,\delta_2,\delta_3)$$
$$= \frac{(\lambda_1\lambda_2\lambda_3)^{n-3}(\lambda_1-\lambda_2)^2(\lambda_1-\lambda_3)^2(\lambda_2-\lambda_3)^2}{2\pi\Gamma(n)\Gamma(n-1)\Gamma(n-2)(s_1s_2s_3)^n} \cdot \frac{\sin(2\theta_2)\cos^2\theta_2\sin(2\theta_1)\sin(2\theta_3)}{8}$$
$$\operatorname{etr}\left(-U^\dagger \begin{bmatrix} s_1^{-1} & 0 & 0 \\ 0 & s_2^{-1} & 0 \\ 0 & 0 & s_3^{-1} \end{bmatrix} U \begin{bmatrix} \lambda_1 & 0 & 0 \\ 0 & \lambda_2 & 0 \\ 0 & 0 & \lambda_3 \end{bmatrix}\right), \quad (4.71)$$

where

$$U = \begin{bmatrix} \cos\theta_1 & e^{j\delta_1}\sin\theta_1 & 0 \\ e^{-j\delta_1}\sin\theta_1 & -\cos\theta_1 & 0 \\ 0 & 0 & 1 \end{bmatrix} \begin{bmatrix} \cos\theta_2 & 0 & e^{j\delta_2}\sin\theta_2 \\ 0 & 1 & 0 \\ e^{-j\delta_2}\sin\theta_2 & 0 & -\cos\theta_2 \end{bmatrix} \begin{bmatrix} 1 & 0 & 0 \\ 0 & \cos\theta_3 & e^{j\delta_3}\sin\theta_3 \\ 0 & e^{-j\delta_3}\sin\theta_3 & -\cos\theta_3 \end{bmatrix}. \quad (4.72)$$

Expansion of the exponential argument of the Wishart distribution yields

$$\begin{aligned} E = {} & s_3^{-1}\lambda_1 + s_2^{-1}\lambda_2 + s_1^{-1}\lambda_3 \\ & + (s_1^{-1}-s_2^{-1})\frac{(\lambda_2-\lambda_3)}{2}\sin(2\theta_1)\sin\theta_2\sin(2\theta_3)\cos(\delta_1+\delta_3-\delta_2) \\ & + (s_1^{-1}-s_2^{-1})(\lambda_2-\lambda_3)[\cos^2\theta_1+\cos^2\theta_3-2\cos^2\theta_1\cos^2\theta_3+\cos^2\theta_1\cos^2\theta_2\cos^2\theta_3] \\ & + (s_2^{-1}-s_3^{-1})(\lambda_2-\lambda_3)\cos^2\theta_2\cos^2\theta_3 \\ & + (s_1^{-1}-s_2^{-1})(\lambda_1-\lambda_2)\cos^2\theta_1\cos^2\theta_2 \\ & + (s_2^{-1}-s_3^{-1})(\lambda_1-\lambda_2)\cos^2\theta_2. \quad (4.73) \end{aligned}$$

Since the eigenvalues of the covariance matrix in this analysis have not been constrained to any particular order, a tremendous simplification can be made if it is assumed that two of the eigenvalues are the same. This is the case for a multi-channel system where all cross-correlations coefficients are identical. For example, by assuming that $s_1 = s_2$, the δ_i, $i \in \{1,2,3\}$, dependence in (4.73) vanishes.

4.10 Conclusion

The covariance matrix of two or more SAR channels contains all of the information required to detect a moving target. Therefore, the analysis of the matrix by decomposition methods is proposed as an alternative to conventional detection methods including DPCA and ATI. The eigenvalue/eigenvector decomposition allows separation of the matrix components into those that are

of interest for moving target detection, and those that are not. This eigen-decomposition naturally produces the ATI phase as a detection metric, and provides two others namely, λ_2 and the similarity phase.

Since, for every covariance matrix sample, the estimated ATI phase and the estimated similarity phase define a point on the unit sphere, one can combine the phases into a single phase by choosing the sphere axis to pass through the expected value of the coordinates of clutter. This combined phase, called the unitary phase, incorporates the moving-target information previously contained in the separate metrics.

Based upon the assumption of two zero-mean Gaussian channels, the sample covariance matrix has a complex Wishart distribution. Decomposition of the sample covariance matrix is accompanied by decomposition of the Wishart distribution into distributions of the matrix elements.

By noting that DPCA can be written as a combination of the decomposition elements it becomes clear that DPCA and the ATI phase, are not statistically independent. However, the ATI phase and the second eigenvalue show a great degree of statistical independence. Recombination of the the small eigenvalue and the unitary phase leads to the proposed adaptable hyperbolic detector.

CHAPTER 5

MULTIPLICATIVE TEXTURE RANDOM VARIABLE

In practice, one often encounters limitations in the model of a stationary zero-mean Gaussian process in each channel. Although the stationary Gaussian model is still locally suitable, the process is not stationary when the background reflectivity (variance) changes from multilooked sample to multilooked sample. While it is still valid to assume that the mean of the process is zero and stationary, the variance must be modelled as globally non-stationary. For instance, the variance of the SAR data may be quite different for grassy terrain compared to forested terrain. In a scene containing both types (and more) of terrain, a statistical description of the random variance must be included to validate the model.

To this end, the introduction of a random variable $A \in [0, \infty)$ such that $\hat{\boldsymbol{R}} \rightarrow A\hat{\boldsymbol{R}}$, leads to the so-called product model. Many authors have studied appropriate statistical models for A including [TBQ95, JWP94, Gie01a]. This thesis adopts the inverse chi-square model, χ^{-2}, of [Gie01a], with a generalization to arbitrary powers, $\chi^{-2\kappa}$. The probability density function for χ^{-2} is given by [Gie01a]

$$f_A(a) = \frac{\Theta^\nu e^{-\Theta/a}}{\Gamma(\nu) a^{\nu+1}}, \quad a \in [0, \infty). \tag{5.1}$$

It also has a cumulative distribution function given by

$$F_A(a) = \frac{1}{\Gamma(\nu)} \Gamma(\nu, \Theta/a). \tag{5.2}$$

which can readily be computed from the characteristic function for the gamma function presented in [Spi94]. Although the distribution has two parameters, imposing the constraint that $\mathcal{E}\{A\} = 1$ leaves only a single describing parameter.

In our proposed generalization of the above random variable, we make the transformation $A \rightarrow W = A^\kappa$ where $\kappa > 0$. The Jacobian introduced by this transformation is $\mathrm{d}w = \kappa a^{\kappa-1} \mathrm{d}a$ thus leading to a probability distribution for W given by

$$f_W(w) = \frac{\theta^\nu e^{-\frac{\theta}{w^{1/\kappa}}}}{\kappa \Gamma(\nu) w^{\nu/\kappa+1}} \tag{5.3}$$

Figure 4.10 showed deviation of the theoretical eigenvalue probability distribution from the histogram of measured data. The theoretical distribution predicts a higher number of lower valued samples than actually measured. The purpose of the random variable, W, is thus to elongate the theoretical probability distribution.

Introduction of a product model complicates evaluation of closed form solutions to the theoretical probability distributions. While good approximations of distributions have been presented in the literature, [Gie01a], general closed form solutions are more elusive, especially when the functions describing the homogenous random variable are already complicated. This thesis therefore presents a method to numerically compute the distribution functions.

5.1 Numerical methods for the product model

The model for power dependent metrics such as DPCA, the small eigenvalue, the eigenvalue projection metric or the hyperbolic detector, assumes statistical independence in the texture statistic. Designating the power dependent random variable as Y, we seek the probability distribution for the quantity

$$Z = WY. \tag{5.4}$$

Since $W > 0$ and $Y > 0$,

$$F_Z(z) = \mathcal{E}_X\{F_W(z/x)\}, \tag{5.5}$$

which leads to

$$f_Z(z) = \mathcal{E}_X\{f_W(z/x)\frac{1}{x}\}. \tag{5.6}$$

Computation of the threshold, δ_z, for a CFAR detector with false alarm rate P_F, requires solving $1 - F_Z(\delta_z) = \mathrm{P}_F$.

We now focus on the chosen probability distribution for W, namely,

$$\begin{aligned} F_W(w) &= F_A(w^{1/\kappa}) \\ &= \frac{1}{\Gamma(\nu)}\Gamma(\nu, \Theta/(w^{1/\kappa})). \end{aligned} \tag{5.7}$$

Using (5.6), one finds that

$$F_Z(z) = \int_0^\infty \frac{\Gamma(\nu, \Theta(x/z)^{1/\kappa})}{\Gamma(\nu)} \mathrm{d}F_X(x), \tag{5.8}$$

and evaluation of the CFAR threshold requires solving

$$\mathrm{P}_F = 1 - \int_0^\infty \frac{\Gamma(\nu, \Theta(x/\delta_z)^{1/\kappa})}{\Gamma(\nu)} \mathrm{d}F_X(x) \tag{5.9}$$

for δ_z. Section 6.2 shows that

$$\mathcal{E}\{W\} \equiv 1 \Rightarrow \Theta \equiv \left(\frac{\Gamma(\nu)}{\Gamma(\nu-\kappa)}\right)^{1/\kappa}, \tag{5.10}$$

therefore, a further simplification of (5.9) leads to

$$\mathrm{P}_F = 1 - \int_0^\infty \frac{\Gamma\left(\nu, \left[\frac{x\Gamma(\nu)}{\delta_z \Gamma(\nu-\kappa)}\right]^{1/\kappa}\right)}{\Gamma(\nu)} \mathrm{d}F_X(x) \tag{5.11}$$

To solve (5.11) one requires an estimate of ν and κ. Estimation of these parameters is discussed in section 6.2. Once these parameters have been determined, numerical integration can be conducted on (5.11) using the distribution for X where appropriate. For example, if X corresponds to λ_2, we substitute (4.33) into (5.11) and solve for δ_z.

5.2 Example of texturised λ_2 in mostly homogeneous terrain

Measured data are hardly (if ever) perfectly homogeneous. In what will be referred to as mostly homogeneous terrain (or just homogeneous terrain, or mildly heterogeneous terrain) we see a good fit with the theoretical distribution function when $\kappa = 0.5$. Figure 5.2 shows how the theoretical distribution and the measured data of figure 5.1 match well. It was found that $\hat{\nu} = 1.6014$ using the technique for estimation outlined in section 6.2.

5.3 Example of texturised λ_2 in heterogeneous terrain

Measured heterogeneous data also seem to fit with the theoretical distribution function, but for $\kappa = 0.2$. Figure 5.4 shows how well the theoretical distribution and the measured data of figure 5.3 agree. It was found that $\hat{\nu} = 0.4054$ using the technique for estimation outlined in section 6.2. Again, in this case, the nominal number of looks was required for the n parameter. By looking at the second moment of the texture statistic, we can compare the width of the distributions for

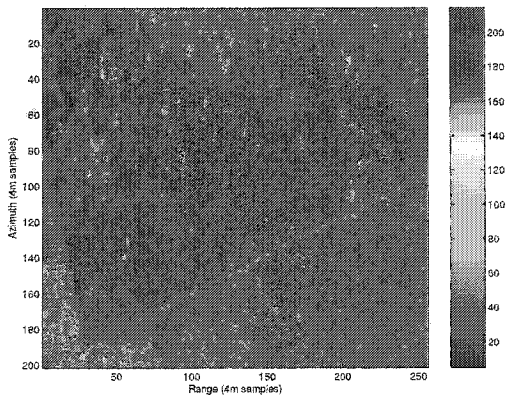

Figure 5.1. SAR scene of mildly heterogeneous terrain.

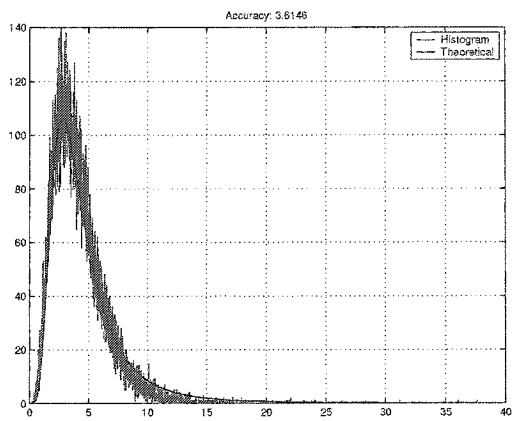

Figure 5.2. Theoretical distribution and histogram of the second eigenvalue for mildly heterogeneous terrain.

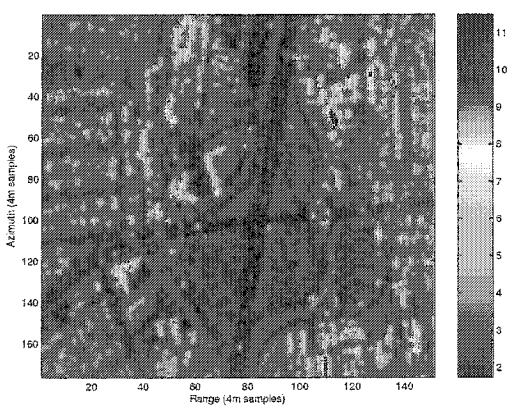

Figure 5.3. SAR scene of extremely heterogeneous terrain.

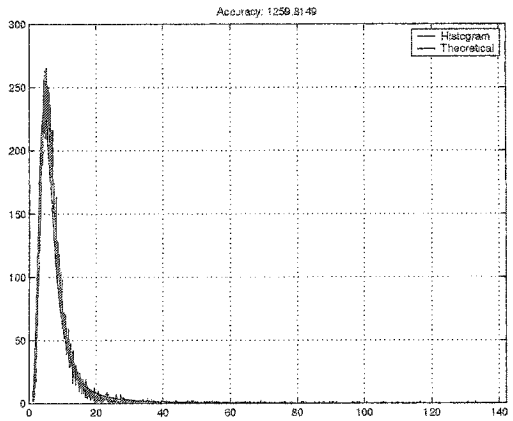

Figure 5.4. Theoretical distribution and histogram of the second eigenvalue for extremely heterogeneous terrain.

heterogeneous and extremely heterogeneous examples given above. The expression for the expected value of the second moment of the texture statistic follows from (6.12) and can be written as

$$\mathcal{E}\{W^2\} = \frac{\Gamma(\nu)\Gamma(\nu - 2\kappa)}{\Gamma(\nu - \kappa)^2}. \tag{5.12}$$

Substituting the estimated values for ν and κ found for the mostly homogeneous and extremely heterogeneous terrains yields 1.4690 and 20.2764, respectively. Thus, the texture distribution for the extremely heterogeneous terrain has greater variance.

5.4 Summary

This section introduced a multiplicative texture random variable. Both cases of extreme and mild heterogeneity seem to be well modelled by this new random variable. The statistics of the variable are based upon an inverse chi-square random variable raised to the power κ. Imposing the constraint that the expected value of the random variable equals one leads to a probability distribution function described by two parameters, κ and ν in addition to the number of looks, n. The method of moments can be used to estimate these parameters by generating two equations in two unknowns. The quality of the estimators regarding bias, efficiency and comparison with the Crámer-Rao bound is suggested for future research. Because the parameters can be estimated automatically, the texture statistic fits will into the scheme of an automatic CFAR detector.

CHAPTER 6

ESTIMATION OF COVARIANCE MATRIX PARAMETERS

Determination of CFAR thresholds for automatic target detection requires the estimation of the SAR scene parameters. In particular, to determine thresholds for the 2×2 case, the underlying covariance matrix needs to be estimated. In addition, the number of samples that are averaged, n, must be estimated.

6.1 Method of moments

Even with the computational load reduced, the iterative ML-estimator of [Gie01b] still has the problems of an undetermined convergence zone and numerical instability (the hypergeometric function has to be computed at values close to the unit circle). Hence, a robust and computationally efficient estimator for the equivalent number of looks is desirable, especially when the operational requirements pertain to larger scenes with many pixels. The approach presented here is based on the higher moments of the multilook ATI phase probability density function of (2.17). Due to the high degree of nonlinearity in (2.17), direct calculation of higher moments is extremely difficult if not impossible.

But, as a very special case, the one-look variance of δ was shown by [TBQ95] (see also [BH98]) to be

$$\mathrm{Var}(\delta) = \pi^2/3 - \pi \arcsin(|\rho|) + \arcsin^2(|\rho|) - \mathrm{Li}_2(|\rho|^2)/2, \tag{6.1}$$

where $\mathrm{Li}_2(\cdot)$ denotes Euler's dilogarithm [GR00].

Consequently, a suitable transformation of the phase variable rather than the phase δ itself is proposed. That is, one transforms the random variable δ to the random variable $Z = \exp(j\delta)$ and calculates the moments of Z. The new result presented in this thesis is the α^{th} moment of Z calculated in appendix D as

$$I_\alpha(n,\rho) = \frac{\Gamma(n+\alpha/2)\Gamma(1+\alpha/2)}{\Gamma(1+\alpha)\Gamma(n)} \rho^\alpha (1-\rho^2)^n {}_2F_1(n+\alpha/2, 1+\alpha/2; 1+\alpha; \rho^2). \tag{6.2}$$

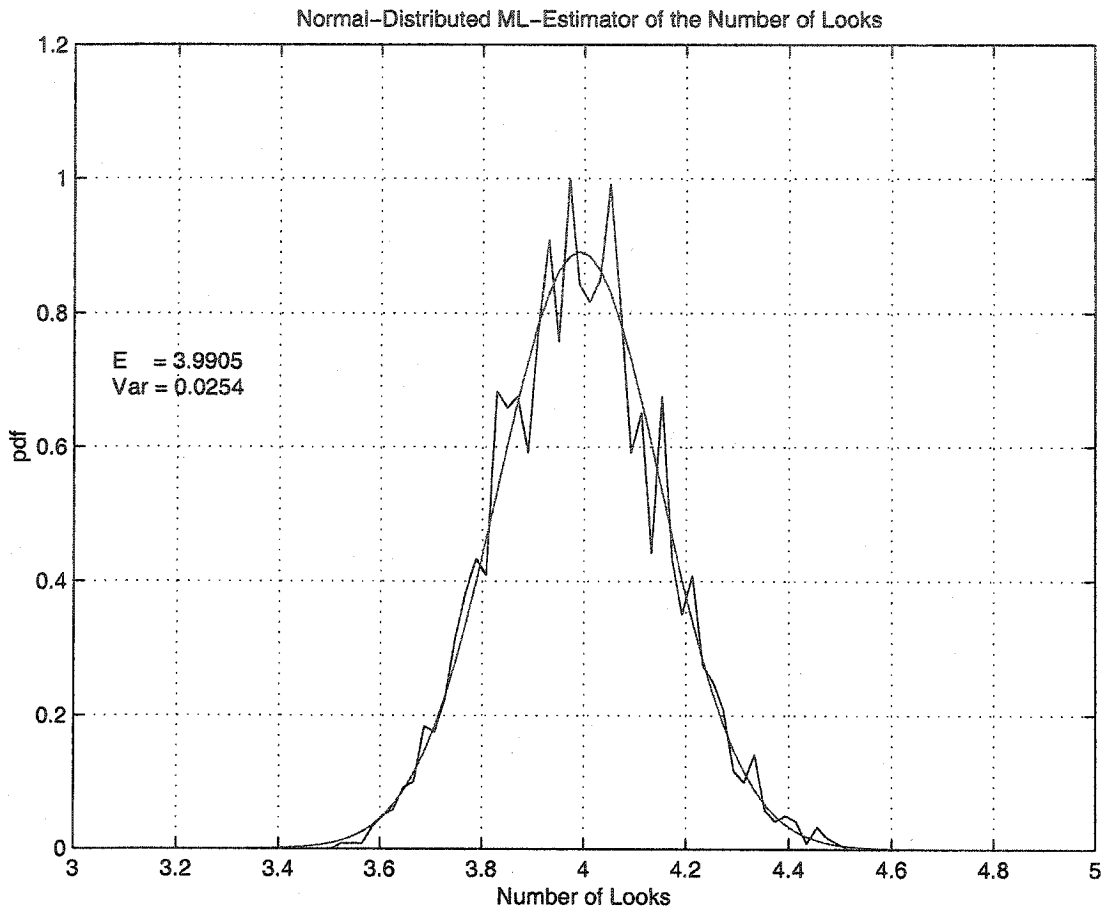

Figure 6.1. Histogram of the Maximum-Likelihood estimation of n for simulated phase data along with the normal distribution given by expectation, $\mu = 3.9905$ and variance, $\sigma^2 = 0.0254$.

From a computational point of view, this transformation is advantageous because the desired moment, α, can be efficiently estimated by simply normalizing each complex pixel in the SAR interferogram (transformation to the Z domain) and taking the real part of the average of Z^α.

Further, explicit computation of the hypergeometric function in (6.2) can be avoided for some special cases of α by rewriting the hypergeometric function as a polynomial in ρ^2, thereby increasing the numerical stability. It can be shown that the even moments all have closed form, albeit rather large and cumbersome for increasing α. It is interesting to note that $I_{2\alpha}(\alpha+1,\rho) = \rho^{2\alpha}$ for $\alpha = 1, 2, 3, \ldots$ Finding the roots of

$$\begin{aligned} I_2(n,\rho) - \bar{I}_2 &= 0, \\ I_4(n,\rho) - \bar{I}_4 &= 0, \end{aligned} \tag{6.3}$$

where the polynomials I_2 and I_4 are given in (D.21) and (D.20) of appendix D, and where $\bar{I}_\alpha$ denotes the α^{th} sample moment estimate

$$\bar{I}_\alpha = 1/N \sum_{m=0}^{N-1} z_m^\alpha, \tag{6.4}$$

principally allows one to simultaneously evaluate $\hat{\rho}$ and $\hat{n}$. Since the coherence can change significantly across a given SAR scene (whereas the number of looks remains the same) it seems advantageous to combine two separate estimators. By inserting the sample coherence estimate for ρ into (6.3) and finding the root for n leads to the desired estimate of n. Moreover, it is also possible to combine, (*e.g.* average), look estimates corresponding to different moments.

Applying the method of moments (MoM), [Spi94], to the same simulated data as used for the MLE in figure 6.1, results also in normal distributed n-estimates with expectation, $\mu = 4.0067$ and variance, $\sigma^2 = 0.0299$. Since the two distributions for the MLE and the MoM are almost identical, only one curve is shown along with the histogram in figure 6.1.

6.2 Method for estimating texture variable parameters

This section outlines a method for estimating the texture variable parameters necessary for implementation of an automatic CFAR scheme. The following assumption sets up the solution: the complex random variable measured by each antenna of the radar is the product of a sum of zero-mean complex Gaussian variables, each with variance σ^2, and a χ^{-2} random variable raised to the power κ.

Consider

$$x = a^\kappa \sum_{m=0}^{n-1} y(m), \tag{6.5}$$

where $y(m) = |z(m)|^2$ is the squared envelope of the circular complex Gaussian random variable, x_i, and a is χ^{-2}. Let us compute $\mathcal{E}\{x^\alpha\}$. Since a and $y(m)$ are assumed to be statistically independent,

$$\mathcal{E}\{x^\alpha\} = \mathcal{E}\{a^{\kappa\alpha}\}\mathcal{E}\left\{\left(\sum_{m=0}^{n-1} y(m)\right)^\alpha\right\}. \tag{6.6}$$

With each $y(m)$ independently identically Gamma distributed,

$$f_{Y(M)}(y(m)) = \frac{e^{-y(m)/\sigma^2}}{\sigma^2}, \tag{6.7}$$

the sum, denoted by $v = \sum_{m=0}^{n-1} y(m)$, has probability distribution [Spi94] given by

$$f_V(v) = \frac{v^{n-1}e^{-v/\sigma^2}}{\Gamma(n)(\sigma^2)^n}. \tag{6.8}$$

The expected value of v^α computes as

$$\begin{aligned}\mathcal{E}\{v^\alpha\} &= \int_0^\infty v^\alpha \frac{v^{n-1}e^{-v/\sigma^2}}{\Gamma(n)(\sigma^2)^n}\mathrm{d}v \\ &= \frac{(\sigma^2)^\alpha}{\Gamma(n)}\int_0^\infty \left(\frac{v}{\sigma^2}\right)^{n+\alpha-1} e^{-v/\sigma^2}\mathrm{d}\frac{v}{\sigma^2} \\ &= \frac{\Gamma(\alpha+n)(\sigma^2)^\alpha}{\Gamma(n)}.\end{aligned} \tag{6.9}$$

The χ^{-2} distribution for the texture variable is given by [Gie01a]

$$f_A(a) = \frac{\Theta^\nu e^{-\Theta/a}}{\Gamma(\nu)a^{\nu+1}}. \tag{6.10}$$

Computation of the moments of this variable proceeds as

$$\begin{aligned}\mathcal{E}\{a^{\kappa\alpha}\} &= \int_0^\infty \frac{a^{\kappa\alpha}\Theta^\nu e^{-\Theta/a}}{\Gamma(\nu)a^{\nu+1}}\mathrm{d}a \\ &= \frac{\Theta^{\kappa\alpha}}{\Gamma(\nu)}\int_0^\infty x^{\nu-\kappa\alpha-1}\exp(-x)\mathrm{d}x \\ &= \frac{\Theta^{\kappa\alpha}\Gamma(\nu-\kappa\alpha)}{\Gamma(\nu)}\end{aligned} \tag{6.11}$$

The second line above made the substitution $x = \Theta/a$. Requiring that $\mathcal{E}\{a^\kappa\} = 1$ dictates that $\Gamma(\nu) = \Theta^\kappa\Gamma(\nu-\kappa)$, or $\Theta = [\Gamma(\nu)/\Gamma(\nu-\kappa)]^{1/\kappa}$. Substituting (6.9) and (6.11) into (6.6) yields

$$\mathcal{E}\{x^\alpha\} = \frac{\sigma^{2\alpha}\Gamma(n+\alpha)}{\Gamma(n)}\left[\frac{\Gamma(\nu)}{\Gamma(\nu-\kappa)}\right]^\alpha \frac{\Gamma(\nu-\kappa\alpha)}{\Gamma(\nu)}. \tag{6.12}$$

For moderately heterogeneous terrain, the appropriate choice for κ, empirically, seems to be $\kappa = 0.5$. Instances of $\kappa = 1$ have been observed for grassy terrain mixed with metal debris, a few trees and a few roads [Gie04]. For urban terrain, as shown in the previous chapter, one finds that $\kappa < 0.5$ fits better, especially for extreme values of the random variable. Solving for ν involves estimating the first and second moments from the data then using (6.12) with $\alpha = 1$ and $\alpha = 2$ to create two equations with two unknowns, namely, σ^2 and ν. Theoretically, if the model were perfect, (6.12) could also generate three equations with three unknowns thereby allowing the value of κ also to be automatically estimated from the data. The estimates of ν and κ could then be indexed into a map of possible classifications of terrain types to provide contextual information about the terrain being examined.

In the case of $\kappa = 1$, solving (6.12) leads to the following expression for ν

$$\hat{\nu} = \frac{2(\hat{I}_2 - \hat{I}_1^2)}{\hat{I}_2 - 2\hat{I}_1^2}, \tag{6.13}$$

where the estimated moments are given by $\hat{I}_1$ and $\hat{I}_2$. Depending on the terrain type, the general equation (6.12), or the specific equation (6.13) can be used to automatically estimate the parameters of the texture random variable. Either can be computed from a single channel of data. Once the texture statistic parameters are known, thresholds for GMTI metrics that depend on the power of the reflected radiation can be computed.

6.3 Summary

This chapter demonstrated the need for a local estimate of the effective number of looks and the complex cross-correlation coefficient between the SAR channels. It presented a fast and robust estimator for these quantities. Comparisons with the optimum MLE showed that the MoM has, statistically, almost identical performance characteristics whereas the computation time for real SAR data was reduced from hours of computing time to quasi real-time. The MoM can be used for an operational CFAR system as it lends itself to rapid computation. Once the parameters ρ and n have been estimated, CFAR detection might be implemented by cross-referencing with a look up table of threshold values for different false alarm rates and for different combinations of ρ and n since direct computation appears daunting.

Additionally, because the algorithm does not require the individual channels for the estimation, indeed it can estimate the parameters from the multi-looked interferogram, data storage requirements are reduced.

The chapter also presented a method for estimating the texture parameters for the generalized inverse chi-square model, $\chi^{-2\kappa}$. The parameter estimation algorithm in this case does not rely on the joint channel data. It is also computed on the multi-looked data thereby allowing for relaxation of data storage requirements.

CHAPTER 7

APPLICATION TO TWO-CHANNEL SAR-GMTI

Given the marginal and joint probability distributions of the detection metrics, a CFAR detector can be created by calculating the threshold corresponding to some function of the metrics. For instance, a linear combination of the metrics could be computed as illustrated in figure 7.1. The

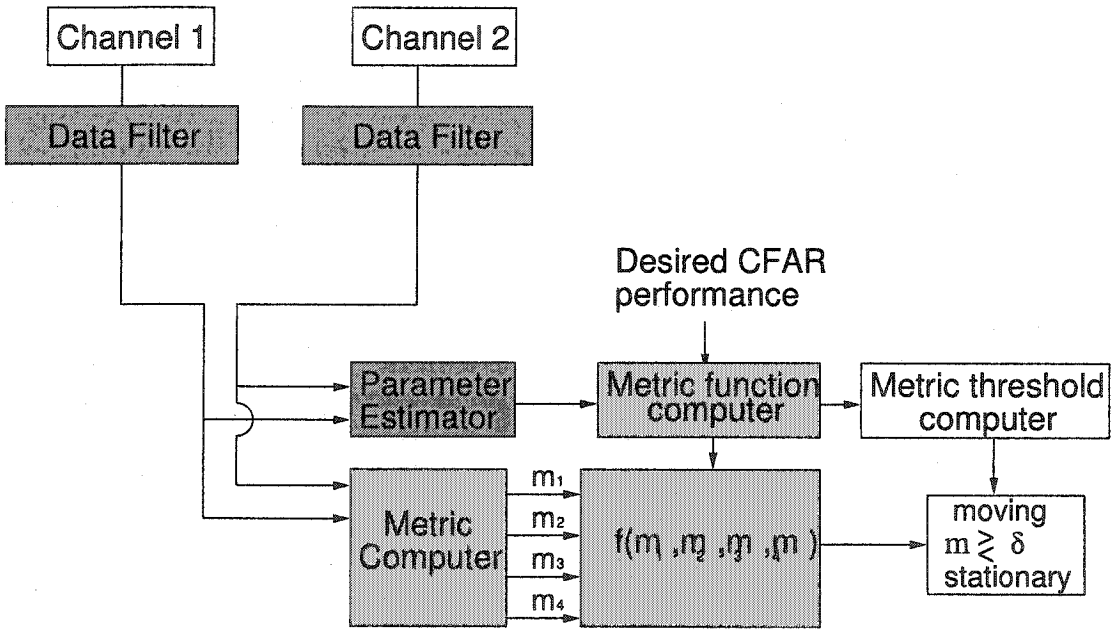

Figure 7.1. Linear combination of detection metrics.

greatest challenge when using this approach is to calculate the probability distribution of the sum of random variables, each one mathematically complicated in its own right. Once the probability distribution is known, the threshold can be dynamically computed or indexed from a look-up table. In this thesis, the recombination elements, functions of the decomposition elements, are examples of such functions of the decomposition metrics.

The function of the metrics need not be linear. Again, in these cases, the probability distribution of the dependent variable must be computed in order to implement the CFAR algorithm.

Two experiments demonstrate the application of the decomposition metrics and the recombination metrics to GMTI. First, by using simulated clutter and target data, we estimate the probability of moving target detection from a large number of clutter plus target samples. Second, from measured SAR data we provide a real-life examples of the metrics detecting moving targets for a false alarm rate of $P_F = 10^{-5}$. In both cases we compare the new metrics to the conventional metrics of DPCA and ATI.

Simulations are conducted for two types of clutter, homogeneous and heterogeneous, and for two types of target, deterministic and Gaussian with different target phases. First, thresholds for each metric are computed for a false alarm rate of $P_F = 10^{-4}$ for both mostly homogeneous ($\nu = 1.6014$, $\kappa = 0.5$) and heterogeneous ($\nu = 0.4054$, $\kappa = 0.2$) terrain. Complex clutter data for these terrain types are then simulated. Finally, moving targets are simulated and added to the clutter.

The moving targets are simulated for various target phases, $\{\pi/4, \pi/2, 3\pi/4, \pi\}$ which, given the radar system characteristics, correspond to across-track target velocities. To ensure that the statistics are well approximated, 10^7 samples are generated for each phase. The probability of target detection is estimated by counting the number of clutter plus target samples that pass the computed threshold for each metric.

Additionally, two types of moving target are simulated. First, deterministic targets have a signal vector given by

$$\vec{s} = \sigma_s \begin{bmatrix} 1 \\ e^{j\phi} \end{bmatrix}, \tag{7.1}$$

where σ_s^2 is the target power and $\phi \in [-\pi, \pi)$ is the target phase.

Secondly, the random Gaussian targets are simulated by applying the Swerling II case model which makes the assumption that the signal is a Gaussian random vector. The physics behind this assumption are comprehensively described in [Gie02]. Gaussian targets have zero-vector mean and covariance matrix

$$\mathcal{E}\{\vec{s}\vec{s}^{\dagger}\} = \boldsymbol{R}_s = \begin{bmatrix} \sigma_s^2 & \sigma_s^2 \rho e^{j\phi} \\ \sigma_s^2 \rho e^{j\phi} & \sigma_s^2 \end{bmatrix}, \tag{7.2}$$

where ρ is selected to be the same as for clutter, σ_s^2 is the target power, and $\phi \in [-\pi, \pi)$ is the target phase.

7.1 Conventional detectors and their weaknesses

Subtractive DPCA computes the difference between the complex responses of two channels but the norm of the difference is open to interpretation. In this section, to put the DPCA and the second

eigenvalue detection methods on the same footing, the norm is chosen as $|z_1 - z_2|^2$, where z_1 and z_2 are the displaced channel responses. In other words, since the second eigenvalue is in units of power, the DPCA norm should also be in units of power. The multilooked DPCA metric is given by

$$m_{DPCA} = \sum_{m=0}^{n-1} (z_1(m) - z_2(m))^\dagger (z_1(m) - z_2(m)), \tag{7.3}$$

or, after expansion and substitution using (4.23) as

$$m_{DPCA} = \Lambda_1 (1 - \sin(2\Theta)\cos\Delta) + \Lambda_2 (1 + \sin(2\Theta)\cos\Delta). \tag{7.4}$$

The second form shows how the metric depends on the eigenvalues.

The SCR curves for both the DPCA and ATI metrics are shown in figure 7.2 and figure 7.3, respectively. Figure 7.2 shows that DPCA has much poorer detection capability in heterogeneous terrain than in homogeneous terrain. Since Λ_1 represents, mostly, a sum of the channel powers, one expects an increase in the false alarm rate for a fixed threshold when the channel powers are high. Such instances occur, mainly, with heterogeneous terrain when high radar cross-section (RCS) buildings or metallic objects are present.

Comparison of the DPCA and ATI metrics reveals that, in homogeneous terrain, DPCA is the superior metric. However, the ATI metric shows a great degree of independence from the terrain type. For this reason, the ATI phase can, in some cases, more easily detect moving targets in heterogeneous terrain. The rate at which detectability increases with SCR is slower for ATI. In fact, one observes that to be more certain of target detection, by selecting a probability of detection of 0.9, the ATI detector requires a higher SCR than the DPCA detector, even in heterogeneous terrain.

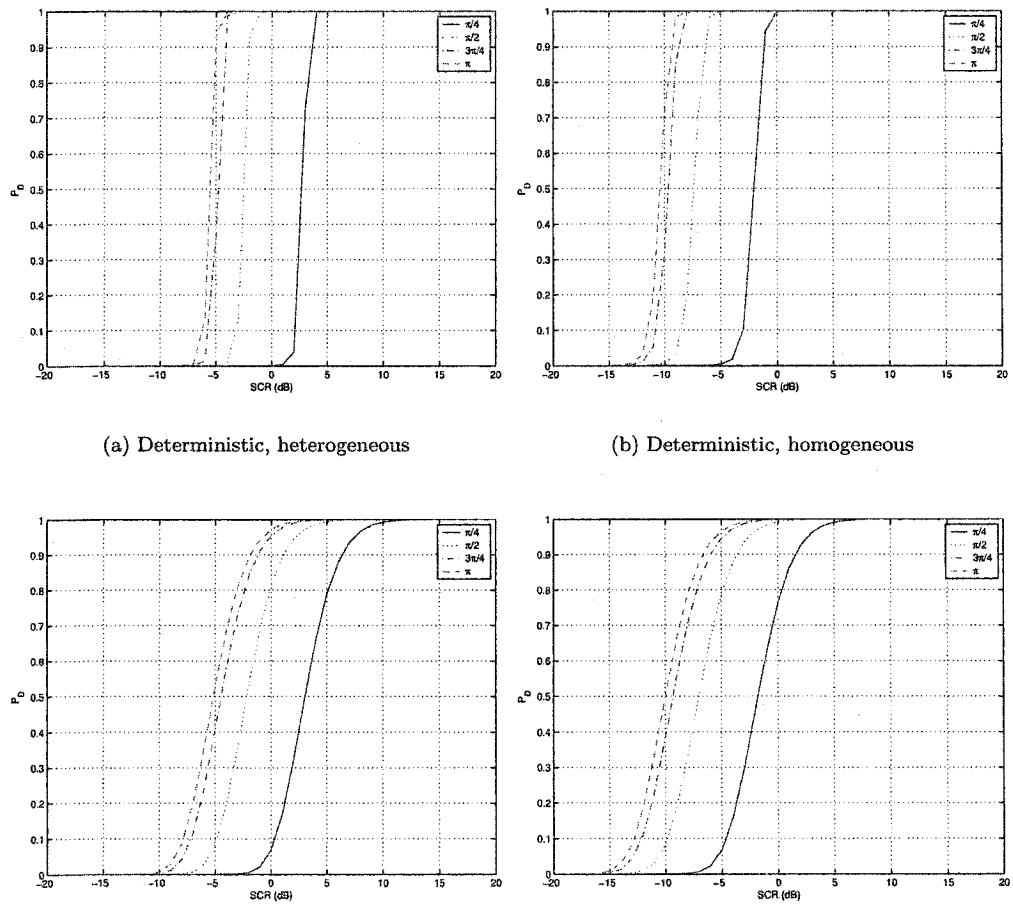

(a) Deterministic, heterogeneous

(b) Deterministic, homogeneous

(c) Gaussian, heterogeneous

(d) Gaussian, homogeneous

Figure 7.2. Probability of detection vs. SCR and target phase for the DPCA detector in heterogeneous and homogeneous terrains, for deterministic and random Gaussian target models.

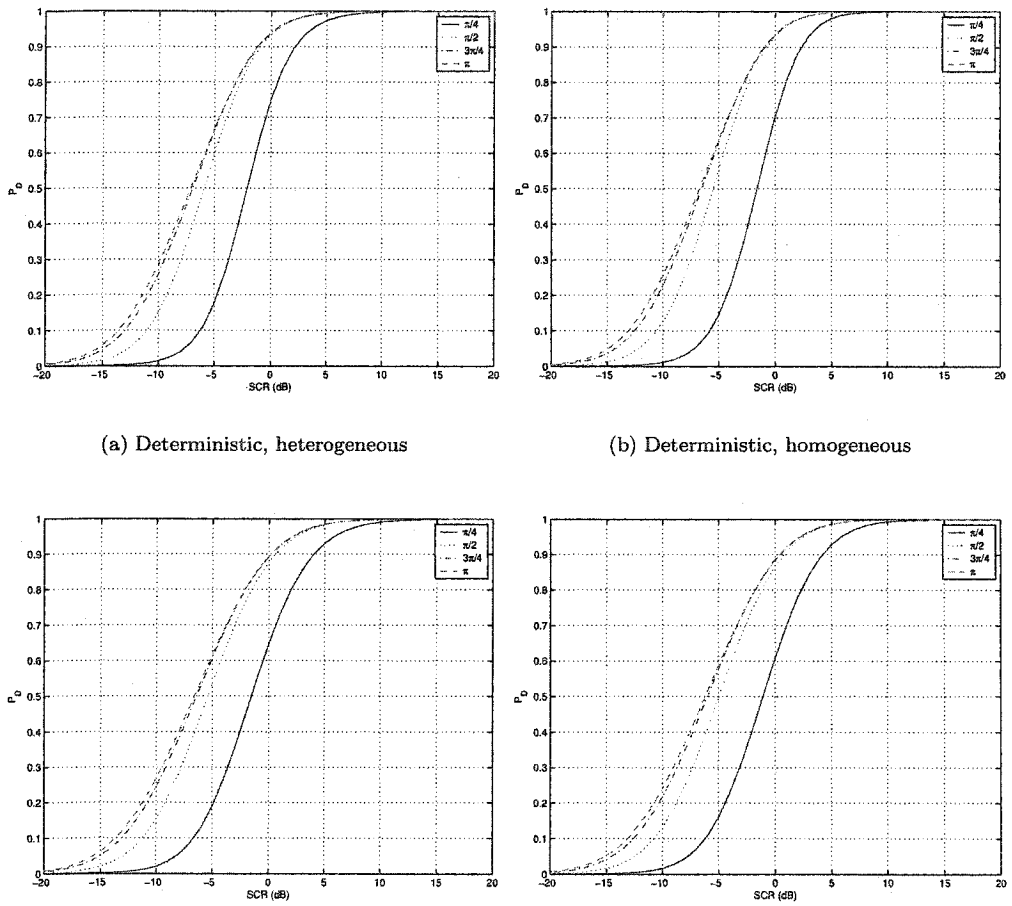

(a) Deterministic, heterogeneous

(b) Deterministic, homogeneous

(c) Gaussian, heterogeneous

(d) Gaussian, homogeneous

Figure 7.3. Probability of detection vs. SCR and target phase for the ATI detector in heterogeneous and homogeneous terrains, for deterministic and random Gaussian target models.

7.2 Detection with similarity and smallest eigenvalue

Figure 7.4 shows that the smallest eigenvalue does not perform as well as DPCA under any of the conditions considered. However, for random Gaussian targets in homogeneous terrain, the detection capability is only a couple of dB worse that DPCA. The detector does outperform the ATI detector in homogeneous clutter.

An explanation for why the detection capability tapers off for the deterministic target type is provided by looking at the limit of the smallest eigenvalue as SCR $\rightarrow \infty$ in the clutter plus target model. Since the target is deterministic, the outer product of $\vec{s}$ with itself has a structure similar to $\boldsymbol{R}$, but is singular, *i.e.*, $\lambda_2 \equiv 0$. Thus, by increasing the SCR, we decompose more and more of this matrix which converges to a finite value for λ_2. Figure 7.5 shows that the similarity compares poorly with the other detectors for GMTI capability. Its performance for GMTI is tempered by the fact that it has been shown to respond to water surfaces quite well [SGC03]. As such, it may provide a good metric for shoreline detection applications.

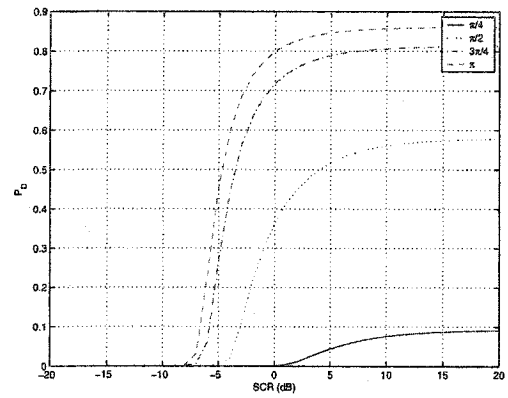

(a) Deterministic, heterogeneous

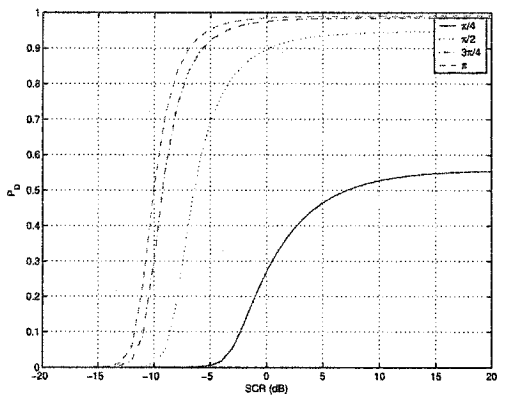

(b) Deterministic, homogeneous

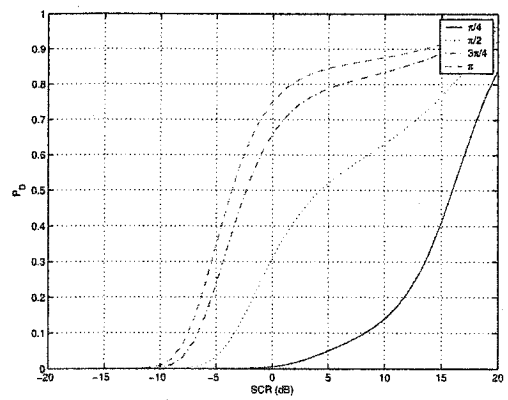

(c) Gaussian, heterogeneous

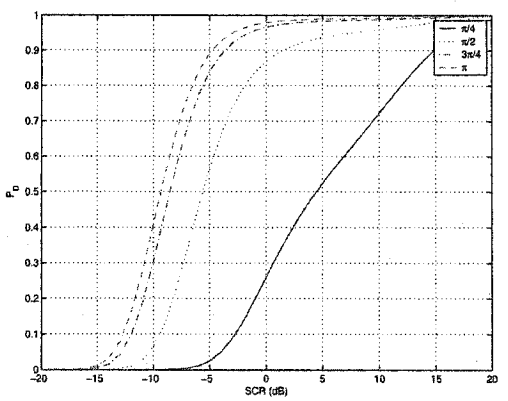

(d) Gaussian, homogeneous

Figure 7.4. Probability of detection vs. SCR and target phase for the smallest eigenvalue detector in heterogeneous and homogeneous clutter, for deterministic and random Gaussian target models.

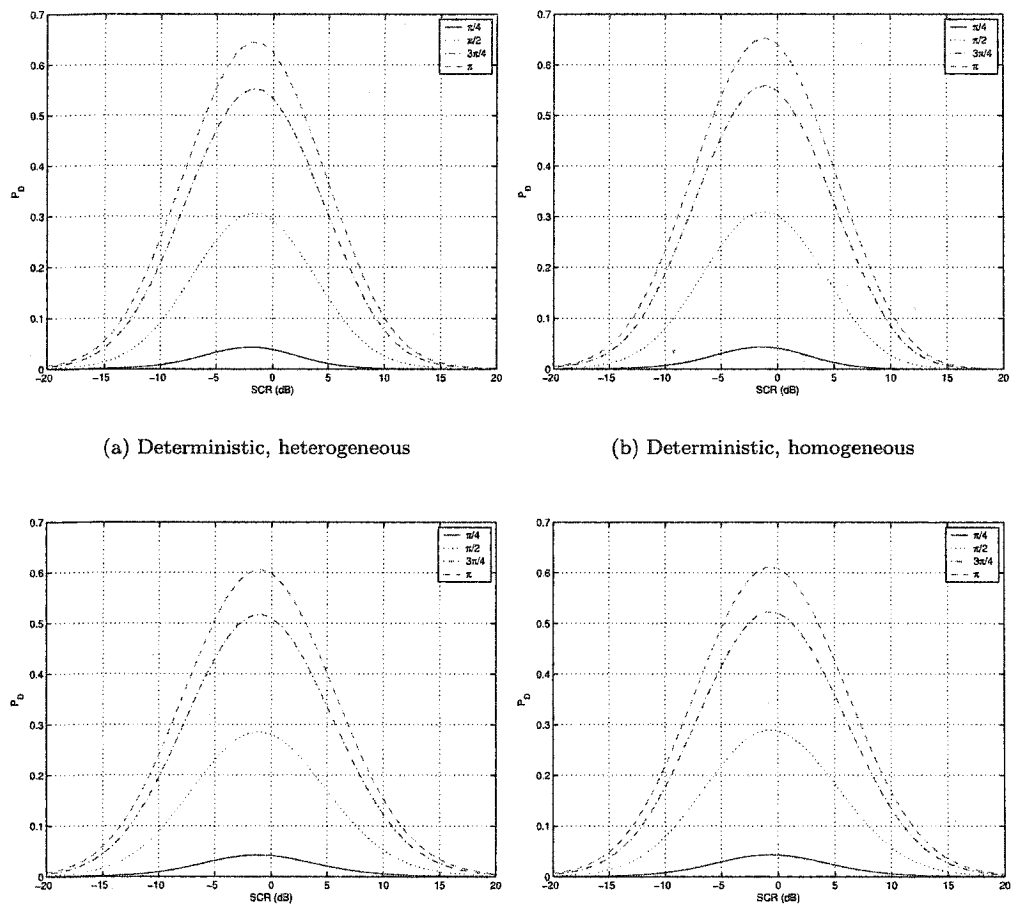

(a) Deterministic, heterogeneous

(b) Deterministic, homogeneous

(c) Gaussian, heterogeneous

(d) Gaussian, homogeneous

Figure 7.5. Probability of detection vs. SCR and target phase for the similarity detector in heterogeneous and homogeneous terrains, for deterministic and random Gaussian target models.

7.3 Detection with unitary phase

Figure 7.6 shows that the unitary phase performs with the same capability as ATI for a phase of $\pi/2$ radians. The ATI phase more often detects targets with a phase in $[-\pi/2, \pi/2)$ while the unitary phase more often detects targets when the phase is otherwise. This increased capability in the unitary phase over $[\pi/2, 3\pi/2)$ is especially noticeable for low SCR targets where equivalent detectability with the ATI phase would require a couple of more dBs of SCR. Whether the target is deterministic or random Gaussian and whether the clutter is heterogeneous or homogeneous seems not to change this observation.

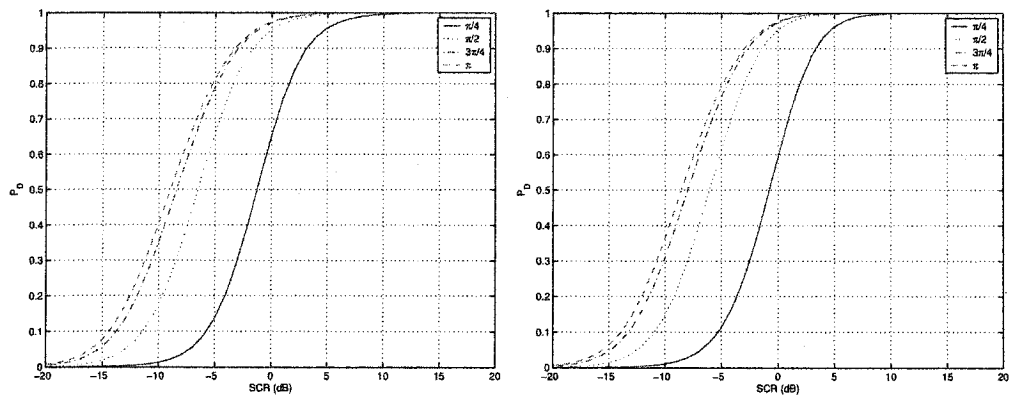

(a) Deterministic, heterogeneous

(b) Deterministic, homogeneous

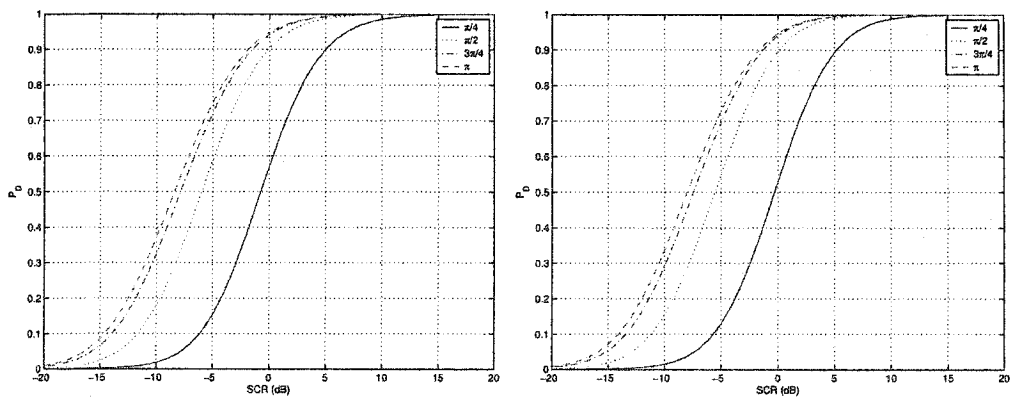

(c) Gaussian, heterogeneous

(d) Gaussian, homogeneous

Figure 7.6. Probability of detection vs. SCR and target phase for the unitary phase detector in heterogeneous and homogeneous terrains, for the deterministic and random Gaussian target models.

7.4 Detection with hyperbolic detector

Figure 7.7 illustrates the performance of the hyperbolic detector in both homogeneous and heterogeneous terrain. Comparison with figure 7.2 and figure 7.3, the DPCA and ATI detectors, reveals increased capability for the hyperbolic detector in heterogeneous terrain for all target phases.

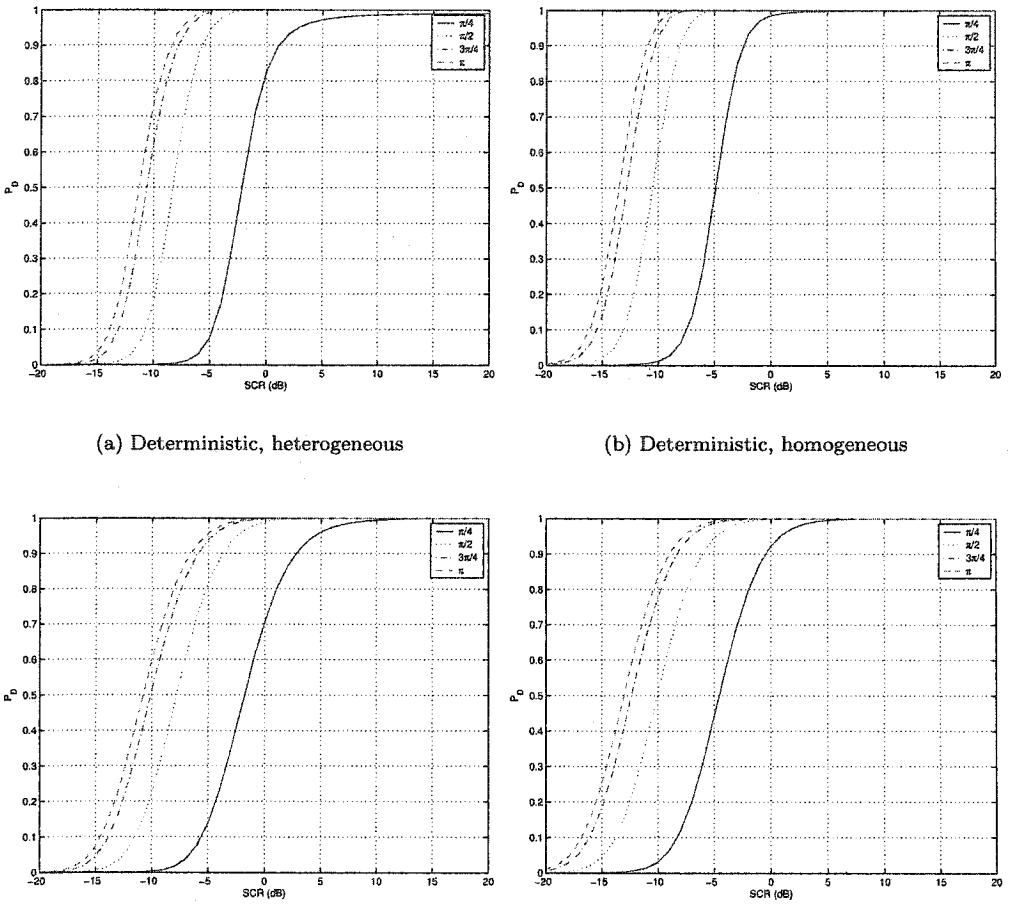

(a) Deterministic, heterogeneous

(b) Deterministic, homogeneous

(c) Gaussian, heterogeneous

(d) Gaussian, homogeneous

Figure 7.7. Probability of detection vs. SCR and target phase for hyperbolic detector in homogeneous and heterogeneous terrains, for deterministic and random Gaussian target models.

7.5 Detection with the eigen-projection metric

Detection with the eigen-projection metric compares with detection with the hyperbolic metric. Examination of figure 7.8 reveals that the detector has almost the same capability in both heterogeneous and mostly homogeneous terrain. There seems only to be about a half dB degradation in performance when compared to the hyperbolic detector curves of figure 7.7. Since the hyperbolic detector outperforms DPCA and ATI by a fair margin, so does the eigen-projection metric.

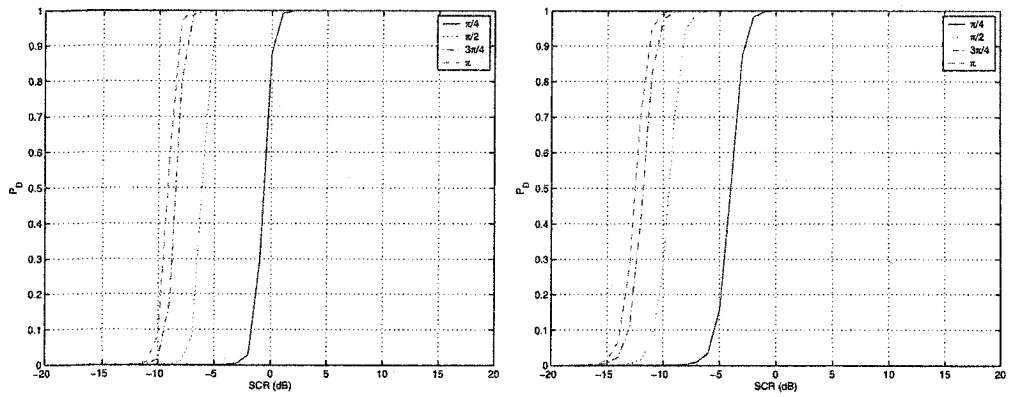

(a) Deterministic, heterogeneous

(b) Deterministic, homogeneous

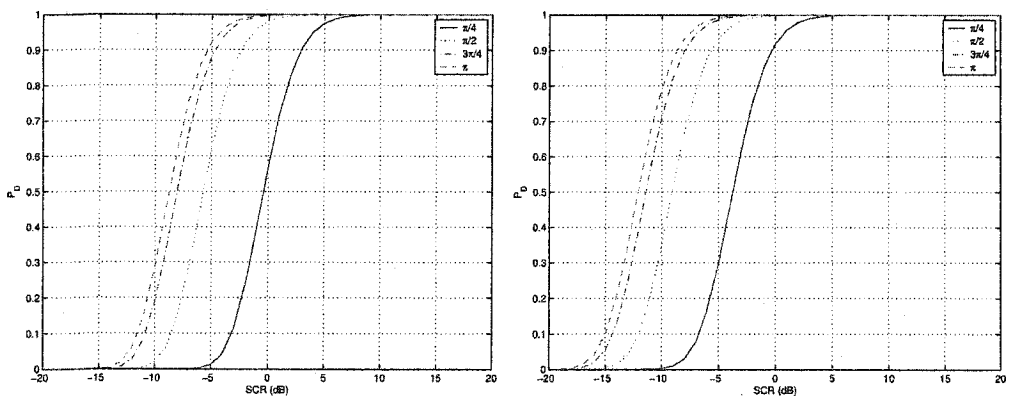

(c) Gaussian, heterogeneous

(d) Gaussian, homogeneous

Figure 7.8. Probability of detection vs. SCR and target phase for projection detector in homogeneous and heterogeneous terrains, for deterministic and random Gaussian target models.

7.6 Comparison of metrics

Table 7.1 compares the probability of detection of a discrete target by each metric, while table 7.2 compares the probability of detection of a Gaussian random target by each metric. This table format more readily permits comparison of the capabilities of the metrics relative to each other. The data reported in the tables are the same used to create the figures in sections 7.1 to 7.5.

Table 7.1. Comparison of probability of detection of a discrete target by each metric. Values in percent.

		Homogeneous					Heterogeneous				
Target		**SCR** (dB)					**SCR** (dB)				
type	**Metric**	-10	-5	0	5	10	-10	-5	0	5	10
Discrete, phase $\pi/4$ rad	m_{DPCA}	0	0	100	100	100	0	0	0	100	100
	m_h	1	47	99	100	100	0	8	83	97	99
	$m_\perp$	0	16	100	100	100	0	0	88	100	100
	δ	1	15	70	98	100	1	18	75	97	100
	ϑ	1	11	60	96	100	1	14	65	96	100
	θ	1	3	4	1	0	1	3	4	1	0
	λ_2	0	1	27	47	53	0	0	0	4	8
Discrete, phase $\pi/2$ rad	m_{DPCA}	1	100	100	100	100	0	0	100	100	100
	m_h	60	100	100	100	100	17	95	100	100	100
	$m_\perp$	28	100	100	100	100	0	97	100	100	100
	δ	13	55	93	100	100	15	60	93	99	100
	ϑ	15	62	95	100	100	18	66	95	100	100
	θ	8	24	30	16	3	9	25	29	14	3
	λ_2	1	69	90	93	94	0	0	36	52	56
Discrete, phase $3\pi/4$ rad	m_{DPCA}	32	100	100	100	100	0	37	100	100	100
	m_h	93	100	100	100	100	63	99	100	100	100
	$m_\perp$	98	100	100	100	100	2	100	100	100	100
	δ	23	63	94	100	100	26	67	94	99	100
	ϑ	31	77	97	100	100	35	79	97	100	100
	θ	19	46	55	33	8	21	47	53	30	8
	λ_2	30	92	98	98	98	0	27	72	79	81
Discrete, phase π rad	m_{DPCA}	71	100	100	100	100	0	94	100	100	100
	m_h	97	100	100	100	100	74	100	100	100	100
	$m_\perp$	99	100	100	100	100	8	100	100	100	100
	δ	26	64	93	100	100	29	67	94	99	100
	ϑ	37	80	98	100	100	41	82	97	100	100
	θ	23	54	64	40	11	26	56	62	37	10
	λ_2	51	95	98	99	99	0	46	80	85	86

Both tables 7.1 and 7.2 indicate the superior performance of the hyperbolic detector and the eigen-projection detector. First of all, for an SCR of -10 dB, both m_h and $m_\perp$ consistently show the greatest probability of detecting moving targets in homogeneous terrain. For a target in homogeneous terrain, m_h is the most likely metric to detect a target with a phase of $\pi/4$ radians and an SCR of -5 dB. In heterogeneous terrain, m_h and $m_\perp$ are the best candidates for detecting a discrete target

Table 7.2. Comparison of probability of detection of a Gaussian target by each metric. Values in percent

Target type	Metric	Homogeneous SCR (dB)					Heterogeneous SCR (dB)				
		-10	-5	0	5	10	-10	-5	0	5	10
Gaussian, phase $\pi/4$ rad	m_{DPCA}	0	7	76	99	100	0	0	7	79	99
	m_h	3	44	92	100	100	0	14	71	96	99
	$m_\perp$	0	30	92	100	100	0	1	57	97	100
	δ	2	16	61	93	99	2	19	65	93	99
	ϑ	1	13	53	89	99	2	15	57	90	99
	θ	1	3	4	2	1	1	3	4	2	1
	λ_2	0	2	26	52	72	0	0	0	1	4
Gaussian, phase $\pi/2$ rad	m_{DPCA}	9	79	99	100	100	0	9	81	99	100
	m_h	51	95	100	100	100	22	82	99	100	100
	$m_\perp$	35	93	100	100	100	2	62	98	100	100
	δ	13	50	87	99	100	15	54	88	98	100
	ϑ	15	55	90	99	100	18	59	90	99	100
	θ	8	22	29	18	6	9	23	28	17	5
	λ_2	6	57	87	94	96	0	0	10	27	38
Gaussian, phase $3\pi/4$ rad	m_{DPCA}	38	95	100	100	100	0	41	96	100	100
	m_h	78	99	100	100	100	52	94	100	100	100
	$m_\perp$	71	99	100	100	100	19	88	100	100	100
	δ	22	58	89	99	100	24	61	90	98	100
	ϑ	29	70	94	99	100	33	72	94	99	100
	θ	18	42	52	36	13	20	43	51	34	12
	λ_2	30	84	97	98	99	0	5	39	58	65
Gaussian, phase π rad	m_{DPCA}	50	97	100	100	100	1	53	97	100	100
	m_h	84	99	100	100	100	60	96	100	100	100
	$m_\perp$	79	99	100	100	100	29	92	100	100	100
	δ	24	59	88	99	100	27	62	89	98	100
	ϑ	34	73	95	100	100	37	75	95	99	100
	θ	22	49	61	43	17	24	51	60	40	15
	λ_2	41	89	98	99	99	0	11	50	66	72

with a phase of $\pi/4$ radians and an SCR of 0 dB. This also holds for a discrete target with a phase of $\pi/2$, $3\pi/4$ or π radians with an SCR of -5 dB. A Gaussian target with a phase of $\pi/2$, $3\pi/4$ or π is most readily detected by m_h and $m_\perp$ (more than 60% of the time with $m_\perp$, more than 80% of the time with m_h) when it has an SCR of -5 dB, no matter whether the target is in heterogeneous or homogeneous terrain. One sees that to be 82% likely to detect a phase $\pi/2$ rad Gaussian target in heterogeneous terrain, about -10 dB SCR is required for m_h, while -5 dB is required for DPCA.

7.7 Complexity considerations

Conventional DPCA in the 2-channel case requires fewer computer flops than computation of the smallest eigenvalue or the unitary phase. However, due to the fact that these quantities are computed

over the multi-looked scene, and due to recent improvements in computer processing capabilities, the required time for the eigenvalue/eigenvector decomposition does not exceed real-time constraints, and, furthermore, takes the same order of time as required for SAR compression itself. It therefore does not represent a rate-limiting step in the SAR-GMTI problem.

Table 7.3 breaks down the time required for SAR-GMTI computation on a SUN UltraAX-MP machine for an $n = 40$ sample. In table 7.3, the decomposition of all elements is reported in terms of flops. The number of flops is computed using Matlab's^{TM}flops command, and the time taken for computation is computed using the tic toc function. The flops command reports the number of floating point additions, subtractions, multiplications and divisions, but does not report the number of flops required to compute either the trigonometric functions or the square root function. Furthermore, to compute both the hyperbolic and the eigenprojection metrics, one needs to first estimate some scene parameters; therefore, the values reported in table 7.3 underestimate both the true number of required flops, and the true required time to compute these metrics. Formulas used to compute the metrics are (4.23), (B.54), (4.54) and (4.64), for the decomposition elements, the unitary phase, the hyperbolic metric and the eigenprojection metric respectively.

Table 7.3. Break-down of time required for SAR-GMTI metric computation per sample for $n = 40$

Metric	Flops	Time (s)
λ_2	900	4.1E-4
δ	321	3.4E-4
θ	888	4.0E-4
ϑ	895	4.9E-4
DPCA	440	3.1E-4
Hyperbolic	918	5.4E-4
Eigenprojection	883	4.0E-4

7.8 Example of detection with measured SAR data

Estimation procedures for SAR data parameters are outlined in [GS02, Gie01a]. Using these procedures, thresholds are computed for a false alarm rate of $P_F = 10^{-5}$. These thresholds are then applied to the computed metrics and target detections for each metric are marked with an "x".

The λ_2 metric is not presented here because it did not detect any moving targets. Thresholds for the eigenprojection metric have not yet been computed so it not shown either. However, one expects similar performace with the eigenprojection metric as obtained from the hyperbolic detection metric. The capability of the eigenprojection metric to detect moving targets in an urban scene will be more

thoroughly investigated in future work. Although the data presented in figures 7.8 to 7.8 contain

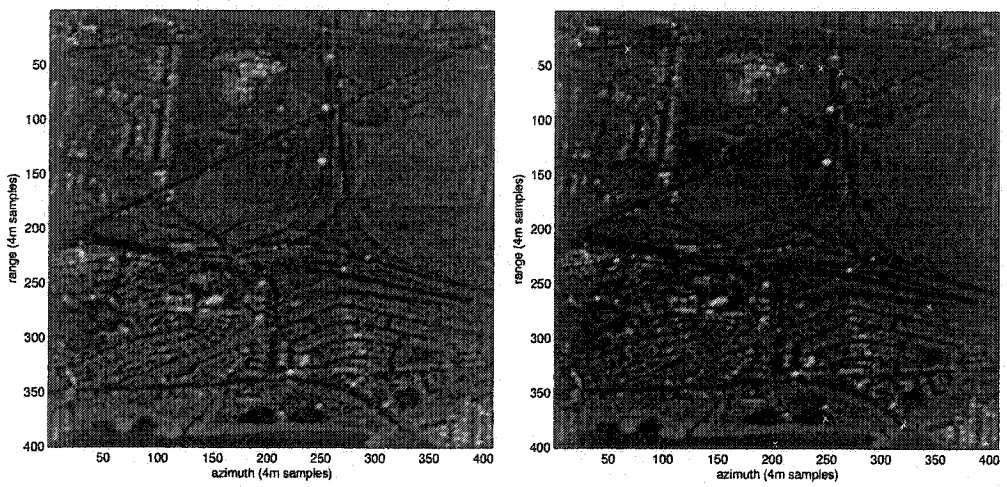

(a) SAR scene

(b) Detections with similarity

Figure 7.9. SAR scene of West Ottawa and detections "x" with similarity metric.

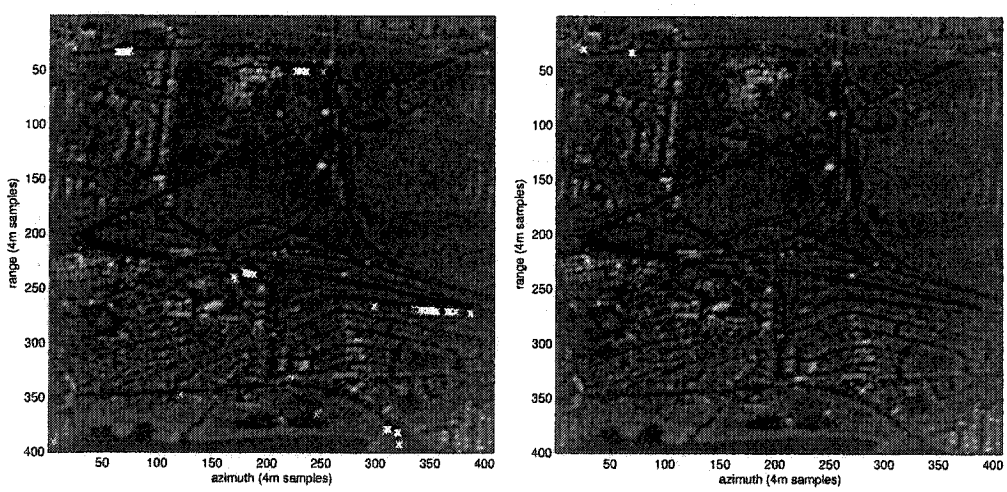

(a) Detections with hyperbolic metric

(b) Detections with DPCA

Figure 7.10. Detections "x" with hyperbolic metric and DPCA metric for real SAR data in West Ottawa.

moving targets, because they were collected over a busy city, no ground truth data are present to corroborate the moving target detections. This data therefore represents what one would get in a

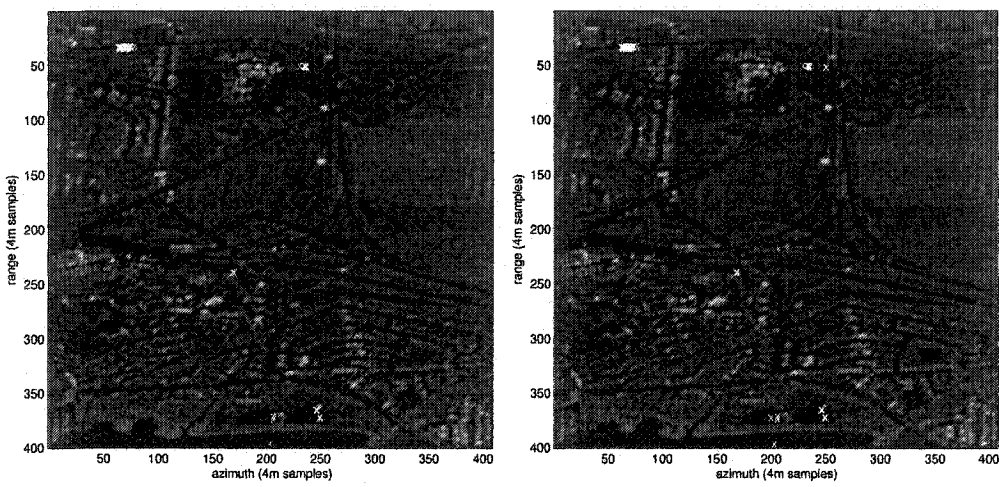

(a) Detections with ATI

(b) Detections with unitary phase metric

Figure 7.11. Detections "x" with ATI metric and unitary phase metric for real SAR data in West Ottawa.

real situation, where faith would have to be invested in the accuracy of the statistical models. One could argue that real moving targets should, generally, appear near roads. The hyperbolic detection image indicates targets close to a highway that horizontally spans the image. These targets are slightly displaced from the highway due to the azimuthal shift caused by their across-track motion.

The statistical argument says that given the specified false alarm rate of $P_F = 10^{-5}$, one expects, for a scene of $400 \times 400 = 160000$ samples, to obtain 1.6 false alarms per image. Thus, in figure 7.8, one expects, of the eight similarity detections marked with an 'x', that two will be false alarms. These false alarms are probably the detections at the bottom of the image, over the water. In figure 7.10, the hyperbolic detector indicates a large number of detections, perhaps 25-30 detections. We expect that only two of these are false alarms. The DPCA image shows only three detections in the upper left corner. One suspects that the leftmost detection is a false alarm, while the two rightmost detections, almost atop each other, have been picked up by the other detectors so could represent a real target. With the ATI and unitary phase detections illustrated in figure 7.8, one suspects that maybe a couple of detections in the lower portion of the image are false alarms while the other detections are real moving targets.

Given that the false alarm rate was set to the same value for all images, one sees clearly that the hyperbolic detector best detects the moving targets. The ATI phase and the unitary phase detect fewer targets, the similarity detector finds fewer still, and DPCA finds the least number of targets.

7.9 Summary

The marginal probability distributions of the elements are used to compute detection thresholds for a given false alarm rate. In combination with simulated clutter plus target data, these thresholds are used to estimate the probability of target detection versus target SCR.

The similarity phase measures the degree of similarity between the two channels, and behaves like the cross-correlation coefficient. Because moving targets change in appearance between channel acquisitions, the similarity can also detect moving targets. However, the estimated probability of detection versus SCR curve for the similarity metric indicates that it is far less sensitive than are DPCA, Λ_2 or the ATI phase.

The combined independent unitary phase metric better detects targets with phases in the range $[\pi/2, 3\pi/2)$ than does the ATI metric. It maintains the property of being insensitive to terrain heterogeneity.

In a two channel system measuring homogeneous terrain, the optimal detector based upon a linear filter of the channels, is the DPCA detector. The linear filter is designed to cancel the clutter leaving, in the residue, moving targets that have been suppressed to a lesser degree. The second eigenvalue has similar characteristics to DPCA in homogeneous terrain for Gaussian type targets, and represents the maximum possible non-trivial clutter cancellation between the two channels.

The hyperbolic and the eigen-projection detectors permit the detection of moving targets with a much greater tolerance for heterogeneity than DPCA. In fact, even in the mostly homogeneous case, these metrics perform significantly better than DPCA. The eigen-projection and hyperbolic metrics have practically identical detection capabilities with the eigen-projection metric only about half a dB less sensitive than the hyperbolic metric. However, the eigen-projection metric also provides potentially useful information about bright stationary targets. It is possible to develop the CFAR rules for the hyperbolic detector and the eigen-projection metrics as their probability distributions are known (see chapter 4).

CHAPTER 8
CONCLUSION

In this thesis, we present the theoretical background on SAR-GMTI techniques using two or more SAR channels. The processing of SAR data for GMTI, the joint channel statistics, the CFAR detection of moving targets, and the estimation of target velocity characteristics, such as along-track velocity and across-track velocity, are discussed.

8.1 Thesis summary

The discussion of stripmap SAR processing for moving targets mentions the azimuth displacement phenomenon that results from the Doppler frequency offset of targets possessing an across-track velocity component. Relocation of the moving target to its true location in a processed image can be achieved by estimating the target's across-track velocity and, either estimating the position by inverse computation of the physical model, or modification of the processing filter by compensating with the estimated target velocity. It is affirmed that, aside from a virtually negligible contribution from the along-track velocity, the displacement is a function of the across-track velocity. Analysis of the functional dependence also reveals that, if a given across-track velocity produces a certain displacement, then the same across-track velocity plus any integer multiple of a certain wrap-velocity, produces an equivalent displacement.

In addition to the displacement, attempting to SAR compress a moving target with an along-track velocity by using a processing filter designed for stationary targets, leads to a spread of the target energy into neighbouring image pixels and, therefore, a reduction of the target peak power. The quality of parameter estimation in these situations is reduced by the lower SCR.

By adaptive target processing, it is possible to estimate the target across-track velocity, for example, by building a processing filter that discriminates against targets without across-track velocities. However, this estimate of the across-track velocity is ambiguous in the same way that the displacement as a function of velocity is ambiguous. Coherent analysis, with two or more channels, provides an independent method for estimating the target across-track velocity. Unfortunately this measurement is also ambiguous though with a different wrap-velocity. By combining the two

ambiguous measurements, the overall wrap-velocity becomes the least common multiple of the two wrap-velocities, allowing unambiguous estimation of across-track velocity for targets that are a priori known to have maximum speeds well below the combined wrap-velocity.

The construction of matched filters for the processing of moving targets is based upon a model of the imaging geometry as it evolves through time. By considering that a target might be moving, the filters are seen to have a functional dependence on the target velocities and accelerations. Optimising the target response by determining the filter that produces the most sharply focused image of the target can be interpreted as maximum likelihood estimation of the target velocity and acceleration. Due to the geometry of strip-map SAR, it is impossible to decouple the across-track acceleration component from the along-track velocity component. Scanning through a range of target velocities and accelerations to find the best focused target requires processing power and time. Automatically focusing the target by measuring the displacement function allows a significant reduction in processing requirements.

If the radar PRF adequately over-samples the clutter bandwidth, fast moving targets are easily distinguished from clutter as their Doppler spectrum lies outside the clutter spectrum. The estimation of target velocities in these cases is not affected by clutter interference. Application of the SPECAN algorithm naturally incorporates this leverage and is additionally attractive in that it requires only a single FFT to compute. In comparison, full SAR compression using the Fourier Transform implementation of convolution requires two FFTs, generally meaning that the processing takes twice as long.

The covariance matrix of two or more SAR channels contains all of the information required to detect a moving target. Therefore, the analysis of the matrix by decomposition methods is proposed as an alternative to conventional detection methods including DPCA and ATI. The eigenvalue/eigenvector decomposition allows separation of the matrix components into those that are of interest for moving target detection, and those that are not. This eigendecomposition naturally produces the ATI phase as a detection metric, and provides two others namely, the second eigenvalue and the similarity phase.

In a two channel system measuring homogeneous terrain, the optimal detector based upon a linear filter of the channels, is the DPCA detector. The linear filter is designed to cancel the clutter leaving, in the residue, moving targets that have been suppressed to a lesser degree. The second eigenvalue has similar characteristics to DPCA, and represents the maximum amount of clutter cancellation between two channels. Because DPCA does not suppress the moving targets to the same degree as second eigenvalue, it is a superior metric over homogeneous terrain. However, in

heterogeneous terrain, DPCA is more likely than the second eigenvalue to misidentify spiky clutter as moving targets and, hence, increase the false alarm rate.

The similarity phase measures the degree of similarity between the two channels, and behaves like the cross-correlation coefficient. Because moving targets change in appearance between channel acquisitions, the similarity can also detect moving targets. It is also seen to be a powerful indicator of water or other scene elements that decorrelate between channel acquisitions. The receiver operating characteristics of the similarity phase for moving target detection show it to be far less sensitive than the second eigenvalue and the ATI phase. Since, for every covariance matrix sample, the estimated ATI phase and the estimated similarity phase define a point on the unit sphere, one can combine the phases into a single phase by choosing the sphere axis to pass through the expected value of the coordinates of clutter. This combined phase, called the unitary phase, incorporates the moving-target information previously contained in the separate metrics. It has better GMTI capability than the two individual metrics for target phases greater than $\pi/2$ radians.

Based upon the assumption of two zero-mean Gaussian channels, the sample covariance matrix has a complex Wishart distribution. Decomposition of the sample covariance matrix is accompanied by decomposition of the Wishart distribution into distributions of the matrix elements. The ROCs of each decomposition element can be constructed.

By noting that DPCA can be written as a combination of the decomposition elements it becomes clear that DPCA and the ATI phase, are not statistically independent. However, the ATI phase and the second eigenvalue are independent for the case of two looks, asymptotically independent for an increasing number of looks, and practically independent otherwise. This allows the construction of a joint detection metric, for example, the adaptable hyperbolic detector. The hyperbolic detector allows the detection of moving targets with a much greater tolerance for heterogeneity than DPCA. Additionally, it is possible to develop the CFAR rules for the hyperbolic detector.

Along the same lines of recombination of elementary decomposition metrics, this thesis also introduces an eigen-projection metric based upon viewing the sample covariance matrix as a point in a k-dimensional space[1] spanned by the outer-products of the eigenvectors of the true underlying covariance matrix. This new metric becomes the DPCA metric for special cases of the true covariance matrix, but generally has better GMTI capability than DPCA. In fact, the eigen-projection metric and the hyperbolic metric have almost the same capability, both requiring at least 3 dB less in signal to clutter ratio than DPCA to detect moving targets in even slightly inhomogeneous terrain. An

[1] k represents the number of antennas in the SAR system.

additionally advantage to the eigen-projection metric stems from the characteristic of identifying bright but stationary targets, information that may be of contextual use.

Decomposition of the Wishart distribution rapidly increases in mathematical complexity as the number of channels grows. The joint probability density function for a three channel system is presented, and the distribution of eigenvalues for the special case of covariance matrices with only two distinct eigenvalues is given. This special case corresponds to identical channel cross-correlation coefficients. The decomposed distribution functions allow the CFAR rules for the special case to be constructed.

The actual implementation of the CFAR rules requires estimation of the SAR data cross-correlation coefficient which is non constant. In addition to the correlation coefficient, the number of independent samples used to estimate the covariance matrix, also called the effective number of looks, has to be estimated. By using the proposed method of moments, these parameters can be simultaneously estimated from the SAR data, even when it has already been multi-looked. The method of moments is based upon the probability distribution of the ATI phase. Alternatively, the classical correlation coefficient estimator can be used in conjunction with the proposed method of moments to estimate the SAR data parameters.

The development of the method of moments illustrates the functional dependence of the phase distribution on both the number of looks and on the correlation coefficient. With a large number of looks, the distribution narrows because the mean-square difference between the sample covariance matrix estimate and the underlying covariance matrix becomes smaller. A greater correlation also narrows the phase distribution because the channels follow each other more closely.

Because the phase distribution is texture independent, the method of moments is robust against of the degree of heterogeneity. Strangely, in the case of highly heterogeneous terrain, the method of moments can predict a number of looks less than one. Even in this case, the phase histogram follows the curve predicted by the Wishart distribution with a fractional number of looks. Thus, in a sense, the Wishart distribution can be analytically continued to $0 \leq n < 2$ despite the fact that it is initially constructed only for $n \geq 2$. That the method of moments works even in extreme cases of heterogeneity gives it an advantage over techniques based upon texture dependent random variables such as the SAR intensity.

8.2 Contributions of the thesis

The contributions of this thesis are organized by chapter. In chapter 3, SAR processing tailored to the GMTI application is introduced. Application of the SPECAN algorithm to GMTI heads the contributions of this chapter. The SPECAN algorithm naturally enhances separation between moving targets and clutter and does so using only one FFT as opposed to two, as required for full SAR compression. Another contribution in this chapter is the auto-focus algorithm for moving targets based on measuring displacements between images of the targets processed using suitably chosen parameters. Autofocus of the moving targets facilitates automatic target recognition as all of the energy of a moving target is gathered to construct the "clearest" possible picture of the target. Additionally, the improved clarity aids estimation of moving target parameters due to the increased SCR. However, the trade-off between focus and SCR is non-trivial.

The well-known SAR ambiguity problem that stems from the nature of sampling is discussed with regards to moving target estimation ambiguities. A method to resolve the processing ambiguity is presented.

Notwithstanding the contributions of other chapters, chapter 4.2 presents the main contribution of this thesis. The eigen-decomposition of the covariance matrix is presented as a new, powerful, flexible approach to moving target detection. New metrics including the smallest eigenvalue, the similarity, and the independent unitary phase demonstrate the appeal of this approach. recombination of these decomposition elements yielded new non-linear detectors such as the hyperbolic detector and the eigen-projection detector that show heretofore unprecedented GMTI capability in heterogeneous terrain.

The probability distribution functions of the eigenvalues and a representation of the eigenvectors of the covariance matrix are given. Generally the eigenvectors are represented as unitary matrices on the Haar measure. In the special 2×2 case, the angular coordinates of a point on the unit sphere represent the eigenvectors. It is believed that this is the first time that the probability distribution of the complex eigenvector representation appears in the literature, and also the first time that the probability density function of the eigenvalues is given without recourse to zonal polynomials, even when correlation exists between the data channels. The joint distribution of the eigenvalues and the eigenvector representation is given. The individual marginal distributions for the 2×2 case are also given.

Owing to the statistical independence of the metrics, in some cases quasi-independence, combinations of the metrics, as in the proposed hyperbolic detector, clearly demonstrate the advantages of the decomposition in being able to detect moving targets even in highly heterogeneous terrain. This

is of tremendous importance as urban areas, where GMTI has particularly important applications, are highly heterogeneous. In summary, this proposed technique proves to be more suitable for urban areas, almost as good as conventional DPCA in homogeneous areas, quantifiable in a previously impossible way, extendable to more than two channels and mathematically fascinating.

Chapter 6 took the detection/estimation problem one step further in presenting a new method to estimate the local SAR parameters required for determination of detection thresholds. This method, based upon the moments of the phase probability density function, allows simultaneous estimation of the cross-correlation coefficient between the channels and the effective number of looks. The estimated parameters are then passed to a CFAR threshold calculator.

8.3 Suggestions for future research

Research into velocity and position estimation remains incomplete. One novel approach for doing this is to use time-frequency analysis. In particular, the wavelet decomposition might prove particularly interesting as it has adjustable time/frequency resolution capabilities. A Wigner-Ville analysis would also be interesting, but as stated in [Dau92], "The disadvantage is that the signal enters in the Wigner distribution in a quadratic rather than linear way, which is the cause of many interference phenomena." This would cause problems for resolving overlapping targets. This wavelet filtering falls into a broader issue of data filtering prior to detection and estimation. Other techniques for data filtering such as a Fractional Fourier transform could also prove valuable to the GMTI problem [CS04]

The hyperbolic detector can be adapted using the parameter p of section 4.8.2. An investigation of the appropriate choice for p depending on the terrain type deserves thought.

Although the three channel case has been introduced, data from such a system should be analysed to compare with the theoretical results. Simulated data can also be investigated to verify the theory.

A possible improvement in the probability of detection for a fixed false alarm rate could be achieved by segmentation. Although a minimum sample data set size is required to ensure sufficient accuracy in parameter estimation, the smaller the data set size, the more likely it is to be homogeneous. There is a greater probability of target detection, for a given false alarm rate, in homogeneous terrain than in heterogeneous terrain.

The method of moments is based upon a transformation of the random ATI phase variable into the Euler domain. Although the result has been used to estimate the phase distribution parameters, greater use might come from the fact that the result is the characteristic function of the phase

variable. To actually determine phase thresholds requires either the use of a lookup table, or the numerical integration of complex mathematical functions. An alternative would be to calculate the Chernoff bound using the characteristic function, and use this to compute the threshold values.

BIBLIOGRAPHY

[AG44] T. W. Anderson and M. A. Girshick. Some extensions of the wishart distribution. *Ann. Math. Stats.*, 15(4):345–357, December 1944.

[AS70] M. Abramowitz and A. Stegun. *Handbook of Mathematical Functions.* Dover, New York, 9th edition, 1970.

[Bar92] S. Barbarossa. Detection and imaging of moving objects with SAR - Part I: Optimal detection and parameter estimation. *IEE Proceedings, Part F*, 138(2):79–87, February 1992.

[BH98] R. Bamler and P. Hartl. Synthetic aperture radar interferometry (a topical review). *Inverse problems*, 14:R1–R54, 1998.

[Chi00] S. Chiu. An analysis of Radarsat 2 SAR-GMTI performance for standard beam mode. Technical Report TR 2000-088, Defence Research and Development Canada, December 2000.

[Chi03] S. Chiu. Clutter effects on ground moving target velocity estimation with SAR along-track interferometry. In *Proc. of IGARSS 2003*, 2003.

[CP96] S. R. Cloude and E Pottier. A review of target decompostition theorems in radar polarimetry. *IEEE Trans. Geosci. and Rem. Sens.*, 34(2):498–518, March 1996.

[CS04] S. Chiu and I. C. Sikaneta. Applying fractional Fourier transfrom to two-aperture SAR-GMTI. *Proc. 2004 EuSAR conf.*, 2004.

[Dau92] I. Daubechies. *Ten Lectures on Wavelets.* Society for Industrial and Applied Mathematics, Philadelphia, 1992.

[Ede89] A. Edelman. *Eigenvalues and Condition Numbers of Random Matrices.* PhD thesis, Massachusettes Institute of Technology, May 1989.

[FL99] G. Franceschetti and R. Lanari. *Synthetic Aperture Radar Processing.* CRC Press, Washington, 1999.

[Gie97] C. H. Gierull. Statistical analysis of the eigenvector projection method for adaptive spatial filtering of interference. *IEE Proceedings*, 144(2):57–63, April 1997.

[Gie01a] C. H. Gierull. Statistics of SAR interferograms with application to moving target detection. Technical Report TR 2001-045, Defence Research and Development Canada, July 2001.

[Gie01b] C. H. Gierull. Unbiased coherence estimator for SAR interferometry with application to moving target detection. *Electronics Letters*, 37(14):913–915, July 2001.

[Gie02] C. H. Gierull. Moving target detection with along-track SAR interferometry. Technical Report TR 2002-084, Defence Research and Development Canada, January 2002.

[Gie03] C. H. Gierull. Digital channel balancing of along-track interferometric SAR data. Technical Memorandum TM 2003-024, Defence Research and Development Canada, March 2003.

[Gie04] C. H. Gierull, Christoph. Statistical analysis of multilook SAR interferograms for CFAR detection of ground moving targets. *IEEE Trans. Geosci. and Rem. Sens.*, 42(4):691–701, April 2004.

[Gir90] V. L. Girko. *Theory of Random Determinants*, volume 45. Kluwer Academic Publishers, London, 1990.

[GL03] C. H. Gierull and C. E. Livingstone. *The Applications of Space-Time Processing*, chapter SAR GMTI concept for RADARSAT-2. IEE Publishers, 2003.

[Goo63] N. R. Goodman. Statistical analysis based on a certain multivariate complex gaussian distribution (an introduction). *Annals of Mathematical Statistics*, 34(1):152–177, March 1963.

[GR00] I. S. Gradshteyn and I. M. Ryzhik. *Table of Integrals, Series and Products.* Academic Press, New York, sixth edition, 2000.

[Gra02] Alex Grant. Rayleigh fading multi-antenna channels. *EURASIP J. on App. Sig. Proc.*, 2002(3):316–329, March 2002. Special issue on space-time coding (Part 1).

[GS02] C. H. Gierull and I. C. Sikaneta. Estimating the effective number of looks in interferometric SAR data. *Submitted to IEEE Trans. Geosci. and Rem. Sens*, February 2002.

[GS03] C. H. Gierull and I. C. Sikaneta. Raw data based two-aperture SAR ground moving target indication. In *Proc. of IGARSS 2003*, 2003.

[GVL96] G. H. Golub and C. F. Van Loan. *Matrix Computations.* Johns Hopkins University Press, Baltimore, third edition, 1996.

[HL98] F. M. Henderson and A. J. Lewis. *Principles and Applications of Imaging Radar*, volume 2. John Wiley and Sons, Inc., Mew York, third edition, 1998.

[Hov80] S. A. Hovanessian. *Introduction to Synthetic Array and Imaging Radars.* Artech House Inc., Washington, 1980.

[HT03] U. Haagerup and S. Thorbjørnsen. Random matrices with complex gaussian entries, 2003.

[Jam64] A. T. James. Distributions of matrix variates and latent roots derived from normal samples. *Ann. Math. Stats.*, 35(2):475–501, June 1964.

[JN02] A. Janik, Romuald and A. Nowak, Maciej. Wishart and anti-Wishart random matrices. *e-print math-ph/0112017*, 2, January 2002.

[JWP94] I. R. Joughin, D. P. Winebrenner, and D. B. Percival. Probablility density functions for multilook polarimetric signatures. *IEEE Trans. Geosci and Rem. Sens.*, 32(3):562–574, May 1994.

[Kle98] R. Klemm. *Space-Time Adaptive Processing: Principles and Applications.* The Institution of Electrical Engineers, London, 1998.

[Liv03] C. E. Livingstone. Focusing moving targets/terrain imaged with moving-target matched filters, April 2003. Chuck's note on the phase jump.

[LMH94] J. S. Lee, A. R. Miller, and K. W. Hoppel. Statistics of phase difference and product magnitude of multi–look processed gaussian signals. *Waves in Random Media. IOP Publishing Inc. London UK*, 4:307–317, 1994.

[LSG+02] C.E. Livingstone, I. Sikaneta, C.H. Gierull, S. Chiu, A. Beaudoin, J. Campbell, J. Beaudoin, S. Gong, and T.A. Knight. An airborne synthetic aperture radar (SAR) experiment to support RADARSAT-2 ground moving target indication (GMTI). *Can. J. Rem. Sens.*, 28(6):1–20, 2002.

[Meh67] M. L. Mehta. *Random Matrices and the Statistical Theory of Energy Levels.* Academic Press, New York and London, 1967.

[Mor91] A Moreira. Improved multilook techniques applied to SAR and SCANSAR imagery. *IEEE Trans. Geosci. Rem. Sens.*, 39:529–534, 1991.

[Mun00] K. Munson. General Atomics Gnat. *Janes Unmanned Aerial Vehicles and Targets*, 15, August 2000.

[OQ98] C. J. Oliver and S. Quegan. *Understanding Synthetic Aperture Radar Images.* Artech House Inc., Boston, 1998.

[SCR01] I. Sikaneta, J. Campbell, and M. Robson. The airborne along track INSAR processor: Documentation, guide, history. Technical Memorandum TM 2001-053, Defence Research and Development Canada, August 2001.

[SGC03] I. C. Sikaneta, C. H. Gierull, and J-Y. Chouinard. Metrics for SAR-GMTI based on eigen-decomposition of the sample covariance matrix. *Proc. of IEEE Int. Conf. on Radar*, September 2003.

[Sha04] J. J. Sharma. Simulation of SAR signals from moving vehicles (focusing accelerating ground moving targets). *Proc. 2004 EuSAR conf.*, 2004.

[Sou99] M. Soumekh. *Synthetic Aperture Radar Signal Processing With MATLAB Algorithms.* Wiley and Sons, New York, 1999.

[Spi64] M. R. Spiegel. *Theory and Problems of Complex Variables.* Schaums, New York, 1964.

[Spi94] M. R. Spiegel. *Theory and Problems of Probability and Statistics.* McGraw-Hill, New York, 1994.

[TBQ95] R. A. J. Tough, D Blacknell, and S. Quegan. A statistical description of polarimetric and interferometric synthetic aperture radar data. *Proc. R. Soc. Lond., A. Math. Phs. Sci*, A(449):567–589, 1995.

[UMF86] F. T. Ulaby, R. K. Moore, and A. K. Fung. *Microwave Remote Sensing: Active and Passive*, volume III. Artech House, Norwood, 1986.

[Wig67] E. P. Wigner. Random matrices in physics. *SIAM Review*, 9(1):1–23, January 1967.

[Wis28] J. Wishart. The generalized product moment distribution in samples from a normal multivariate population. *Biometrika*, 20A(12):32–52, July 1928.

APPENDIX A
INCORRECT DOPPLER RATE COMPRESSION

For the case where the signal and the reference function have compact support, the output of the SAR correlator with an incorrect Doppler rate can be written as

$$d(\tau) = e^{j(b_0 - a_0 - a_1\tau - a_2\tau^2)} \int_{t_1}^{t_2} e^{jB(t+t_0)^2 - jBt_0^2} dt, \tag{A.1}$$

where $B = b_2 - a_2$ and $t_0 = (b_1 - a_1 - 2a_2\tau)/(2b_2 - 2a_2)$, and t_1, t_2 account for the compact support. The squared envelope of $d(\tau)$ can be written as

$$|d(\tau)|^2 = \int_{t_1}^{t_2} \int_{t_1}^{t_2} e^{jB(x+t_0)^2 - jB(y+t_0)^2} dx dy. \tag{A.2}$$

By changing the integration variables according to

$$u = x + y \tag{A.3}$$

$$v = x - y, \tag{A.4}$$

the domain of integration becomes as shown in figure A.1. The Jacobian contributes a factor of $1/2$, and the correlator output becomes the sum of the two integrals given by

$$|d(\tau)|^2 = \frac{1}{2} \int_{2t_1}^{t_1+t_2} \int_{2t_1-u}^{u-2t_1} e^{jBv(u+2t_0)} dv du + \frac{1}{2} \int_{t_1+t2}^{2t_2} \int_{u-2t_2}^{2t_2-u} e^{jBv(u+2t_0)} dv du. \tag{A.5}$$

Integration over v followed by an appropriate shift in u leads to

$$|d(\tau)|^2 = \int_0^{t_2-t_1} \frac{\sin[Bu(u + 2t_1 + 2t_0)]}{B(u + 2t_1 + 2t_0)} du + \int_0^{t_2-t_1} \frac{\sin[Bu(u - 2t_2 - 2t_0)]}{B(u - 2t_2 - 2t_0)} du, \tag{A.6}$$

the result stated in (3.26).

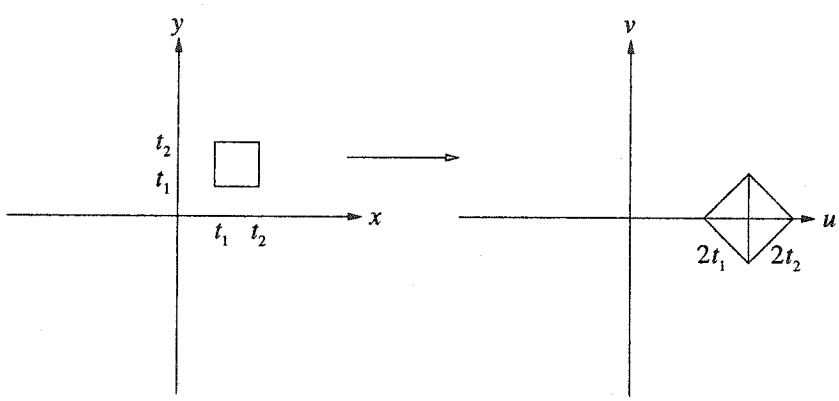

Figure A.1. Transformation of integration domain.

APPENDIX B

DERIVATION OF PROBABILITY DENSITY FUNCTIONS OF DECOMPOSED COVARIANCE MATRIX ELEMENTS

In this appendix, the expressions for the probability density functions of the decomposed covariance matrix elements are derived. The derivations are all based on marginalization of the complex Wishart distribution of the sample covariance matrix.

B.1 Calculation of the decomposition Jacobian

Take the derivative of $\boldsymbol{R}$ with respect to λ_i

$$\frac{\partial \boldsymbol{R}}{\partial \lambda_i} = \boldsymbol{U}\frac{\partial \boldsymbol{D}}{\partial \lambda_i}\boldsymbol{U}^\dagger. \tag{B.1}$$

Next, differentiate with respect to α_i to get

$$\begin{aligned}\frac{\partial \boldsymbol{R}}{\partial \alpha_i} &= \frac{\partial \boldsymbol{U}\boldsymbol{D}\boldsymbol{U}^\dagger}{\partial \alpha_i} \\ &= \frac{\partial \boldsymbol{U}}{\partial \alpha_i}\boldsymbol{D}\boldsymbol{U}^\dagger + \boldsymbol{U}\boldsymbol{D}\frac{\partial \boldsymbol{U}^\dagger}{\partial \alpha_i}.\end{aligned} \tag{B.2}$$

Differentiation of the unitary relation yields

$$\begin{aligned}\frac{\partial \boldsymbol{U}^\dagger \boldsymbol{U}}{\partial \alpha_i} &= \frac{\partial \boldsymbol{I}}{\partial \alpha_i} \\ \frac{\partial \boldsymbol{U}^\dagger}{\partial \alpha_i}\boldsymbol{U} + \boldsymbol{U}^\dagger\frac{\partial \boldsymbol{U}}{\partial \alpha_i} &= \boldsymbol{0} \\ \frac{\partial \boldsymbol{U}^\dagger}{\partial \alpha_i}\boldsymbol{U} &= -\boldsymbol{U}^\dagger\frac{\partial \boldsymbol{U}}{\partial \alpha_i}.\end{aligned} \tag{B.3}$$

Thus, writing

$$\boldsymbol{S}^i = \boldsymbol{U}^\dagger\frac{\partial \boldsymbol{U}}{\partial \alpha_i}, \tag{B.4}$$

and pre-multiplying (B.2) by $\boldsymbol{U}^\dagger$ and post-multiplying by $\boldsymbol{U}$ one finds that (B.2) can be written as

$$\boldsymbol{U}^\dagger\frac{\partial \boldsymbol{R}}{\partial \alpha_i}\boldsymbol{U} = \boldsymbol{S}^i\boldsymbol{D} - \boldsymbol{D}\boldsymbol{S}^i. \tag{B.5}$$

To be more specific, differentiation of $R_{lm} \in \mathcal{C}$ with respect to $\alpha_i \in \mathcal{R}$ means,

$$\frac{\partial R_{lm}}{\partial \alpha_i} = \frac{\partial R_{lm}^{(0)}}{\partial \alpha_i} + j\frac{\partial R_{lm}^{(1)}}{\partial \alpha_i}. \tag{B.6}$$

The derivative relations can be written in terms of elements as

$$\begin{aligned}
\sum_{l=1}^{k}\sum_{m=1}^{k} \frac{\partial R_{lm}}{\partial \alpha_i} U_{pl}^{\dagger} U_{mq} &= S_{pq}^{i}(\lambda_q - \lambda_p), \\
\sum_{l=1}^{k}\sum_{m=1}^{k} \frac{\partial R_{lm}}{\partial \lambda_i} U_{pl}^{\dagger} U_{mq} &= \delta_{pq}\delta_{pi},
\end{aligned} \tag{B.7}$$

where δ_{pq} is the Delta-Kronecker symbol. Upon writing $W_{plmq} = U_{pl}^{\dagger} U_{mq}$ and equating real and imaginary parts one finds that

$$\begin{aligned}
\sum_{l=1}^{k}\sum_{m=1}^{k} \frac{\partial R_{lm}^{(0)}}{\partial \alpha_i} W_{plmq}^{(0)} - \sum_{l=1}^{k}\sum_{m=1}^{k} \frac{\partial R_{lm}^{(1)}}{\partial \alpha_i} W_{plmq}^{(1)} &= S_{pq}^{i(0)}(\lambda_q - \lambda_p), \\
\sum_{l=1}^{k}\sum_{m=1}^{k} \frac{\partial R_{lm}^{(0)}}{\partial \alpha_i} W_{plmq}^{(1)} + \sum_{l=1}^{k}\sum_{m=1}^{k} \frac{\partial R_{lm}^{(1)}}{\partial \alpha_i} W_{plmq}^{(0)} &= S_{pq}^{i(1)}(\lambda_q - \lambda_p), \\
\sum_{l=1}^{k}\sum_{m=1}^{k} \frac{\partial R_{lm}^{(0)}}{\partial \lambda_i} W_{plmq}^{(0)} - \sum_{l=1}^{k}\sum_{m=1}^{k} \frac{\partial R_{lm}^{(1)}}{\partial \lambda_i} W_{plmq}^{(1)} &= \delta_{pq}\delta_{pi}, \\
\sum_{l=1}^{k}\sum_{m=1}^{k} \frac{\partial R_{lm}^{(0)}}{\partial \lambda_i} W_{plmq}^{(1)} + \sum_{l=1}^{k}\sum_{m=1}^{k} \frac{\partial R_{lm}^{(1)}}{\partial \lambda_i} W_{plmq}^{(0)} &= 0.
\end{aligned} \tag{B.8}$$

For compact notation, denote $k_2 = k(k-1)/2$. The Jacobian matrix is

$$J = \begin{bmatrix}
\frac{\partial R_{11}}{\partial \lambda_1} & \frac{\partial R_{22}}{\partial \lambda_1} \cdots & \frac{\partial R_{kk}}{\partial \lambda_1} & \frac{\partial R_{12}^{(0)}}{\partial \lambda_1} & \frac{\partial R_{13}^{(0)}}{\partial \lambda_1} \cdots & \frac{\partial R_{k(k-1)}^{(0)}}{\partial \lambda_1} & j\frac{\partial R_{12}^{(1)}}{\partial \lambda_1} & j\frac{\partial R_{13}^{(1)}}{\partial \lambda_1} \cdots & j\frac{\partial R_{k(k-1)}^{(1)}}{\partial \lambda_1} \\
\vdots & \vdots & \vdots & \vdots & \vdots & \vdots & \vdots & \vdots & \vdots \\
\frac{\partial R_{11}}{\partial \lambda_k} & \frac{\partial R_{22}}{\partial \lambda_k} \cdots & \frac{\partial R_{kk}}{\partial \lambda_k} & \frac{\partial R_{12}^{(0)}}{\partial \lambda_k} & \frac{\partial R_{13}^{(0)}}{\partial \lambda_k} \cdots & \frac{\partial R_{k(k-1)}^{(0)}}{\partial \lambda_k} & j\frac{\partial R_{12}^{(1)}}{\partial \lambda_k} & j\frac{\partial R_{13}^{(1)}}{\partial \lambda_k} \cdots & j\frac{\partial R_{k(k-1)}^{(1)}}{\partial \lambda_k} \\
\frac{\partial R_{11}}{\partial \alpha_1} & \frac{\partial R_{22}}{\partial \alpha_1} \cdots & \frac{\partial R_{kk}}{\partial \alpha_1} & \frac{\partial R_{12}^{(0)}}{\partial \alpha_1} & \frac{\partial R_{13}^{(0)}}{\partial \alpha_1} \cdots & \frac{\partial R_{k(k-1)}^{(0)}}{\partial \alpha_1} & j\frac{\partial R_{12}^{(1)}}{\partial \alpha_1} & j\frac{\partial R_{13}^{(1)}}{\partial \alpha_1} \cdots & j\frac{\partial R_{k(k-1)}^{(1)}}{\partial \alpha_1} \\
\vdots & \vdots & \vdots & \vdots & \vdots & \vdots & \vdots & \vdots & \vdots \\
\frac{\partial R_{11}}{\partial \alpha_{k_2}} & \frac{\partial R_{22}}{\partial \alpha_{k_2}} \cdots & \frac{\partial R_{kk}}{\partial \alpha_{k_2}} & \frac{\partial R_{12}^{(0)}}{\partial \alpha_{k_2}} & \frac{\partial R_{13}^{(0)}}{\partial \alpha_{k_2}} \cdots & \frac{\partial R_{k(k-1)}^{(0)}}{\partial \alpha_{k_2}} & j\frac{\partial R_{12}^{(1)}}{\partial \alpha_{k_2}} & j\frac{\partial R_{13}^{(1)}}{\partial \alpha_{k_2}} \cdots & j\frac{\partial R_{k(k-1)}^{(1)}}{\partial \alpha_{k_2}}
\end{bmatrix}. \tag{B.9}$$

Post-multiply J on the right by the matrix

$$\boldsymbol{Y} = \begin{bmatrix} W^{(0)}_{p_1 11 q_1} & \cdots & jW^{(1)}_{p_2 11 q_2} & \cdots \\ W^{(0)}_{p_1 22 q_1} & \cdots & jW^{(1)}_{p_2 22 q_2} & \cdots \\ \vdots & \cdots & \vdots & \cdots \\ W^{(0)}_{p_1 kk q_1} & \cdots & jW^{(1)}_{p_2 kk q_2} & \cdots \\ W^{(0)}_{p_1 12 q_1} & \cdots & jW^{(1)}_{p_2 12 q_2} & \cdots \\ W^{(0)}_{p_1 13 q_1} & \cdots & jW^{(1)}_{p_2 13 q_2} & \cdots \\ \vdots & \cdots & \vdots & \cdots \\ W^{(0)}_{p_1 k(k-1) q_1} & \cdots & jW^{(1)}_{p_2 k(k-1) q_2} & \cdots \\ jW^{(1)}_{p_1 12 q_1} & \cdots & W^{(0)}_{p_2 12 q_2} & \cdots \\ jW^{(1)}_{p_1 13 q_1} & \cdots & W^{(0)}_{p_2 13 q_2} & \cdots \\ \vdots & \cdots & \vdots & \cdots \\ jW^{(1)}_{p_1 k(k-1) q_1} & \cdots & W^{(0)}_{p_2 k(k-1) q_2} & \cdots \end{bmatrix}, \tag{B.10}$$

where $p_1 \leq q_1 \leq k$, ordered as $p_1 q_1 = \{11, 22, \ldots, kk, 12, 13, \ldots, k(k-1), \ldots\}$, and $p_2 < q_2 \leq k$, to obtain

$$\boldsymbol{JY} = \begin{bmatrix} \begin{bmatrix} 1 & 0 & \cdots & 0 \\ 0 & 1 & \cdots & 0 \\ \vdots & \vdots & \vdots & \vdots \\ 0 & 0 & \cdots & 1 \end{bmatrix} & \begin{bmatrix} 0 & 0 & \cdots & 0 \\ 0 & 0 & \cdots & 0 \\ \vdots & \vdots & \vdots & \vdots \\ 0 & 0 & \cdots & 0 \end{bmatrix} \\ \begin{bmatrix} S^{1(0)}_{p_1 q_1}(\lambda_{q_1} - \lambda_{p_1}) & \cdots \\ S^{2(0)}_{p_1 q_1}(\lambda_{q_1} - \lambda_{p_1}) & \cdots \\ \vdots & \vdots \\ S^{k(k-1)(0)}_{p_1 q_1}(\lambda_{q_1} - \lambda_{p_1}) & \cdots \end{bmatrix} & \begin{bmatrix} S^{1(1)}_{p_2 q_2}(\lambda_{q_2} - \lambda_{p_2}) & \cdots \\ S^{2(1)}_{p_2 q_2}(\lambda_{q_2} - \lambda_{p_2}) & \cdots \\ \vdots & \vdots \\ S^{k(k-1)(1)}_{p_2 q_2}(\lambda_{q_2} - \lambda_{p_2}) & \cdots \end{bmatrix} \end{bmatrix} \tag{B.11}$$

The first k terms in the bottom left matrix involving $S^{i(0)}_{p_1 q_1}(\lambda_{q_1} - \lambda_{p_1})$ will vanish as we have ordered the $p_1 q_1$ to start with $p_1 = q_1$. The remaining terms which are the permutations of $p_1 < q_1 \leq k$ will not vanish. One can take the determinant of both sides,

$$\det(\boldsymbol{JY}) = \det\begin{bmatrix}\begin{bmatrix} S_{p_2q_2}^{1(0)}(\lambda_{q_2}-\lambda_{p_2}) & \cdots \\ S_{p_2q_2}^{2(0)}(\lambda_{q_2}-\lambda_{p_2}) & \cdots \\ \vdots & \vdots \\ S_{p_2q_2}^{k(k-1)(0)}(\lambda_{q_2}-\lambda_{p_2}) & \cdots \end{bmatrix} & \begin{bmatrix} S_{p_2q_2}^{1(1)}(\lambda_{q_2}-\lambda_{p_2}) & \cdots \\ S_{p_2q_2}^{2(1)}(\lambda_{q_2}-\lambda_{p_2}) & \cdots \\ \vdots & \vdots \\ S_{p_2q_2}^{k(k-1)(1)}(\lambda_{q_2}-\lambda_{p_2}) & \cdots \end{bmatrix}\end{bmatrix}$$
$$= \left[\prod_{p_2,q_2}(\lambda_{q_2}-\lambda_{p_2})^2\right]\det\begin{bmatrix}\begin{bmatrix} S_{p_2q_2}^{1(0)} & \cdots \\ S_{p_2q_2}^{2(0)} & \cdots \\ \vdots & \vdots \\ S_{p_2q_2}^{k(k-1)(0)} & \cdots \end{bmatrix} & \begin{bmatrix} S_{p_2q_2}^{1(1)} & \cdots \\ S_{p_2q_2}^{2(1)} & \cdots \\ \vdots & \vdots \\ S_{p_2q_2}^{k(k-1)(1)} & \cdots \end{bmatrix}\end{bmatrix}. \tag{B.12}$$

Since $\det\boldsymbol{Y} = 1$ [Meh67], we have an expression for the Jacobian matrix of the transformation.

B.2 Derivation of marginal probability density function of similarity

It is not straightforward to integrate over the eigenvalues, λ_i, from (4.30) to get the marginal joint pdf of δ and θ because of the domain of integration of the eigenvalues, $0 < \lambda_2 < \lambda_1 < \infty$. However, in the case where the channels are balanced in power, (i.e. that the diagonal elements of the covariance matrix are equal), one can derive the probability distribution of θ. In this case, the exponential trace expression for the joint pdf in (4.30) can be written as

$$\begin{aligned} &-\mathrm{Tr}\left(\boldsymbol{U}^\dagger\begin{bmatrix}\sigma^2 & \sigma^2\rho e^{j\phi}\\ \sigma^2\rho e^{-j\phi} & \sigma^2\end{bmatrix}^{-1}\boldsymbol{U}\begin{bmatrix}\lambda_1 & 0\\ 0 & \lambda_2\end{bmatrix}\right) \\ &= -\frac{1-\rho\cos(\delta-\phi)\sin(2\theta)}{\sigma^2(1-\rho^2)}\lambda_1 - \frac{1+\rho\cos(\delta-\phi)\sin(2\theta)}{\sigma^2(1-\rho^2)}\lambda_2. \end{aligned} \tag{B.13}$$

The required integral thus becomes,

$$f_\Theta(\theta) = \int_0^\infty\int_0^{\lambda_1}\int_{-\pi}^{\pi}\frac{(\lambda_1\lambda_2)^{n-2}(\lambda_1-\lambda_2)^2\sin(2\theta)}{2\pi\Gamma(n)\Gamma(n-1)(s_1s_2)^n} \exp\left(-\frac{1-\rho\cos(\delta-\phi)\sin(2\theta)}{\sigma^2(1-\rho^2)}\lambda_1 - \frac{1+\rho\cos(\delta-\phi)\sin(2\theta)}{\sigma^2(1-\rho^2)}\lambda_2\right)\mathrm{d}\delta\mathrm{d}\lambda_2\mathrm{d}\lambda_1, \tag{B.14}$$

where we recall, from (4.5), that s_1 and s_2 are the eigenvalues of the underlying covariance matrix $\boldsymbol{R}$.

We claim that the integrand of (B.14) is symmetric in λ_1 and λ_2[1] under the condition that one conducts integration over δ. Although one sees this symmetry in the term outside the exponential, the exponential argument appears asymmetric. Note that (B.14) is periodic in δ, and that integration over δ does not depend on ϕ. To understand the independence from ϕ, recall that $\cos x$ achieves all its possible values over the interval $x \in [\phi, \phi + 2\pi)$ no matter the value of ϕ. In fact, all values are achieved twice except for the two zero-measure extreme points where it evaluates to ± 1. Thus one can write,

$$\begin{aligned}
\int_{-\pi}^{\pi} f(\cos(\delta - \phi))\mathrm{d}\delta &\equiv \int_{-\pi}^{\pi} f(\cos\delta)\mathrm{d}\delta \\
&= 2\int_{0}^{\pi/2} f(\cos\delta)\mathrm{d}\delta + 2\int_{-\pi}^{-\pi/2} f(\cos\delta)\mathrm{d}\delta \\
&= 2\int_{0}^{\pi/2} f(\cos\delta)\mathrm{d}\delta + 2\int_{0}^{\pi/2} f(\cos(\delta - \pi))\mathrm{d}\delta \\
&= 2\int_{0}^{\pi/2} f(\cos\delta)\mathrm{d}\delta + 2\int_{0}^{\pi/2} f(-\cos(\delta))\mathrm{d}\delta \\
&= 2\int_{0}^{\pi/2} [f(\cos\delta) + f(-\cos\delta)]\mathrm{d}\delta.
\end{aligned}$$

The above equivalence can be used to rewrite (B.14) as

$$\begin{aligned}
f_{\Theta}(\theta) = \int_0^{\infty}\int_0^{\lambda_1}\int_{-\pi}^{\pi} & \frac{(\lambda_1\lambda_2)^{n-2}(\lambda_1 - \lambda_2)^2 \sin(2\theta)}{2\pi\Gamma(n)\Gamma(n-1)(s_1 s_2)^n} \\
& \left[\exp\left(-\frac{1 - \rho\cos\delta\sin(2\theta)}{\sigma^2(1-\rho^2)}\lambda_1 - \frac{1 + \rho\cos\delta\sin(2\theta)}{\sigma^2(1-\rho^2)}\lambda_2\right)\right. \\
& \left. + \exp\left(-\frac{1 + \rho\cos\delta\sin(2\theta)}{\sigma^2(1-\rho^2)}\lambda_1 - \frac{1 - \rho\cos\delta\sin(2\theta)}{\sigma^2(1-\rho^2)}\lambda_2\right)\right]\mathrm{d}\delta\mathrm{d}\lambda_1\mathrm{d}\lambda_2,
\end{aligned} \tag{B.15}$$

which, upon inspection is revealed to be symmetric in λ_1 and λ_2. Because of this symmetry, the integration limits may be taken to be $[0, \infty)$ for both λ_1 and λ_2 with subsequent division by two. Integration over the eigenvalues in (B.14), using

$$\int_0^{\infty} x^{\nu-1}e^{-\beta x} = \frac{\Gamma(\nu)}{\beta^{\nu}}, \quad \beta > 0 \in \mathcal{R} \tag{B.16}$$

leads to the following expression

$$\frac{\sin(2\theta)}{4\pi(s_1 s_2)^n\Gamma(n)\Gamma(n-1)}\left[\frac{\Gamma(n+1)\Gamma(n-1)}{A^{n+1}B^{n-1}} - 2\frac{\Gamma(n)\Gamma(n)}{A^n B^n} + \frac{\Gamma(n-1)\Gamma(n+1)}{A^{n-1}B^{n+1}}\right], \tag{B.17}$$

[1] i.e. a function of the form, $f(\lambda_1, \lambda_2) = f(\lambda_2, \lambda_1)$.

where,

$$A = \frac{1 - \rho\cos(\delta - \phi)\sin(2\theta)}{\sigma^2(1-\rho^2)}$$
$$B = \frac{1 + \rho\cos(\delta - \phi)\sin(2\theta)}{\sigma^2(1-\rho^2)}. \tag{B.18}$$

One can rearrange the terms to get

$$\begin{aligned}
f_{\Theta,\Delta}(\theta,\delta) &= \frac{\sin(2\theta)\Gamma(n)\Gamma(n-1)}{4\pi(s_1 s_2)^n\Gamma(n)\Gamma(n-1)A^{n+1}B^{n+1}}\left[A^2 n + B^2 n - 2AB(n-1)\right] \\
&= \frac{\sin(2\theta)}{4\pi(\sigma^2(1+\rho)\sigma^2(1-\rho))^n(AB)^{n+1}}\left[A^2 n + B^2 n - 2AB(n-1)\right] \\
&= \frac{\sin(2\theta)(\sigma^4(1-\rho^2)^2)^{n+1}}{4\pi(\sigma^4(1-\rho^2))^n((1-\rho^2\cos^2(\delta-\phi)\sin^2(2\theta))^{n+1}}\left[A^2 n + B^2 n - 2AB(n-1)\right] \\
&= \frac{\sin(2\theta)(1-\rho^2)^{n+1}\sigma^4(1-\rho^2)}{2\pi((1-\rho^2\cos^2(\delta-\phi)\sin^2(2\theta))^{n+1}}\left[\frac{(2n-1)\rho^2\cos^2(\delta-\phi)\sin^2(2\theta)+1}{\sigma^4(1-\rho^2)^2}\right] \\
&= \frac{\sin(2\theta)(1-\rho^2)^n}{2\pi((1-\rho^2\cos^2(\delta-\phi)\sin^2(2\theta))^{n+1}}\left[(2n-1)\rho^2\cos^2(\delta-\phi)\sin^2(2\theta)+1\right] \\
&= \frac{\sin(2\theta)(1-\rho^2)^n}{2\pi((1-\rho^2\cos^2(\delta-\phi)\sin^2(2\theta))^{n+1}}\left[(2n-1)[\rho^2\cos^2(\delta-\phi)\sin^2(2\theta)-1]+(2n-1)+1\right] \\
&= \frac{\sin(2\theta)(1-\rho^2)^n}{2\pi((1-\rho^2\cos^2(\delta-\phi)\sin^2(2\theta))^{n+1}}\left[(1-2n)[1-\rho^2\cos^2(\delta-\phi)\sin^2(2\theta)]+2n\right] \\
&= \frac{(1-2n)(1-\rho^2)^n\sin(2\theta)}{2\pi(\rho^2\sin^2 2\theta)^n(\rho^{-2}\sin^{-2}2\theta - \cos^2(\delta-\phi))^n} \\
&+ \frac{2n(1-\rho^2)^n\sin(2\theta)}{2\pi(\rho^2\sin^2 2\theta)^{n+1}(\rho^{-2}\sin^{-2}2\theta - \cos^2(\delta-\phi))^{n+1}}
\end{aligned} \tag{B.19}$$

Integration over δ using

$$\int_{-\pi}^{\pi}\frac{1}{(a^2-\cos^2(\theta-\theta_0))^n}\mathrm{d}\theta = 2\pi a^{-2n}{}_2F_1(n,1/2;1;a^{-2}) \tag{B.20}$$

leads to the marginal pdf for Θ

$$\begin{aligned}
f_\Theta(\theta) &= (1-\rho^2)^n\sin(2\theta) \\
&\cdot\left[2n\ {}_2F_1(1+n,1/2;1;\rho^2\sin^2(2\theta)) + (1-2n)\ {}_2F_1(n,1/2;1;\rho^2\sin^2(2\theta))\right].
\end{aligned} \tag{B.21}$$

B.3 Joint distribution of similarity and phase

One can also calculate the joint probability density function of Θ and Δ. From (4.30),

$$f_{\Theta\Delta}(\theta,\delta) = \frac{\sin(2\theta)}{2\pi\Gamma(n)\Gamma(n-1)(s_1 s_2)^n}\int_0^\infty\int_0^{\lambda_1}(\lambda_1\lambda_2)^{n-2}(\lambda_1-\lambda_2)^2 e^{-A\lambda_1-B\lambda_2}\mathrm{d}\lambda_2\mathrm{d}\lambda_1, \tag{B.22}$$

where

$$A = \frac{1-\rho\cos\delta\sin(2\theta)}{\sigma^2(1-\rho^2)},\quad B = \frac{1+\rho\cos\delta\sin(2\theta)}{\sigma^2(1-\rho^2)}. \tag{B.23}$$

Transformation of λ_1 and λ_2 into spherical-polar coordinates gives

$$f_{\Theta\Delta}(\theta,\delta) = \frac{\sin(2\theta)}{2\pi\Gamma(n)\Gamma(n-1)(s_1 s_2)^n} \int_0^{\pi/4}\int_0^\infty (r^2\cos\alpha\sin\alpha)^{n-2} r^2(\cos\alpha-\sin\alpha)^2 e^{-r(A\cos\alpha+B\sin\alpha)} r\mathrm{d}r\mathrm{d}\alpha. \tag{B.24}$$

Evaluation of the integral over r leaves

$$f_{\Theta\Delta}(\theta,\delta) = \frac{\sin(2\theta)\Gamma(2n)}{2\pi\Gamma(n)\Gamma(n-1)(s_1 s_2)^n}\int_0^{\pi/4}\frac{(\cos\alpha\sin\alpha)^{n-2}(\cos\alpha-\sin\alpha)^2}{(A\cos\alpha+B\sin\alpha)^{2n}}\mathrm{d}\alpha. \tag{B.25}$$

It is useful to multiply the numerator and denominator of the integrand by $(\cos\alpha)^{-2n}$ and to write the integral in terms of the $\tan(\alpha)$ function as

$$f_{\Theta\Delta}(\theta,\delta) = \frac{\sin(2\theta)\Gamma(2n)}{2\pi\Gamma(n)\Gamma(n-1)(s_1 s_2)^n}\int_0^{\pi/4}\frac{(\tan\alpha)^{n-2}(1-\tan\alpha)^2\sec^2\alpha}{(A+B\tan\alpha)^{2n}}\mathrm{d}\alpha, \tag{B.26}$$

because one can then change variables using $u = 1-\tan\alpha$ to get

$$f_{\Theta\Delta}(\theta,\delta) = \frac{\sin(2\theta)\Gamma(2n)}{2\pi\Gamma(n)\Gamma(n-1)(s_1 s_2)^n(A+B)^{2n}}\int_0^1\frac{(1-u)^{n-2}u^2}{(1-Bu/(A+B))^{2n}}\mathrm{d}u. \tag{B.27}$$

By definition, the above integral is a Gauss hypergeometric function, definition (9.111) in [GR00]. The final result is thus

$$\begin{aligned} f_{\Theta\Delta}(\theta,\delta) &= \frac{\sin(2\theta)\Gamma(2n)}{2\pi\Gamma(n)\Gamma(n-1)(s_1 s_2)^n(A+B)^{2n}}\frac{2\Gamma(n-1)}{\Gamma(n+2)}{}_2F_1(2n,3;n+2;B/(A+B)) \\ &= \frac{\sin(2\theta)\Gamma(n+1/2)(1-\rho^2)^n}{2\pi^{3/2}\Gamma(n+2)}{}_2F_1(2n,3;n+2;(1+\rho\cos\delta\sin(2\theta))/2). \end{aligned} \tag{B.28}$$

B.4 Marginal probability distribution of unitary phase

The derivation for the marginal probability density function of the unitary phase follows from section B.3. However, after the unitary transformation, the factors A and B are seen to be

$$A = \frac{\cos^2\vartheta}{s_1} + \frac{\sin^2\vartheta}{s_2}, \quad B = \frac{\cos^2\vartheta}{s_2} + \frac{\sin^2\vartheta}{s_1}. \tag{B.29}$$

The unitary transformation corresponds to a unit Jacobian, and integration over δ contributes 2π. One thus finds that the probability density function of the unitary phase is given by

$$f_\vartheta(\vartheta) = \frac{2\sin(2\vartheta)\Gamma(2n)(s_1s_2)^n}{\Gamma(n)\Gamma(n-1)(s_1+s_2)^{2n}} \frac{\Gamma(n-1)}{\Gamma(n+2)} {}_2F_1(2n, 3; n+2; \frac{s_2\sin^2\vartheta + s_1\cos^2\vartheta}{s_1+s_2}) \tag{B.30}$$

B.5 Marginal probability density function of the eigenvalues

The group of unitary transformations with the Haar measure allows the Lebesgue integral to be defined over the group, thereby leading to a meaningful mathematical definition of the probability measure for the eigenvalues and eigenvectors of the sample covariance matrix [Gir90]. One critically important quality of a Haar measure is its invariance under group transformations. That is [Gir90],

$$\int_{\boldsymbol{U}} \mathrm{d}\boldsymbol{U} = \int_{\boldsymbol{U}} \mathrm{d}\boldsymbol{L}\boldsymbol{U}, \tag{B.31}$$

where $\boldsymbol{L}$ is some arbitrary unitary transformation. One way to understand this is to view the group of unitary matrices as complete and thus integration over the whole space does not depend on the starting point of integration. An analogy is the integration of $\cos^2 x$ over a connected interval of length π. The answer clearly does not depend on the starting point of integration. How the Haar invariance is useful is in the fact that one might as well consider the covariance matrix $\boldsymbol{R}$ as diagonal. The required integral, from (4.30), is therefore

$$\begin{aligned} f_{\Lambda_1\Lambda_2}(\lambda_1,\lambda_2) = {} & \frac{(\lambda_1\lambda_2)^{n-2}(\lambda_1-\lambda_2)^2}{2\pi\Gamma(n)\Gamma(n-1)(s_1s_2)^n} \\ & \cdot \int_{-\pi}^{\pi}\int_0^{\pi/2} \sin(2\theta) e^{-\mathrm{Tr}\left(\boldsymbol{U}^\dagger \begin{bmatrix} s_1^{-1} & 0 \\ 0 & s_2^{-1} \end{bmatrix} \boldsymbol{U} \begin{bmatrix} \lambda_1 & 0 \\ 0 & \lambda_2 \end{bmatrix}\right)} \mathrm{d}\theta\mathrm{d}\delta. \end{aligned} \tag{B.32}$$

Expansion of the trace relation yields

$$\mathrm{Tr}\left(U^\dagger \begin{bmatrix} s_1^{-1} & 0 \\ 0 & s_2^{-1} \end{bmatrix} U \begin{bmatrix} \lambda_1 & 0 \\ 0 & \lambda_2 \end{bmatrix}\right) = \left(\frac{\lambda_1}{s_1} + \frac{\lambda_2}{s_2}\right)\cos^2\theta + \left(\frac{\lambda_1}{s_2} + \frac{\lambda_2}{s_1}\right)\sin^2\theta, \tag{B.33}$$

showing that integration over δ is trivial as there are no δ terms. By ignoring the constant part of the integrand for the moment, the θ integral can be written as

$$I = \int_0^{\pi/2} \sin(2\theta) e^{-\left(\frac{\lambda_1}{s_1}+\frac{\lambda_2}{s_2}\right)+\left(\frac{\lambda_1}{s_1}+\frac{\lambda_2}{s_2}-\frac{\lambda_1}{s_2}-\frac{\lambda_2}{s_1}\right)\sin^2\theta} \mathrm{d}\theta, \tag{B.34}$$

and evaluates to

$$\frac{1}{(\lambda_1-\lambda_2)(s_1^{-1}-s_2^{-1})}\left(e^{-\frac{\lambda_1}{s_2}-\frac{\lambda_2}{s_1}} - e^{-\frac{\lambda_1}{s_1}-\frac{\lambda_2}{s_2}}\right). \tag{B.35}$$

After substituting this result back into (B.32), one finds that

$$f_{\Lambda_1\Lambda_2}(\lambda_1,\lambda_2) = \frac{\lambda_1^{n-1}\lambda_2^{n-2} - \lambda_1^{n-2}\lambda_2^{n-1}}{(s_1-s_2)\Gamma(n)\Gamma(n-1)(s_1s_2)^{n-1}}\left[e^{-\frac{\lambda_1}{s_1}-\frac{\lambda_2}{s_2}} - e^{-\frac{\lambda_1}{s_2}-\frac{\lambda_2}{s_1}}\right]. \tag{B.36}$$

The final step in the marginalization is to integrate over one eigenvalue to get the marginal pdf of the other. Let us first integrate over λ_1. The domain is $0 < \lambda_2 \leq \lambda_1 < \infty$. As such, the following will be a typical integral

$$\int_{\lambda_2}^{\infty} \lambda_1^{k-1} e^{-\lambda_1/B} \mathrm{d}\lambda_1 = B^k \Gamma(k, \lambda_2/B), \tag{B.37}$$

where $B > 0$. This integral is called an incomplete gamma function. The result of the integration over λ_1 is

$$\begin{aligned} f_{\Lambda_2}(\lambda_2) = &\frac{(\lambda_2/s_2)^{n-2}e^{-\lambda_2/s_2}\Gamma(n,\lambda_2/s_1)}{\Gamma(n)\Gamma(n-1)(s_1-s_2)}\left(\frac{s_1}{s_2} - \frac{\lambda_2/s_2}{n-1}\right) \\ &- \frac{(\lambda_2/s_1)^{n-2}e^{-\lambda_2/s_1}\Gamma(n,\lambda_2/s_2)}{\Gamma(n)\Gamma(n-1)(s_1-s_2)}\left(\frac{s_2}{s_1} - \frac{\lambda_2/s_1}{n-1}\right). \end{aligned} \tag{B.38}$$

B.6 Marginal joint distribution of the unitary phase and Λ_2

In this section, the marginal joint distribution of Λ_2 and the unitary phase is computed. Given that the unitary transformation contributes a Jacobian of one, the transformation of (4.30) can be expressed as

$$f_{\vartheta\Delta\Lambda_1\Lambda_2}(\vartheta,\delta,\lambda_1,\lambda_2) = \frac{\sin(2\vartheta)}{2\pi\Gamma(n)\Gamma(n-1)(s_1s_2)^n}(\lambda_1\lambda_2)^{n-2}(\lambda_1-\lambda_2)^2 e^{-A\lambda_1-B\lambda_2}, \tag{B.39}$$

where A and B are defined in (B.29). The integral over δ contributes 2π. Consider only the integration over λ_1,

$$f_{\vartheta\Lambda_2}(\vartheta,\lambda_2)=\frac{\sin(2\vartheta)}{\Gamma(n)\Gamma(n-1)(s_1s_2)^n}\int_{\lambda_2}^{\infty}(\lambda_1\lambda_2)^{n-2}(\lambda_1^2-2\lambda_1\lambda_2+\lambda_2^2)e^{-A\lambda_1-B\lambda_2}\mathrm{d}\lambda_1. \tag{B.40}$$

This can be written as

$$f_{\vartheta\Lambda_2}(\vartheta,\lambda_2)=\frac{\sin(2\vartheta)}{\Gamma(n)\Gamma(n-1)(s_1s_2)^n}\lambda_2^{n-2}e^{-B\lambda_2}\left(\lambda_2+\frac{\mathrm{d}}{\mathrm{d}A}\right)^2 I, \tag{B.41}$$

where

$$I=\int_{\lambda_2}^{\infty}\lambda_1^{n-2}e^{-A\lambda_1}\mathrm{d}\lambda_1. \tag{B.42}$$

I can be written in terms of the incomplete gamma function (formula 8.350 in [GR00]) which, in turn, can be written in the form of the degenerate hypergeometric function of the second kind (formula 8.351 in [GR00])

$$I=e^{-A\lambda_2}\lambda_2^{n-1}\Psi(1,n;A\lambda_2). \tag{B.43}$$

Thus, the joint distribution can be written as

$$\begin{aligned}
f_{\vartheta\Lambda_2}(\vartheta,\lambda_2)&=\frac{\sin(2\vartheta)}{\Gamma(n)\Gamma(n-1)(s_1s_2)^n}\lambda_2^{2n-3}e^{-B\lambda_2}(\lambda_2+\frac{\mathrm{d}}{\mathrm{d}A})^2e^{-A\lambda_2}\Psi(1,n;A\lambda_2)\\
&=\frac{\sin(2\vartheta)}{\Gamma(n)\Gamma(n-1)(s_1s_2)^n}\lambda_2^{2n-1}e^{-B\lambda_2}(1+\frac{\mathrm{d}}{\mathrm{d}A\lambda_2})^2e^{-A\lambda_2}\Psi(1,n;A\lambda_2)\\
&=\frac{\sin(2\vartheta)}{\Gamma(n)\Gamma(n-1)(s_1s_2)^n}\lambda_2^{2n-1}e^{-B\lambda_2}(1+\frac{\mathrm{d}}{\mathrm{d}x})^2e^{-x}\Psi(1,n;x)\Big|_{x=A\lambda_2}\\
&=\frac{\sin(2\vartheta)}{\Gamma(n)\Gamma(n-1)(s_1s_2)^n}\lambda_2^{2n-1}e^{-B\lambda_2}e^{-x}\frac{\mathrm{d}^2}{\mathrm{d}x^2}\Psi(1,n;x)\Big|_{x=A\lambda_2}\\
&=\frac{2\sin(2\vartheta)}{\Gamma(n)\Gamma(n-1)(s_1s_2)^n}\lambda_2^{2n-1}e^{-(s_1^{-1}+s_2^{-1})\lambda_2}\Psi(3,n+2;A\lambda_2),
\end{aligned} \tag{B.44}$$

where we have used that

$$\frac{\mathrm{d}}{\mathrm{d}z}\Psi(a,b;z)=-a\Psi(a+1,b+1;z). \tag{B.45}$$

This differentiation formula can be found in [AS70], formula 13.4.22.

B.7 Hyperbolic detector probability distribution

Recall the joint distribution of unitary phase and the second eigenvalue

$$f_{\vartheta\Lambda_2}(\vartheta,\lambda_2)=\frac{2\sin(2\vartheta)}{\Gamma(n)\Gamma(n-1)(s_1s_2)^n}\lambda_2^{2n-1}e^{-(s_1^{-1}+s_2^{-1})\lambda_2}\Psi(3,n+2;A\lambda_2) \tag{B.46}$$

By making the change of variables

$$u = \left(\frac{\cos^2\vartheta}{s_1} + \frac{\sin^2\vartheta}{s_2}\right)\lambda_2, \quad v = \lambda_2. \tag{B.47}$$

The Jacobian introduced by this transformation is given by

$$\frac{\partial(u,v)}{\partial(\lambda_2,\vartheta)} = v\sin 2\vartheta\left|\frac{1}{s_2} - \frac{1}{s_1}\right|, \tag{B.48}$$

therefore the transformed random variables have a joint distribution given by

$$f_{UV}(u,v) = \frac{2}{\Gamma(n)\Gamma(n-1)(s_2^{-1}-s_1^{-1})(s_1s_2)^n}v^{2n-2}e^{-(s_1^{-1}+s_2^{-1})v}\Psi(3,n+2;u). \tag{B.49}$$

The limits for the new random variables now become $s_2u < v < s_1u$ where, by definition, $s_1 > s_2$ and $0 < u < \infty$.

By again using (B.43), integration may be conducted over v with the following result

$$f_U(u) = \frac{2u^{2n-1}\Psi(3,n+2;u)}{\Gamma(n)\Gamma(n-1)(s_1-s_2)}\Big[s_1e^{-u\mathrm{Tr}\boldsymbol{R}/s_1}(s_2/s_1)^n\Psi(1,2n;u\mathrm{Tr}\boldsymbol{R}/s_1) - s_2e^{-u\mathrm{Tr}\boldsymbol{R}/s_2}(s_1/s_2)^n\Psi(1,2n;u\mathrm{Tr}\boldsymbol{R}/s_2)\Big]. \tag{B.50}$$

B.8 Derivation of eigenprojection probability distribution

Recall that the eigenprojection metric is given by

$$m_\perp = s_1[\lambda_1(1-\cos\delta\sin(2\theta))+\lambda_2(1+\cos\delta\sin(2\theta))] - s_2[\lambda_1(1+\cos\delta\sin(2\theta))+\lambda_2(1-\cos\delta\sin(2\theta))]. \tag{B.51}$$

To compute the probability distribution of this metric, we return to the joint probability distribution of eigenvalues and eigenvectors, (4.30). However, before doing so, it behoves the derivation to rewrite (B.51) in terms of the independent unitary phase random variable. To this end, make the substitution:

$$\begin{bmatrix} e^{j\eta_1} & 0 \\ 0 & e^{j\eta_2}\end{bmatrix}\begin{bmatrix}\cos\vartheta & e^{j\varphi}\sin\vartheta \\ e^{-j\varphi}\sin\vartheta & -\cos\vartheta\end{bmatrix} = \frac{1}{\sqrt{2}}\begin{bmatrix}1 & 1\\ 1 & -1\end{bmatrix}\begin{bmatrix}\cos\theta & e^{j\delta}\sin\theta \\ e^{-j\delta}\sin\theta & -\cos\theta\end{bmatrix} \tag{B.52}$$

Expansion of the right side yields

$$\frac{1}{\sqrt{2}}\begin{bmatrix}\cos\theta + e^{-j\delta}\sin\theta & e^{j\delta}\sin\theta - \cos\theta \\ \cos\theta - e^{-j\delta}\sin\theta & e^{j\delta}\sin\theta + \cos\theta\end{bmatrix}, \tag{B.53}$$

and for equality with the left side, we must have that

$$\begin{aligned} 2\cos^2\vartheta &= (\cos\theta + \cos\delta\sin\theta)^2 + (-\sin\theta\sin\delta)^2 \\ &= 1 + \cos\delta\sin(2\theta) \\ \cos(2\vartheta) &= \cos\delta\sin(2\theta). \end{aligned} \tag{B.54}$$

The invariance of the Haar measure ensures that the Jacobian is $\sin(2\vartheta)/\sin(2\theta)$. Equation (4.30) becomes

$$\begin{aligned} f_{\lambda_1,\lambda_2,\vartheta,\varphi}(\lambda_1,\lambda_2,\vartheta,\varphi) = &\frac{\sin(2\vartheta)(\lambda_1\lambda_2)^{n-2}(\lambda_1-\lambda_2)^2}{2\pi\Gamma(n)\Gamma(n-1)(s_1s_2)^n} \\ &\exp\left(\frac{-1}{\sigma^2(1-\rho^2)}\Big[\lambda_1(1-\rho\cos(2\vartheta)) + \lambda_2(1+\rho\cos(2\vartheta))\Big]\right). \end{aligned} \tag{B.55}$$

Since (B.55) does not depend on φ, it can immediately be integrated out leading to a factor of 2π. The metric transforms into

$$m_\perp = s_1[\lambda_1(1-\cos(2\vartheta)) + \lambda_2(1+\cos(2\vartheta))] - s_2[\lambda_1(1+\cos(2\vartheta)) + \lambda_2(1-\cos(2\vartheta))]. \tag{B.56}$$

By making a further transformation

$$u = -\cos 2\vartheta, \tag{B.57}$$

one finds that

$$f_{\lambda_1,\lambda_2,\vartheta}(\lambda_1,\lambda_2,\vartheta) = \frac{(\lambda_1\lambda_2)^{n-2}(\lambda_1-\lambda_2)^2}{2\Gamma(n)\Gamma(n-1)(s_1s_2)^n}\exp\left(\frac{-1}{\sigma^2(1-\rho^2)}\Big[\lambda_1(1+\rho u) + \lambda_2(1-\rho u)\Big]\right), \tag{B.58}$$

and

$$\begin{aligned} m_\perp &= s_1[\lambda_1(1+u) + \lambda_2(1+u)] - s_2[\lambda_1(1-u) + \lambda_2(1+u)] \\ &= 2\sigma^2[(\lambda_1(\rho+u) + \lambda_2(\rho-u)] \end{aligned} \tag{B.59}$$

The next step involves making the following transformation

$$\begin{aligned} m_\perp &= 2\sigma^2[(\lambda_1(\rho+u)+\lambda_2(\rho-u)] \\ \lambda_2 &= \lambda_2 \\ \lambda_1 &= \lambda_1 \end{aligned} \tag{B.60}$$

which produces a Jacobian of

$$\frac{\partial(m_\perp,\lambda_2,\lambda_1)}{\partial(\lambda_1,\lambda_2,u)} = |2\sigma^2(\lambda_1-\lambda_2)|. \tag{B.61}$$

Given that $\lambda_1 > \lambda_2 > 0$, the absolute values bars are unecessary. The probability distribution of the eigenprojection metric is given by the marginal distribution of $m_\perp$. To compute this marginal distribution, one needs to compute the domains of integration for λ_1 and λ_2 which have changed due to the transformation. To this end, consider three possible values of $m_\perp$ fixed. From the first equation in (B.60), one sees that

$$\lambda_1 = \frac{m_\perp}{2\sigma^2(\rho+u)} + \frac{\lambda_2(u-\rho)}{(u+\rho)}. \tag{B.62}$$

For any value of $m_\perp$, a linear relationship exists between λ_1 and λ_2, the slope of which depends on u. As u increases from -1 to 1, for $m_\perp = 0$, it becomes clear that these lines in the $\lambda_1 \times \lambda_2$ plane trace out a fan shape around the origin as illustrated in figure B.1. It is a straightforward matter to show that the intercept of (B.62) and $\lambda_1 = \lambda_2$ is independent of u and given by $\lambda_2 = m_\perp/(4\rho\sigma^2) = m_\perp/(2(s1-s2))$. Thus, for any value of $m_\perp$, the fan shape in figure B.1 opens up on the line $\lambda_1 = \lambda_2$ at the point $\lambda_2 = \lambda_1 = m_\perp/(2(s1-s2))$. It opens in a counter clockwise direction. Recalling that we must have $\lambda_1 > \lambda_2 > 0$ leads to the illustrations of figure B.2 for $m_\perp < 0$ and figure B.3 for $m_\perp > 0$. Clearly, the most complicated integral occurs for $m_\perp > 0$ since it must be split into two parts. The expression for the marginal distribution of $m_\perp$ is given by

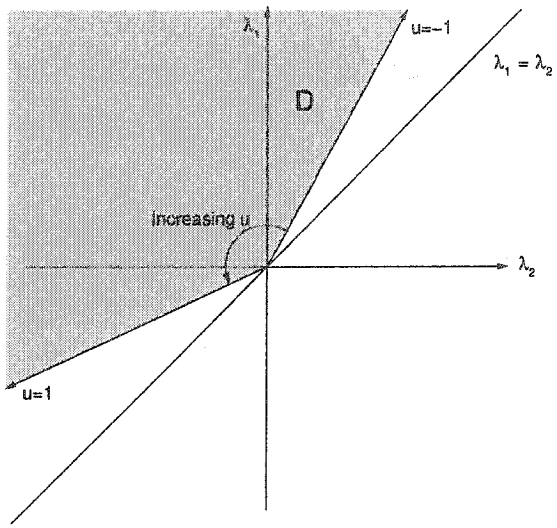

Figure B.1. Domain of integration for λ_1 and λ_2 when $m_\perp = 0$.

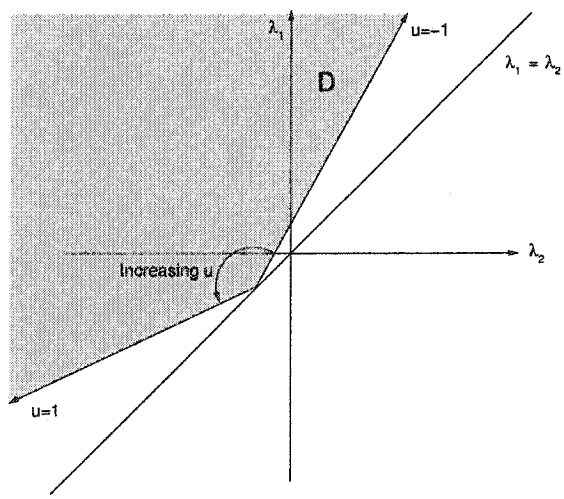

Figure B.2. Domain of integration for λ_1 and λ_2 when $m_\perp < 0$.

$$f_{M_\perp}(m_\perp) = \begin{cases} \displaystyle\int_0^{\infty} \int_{\frac{-m_\perp}{2s_2}+\frac{s_1\lambda_2}{s_2}}^{\infty} f_{\lambda_1,\lambda_2,m_\perp}(\lambda_1,\lambda_2,m_\perp)\mathrm{d}\lambda_1\mathrm{d}\lambda_2 & \text{for } m_\perp \leq 0 \\ \displaystyle\int_0^{\frac{m_\perp}{2(s_1-s_2)}} \int_{\frac{m_\perp}{2s_1}+\frac{s_2\lambda_2}{s_1}}^{\infty} f_{\lambda_1,\lambda_2,m_\perp}(\lambda_1,\lambda_2,m_\perp)\mathrm{d}\lambda_1\mathrm{d}\lambda_2 & \\ + \displaystyle\int_{\frac{m_\perp}{2(s_1-s_2)}}^{\infty} \int_{\frac{-m_\perp}{2s_2}+\frac{s_1\lambda_2}{s_2}}^{\infty} f_{\lambda_1,\lambda_2,m_\perp}(\lambda_1,\lambda_2,m_\perp)\mathrm{d}\lambda_1\mathrm{d}\lambda_2 & \text{for } m_\perp > 0. \end{cases} \tag{B.63}$$

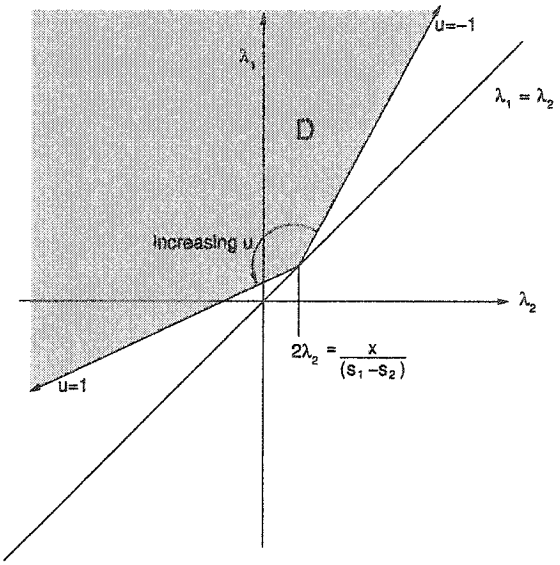

Figure B.3. Domain of integration for λ_1 and λ_2 when $m_\perp > 0$.

where

$$f_{\lambda_1,\lambda_2,m_\perp}(\lambda_1,\lambda_2,m_\perp) = \frac{(\lambda_1\lambda_2)^{n-2}(\lambda_1-\lambda_2)}{4\sigma^2\Gamma(n)\Gamma(n-1)(s_1s_2)^n}\exp\left(-\frac{\lambda_1}{\sigma^2}-\frac{\lambda_2}{\sigma^2}-\frac{m_\perp\rho}{2s_1s_2}\right). \tag{B.64}$$

The probability density function can be re-written in terms of a single integration using the upper incomplete gamma function [GR00]:

$$f_{M_\perp}(m_\perp) = \exp\left(-\frac{m_\perp\rho}{2s_1s_2}\right)\int_0^\infty \frac{e^{-\frac{\lambda_2}{\sigma^2}}\lambda_2^{n-2}\sigma^{2n}}{4\Gamma(n)\Gamma(n-1)(s_1s_2)^n}$$
$$\left[\Gamma\left(n+1,\frac{s_1\lambda_2}{s_2\sigma^2}-\frac{m_\perp}{2s_2\sigma^2}\right)-2\frac{\lambda_2}{\sigma^2}\Gamma\left(n,\frac{s_1\lambda_2}{s_2\sigma^2}-\frac{m_\perp}{2s_2\sigma^2}\right)+\frac{\lambda_2^2}{\sigma^4}\Gamma\left(n-1,\frac{s_1\lambda_2}{s_2\sigma^2}-\frac{m_\perp}{2s_2\sigma^2}\right)\right]\mathrm{d}\lambda_2 \tag{B.65}$$

for $m_\perp \leq 0$ while for $m_\perp > 0$ the distribution function is

$$
\begin{aligned}
f_{M_\perp}(m_\perp) = \exp\left(-\frac{m_\perp \rho}{2s_1 s_2}\right) \int_0^{\frac{m_\perp}{2(s_1-s_2)}} & \frac{e^{-\frac{\lambda_2}{\sigma^2}} \lambda_2^{n-2} \sigma^{2n}}{4\Gamma(n)\Gamma(n-1)(s_1 s_2)^n} \\
& \left[\Gamma\left(n+1, \frac{s_2\lambda_2}{s_1\sigma^2} + \frac{m_\perp}{2s_1\sigma^2}\right) - 2\frac{\lambda_2}{\sigma^2}\Gamma\left(n, \frac{s_2\lambda_2}{s_1\sigma^2} + \frac{m_\perp}{2s_1\sigma^2}\right) + \frac{\lambda_2^2}{\sigma^4}\Gamma\left(n-1, \frac{s_2\lambda_2}{s_1\sigma^2} + \frac{m_\perp}{2s_1\sigma^2}\right)\right] \mathrm{d}\lambda_2 \\
+ \exp\left(-\frac{m_\perp \rho}{2s_1 s_2}\right) \int_{\frac{m_\perp}{2(s_1-s_2)}}^{\infty} & \frac{e^{-\frac{\lambda_2}{\sigma^2}} \lambda_2^{n-2} \sigma^{2n}}{4\Gamma(n)\Gamma(n-1)(s_1 s_2)^n} \\
& \left[\Gamma\left(n+1, \frac{s_1\lambda_2}{s_2\sigma^2} - \frac{m_\perp}{2s_2\sigma^2}\right) - 2\frac{\lambda_2}{\sigma^2}\Gamma\left(n, \frac{s_1\lambda_2}{s_2\sigma^2} - \frac{m_\perp}{2s_2\sigma^2}\right) + \frac{\lambda_2^2}{\sigma^4}\Gamma\left(n-1, \frac{s_1\lambda_2}{s_2\sigma^2} - \frac{m_\perp}{2s_2\sigma^2}\right)\right] \mathrm{d}\lambda_2.
\end{aligned}
\tag{B.66}
$$

APPENDIX C

RECEIVER OPERATING CHARACTERISTICS FOR VARIOUS NUMBER OF LOOKS

The receiver operating characteristics (ROCs) for a range of phases and the number of looks have been computed for the Gaussian target case (Swerling type II). These ROC plots follow. Thresholds were calculated for the three metrics and are listed in table C.1

looks	subtractive DPCA	Λ_2	ATI phase
2	1.1756	0.2245	2.9881
3	0.9285	0.1933	1.8007
4	0.7957	0.1725	0.9657
5	0.7113	0.1581	0.7025
6	0.6522	0.1474	0.5723
7	0.6083	0.1391	0.4919
8	0.5741	0.1325	0.4375
9	0.5465	0.1271	0.3971
10	0.5239	0.1226	0.3648
11	0.5048	0.1187	0.3400
12	0.4884	0.1154	0.3189

Table C.1. Thresholds for the subtractive DPCA metric, the λ_2 metric and the ATI phase metric. $P_F = 10^{-4}$, $\rho = 0.95$, $\sigma^2 = 1$.

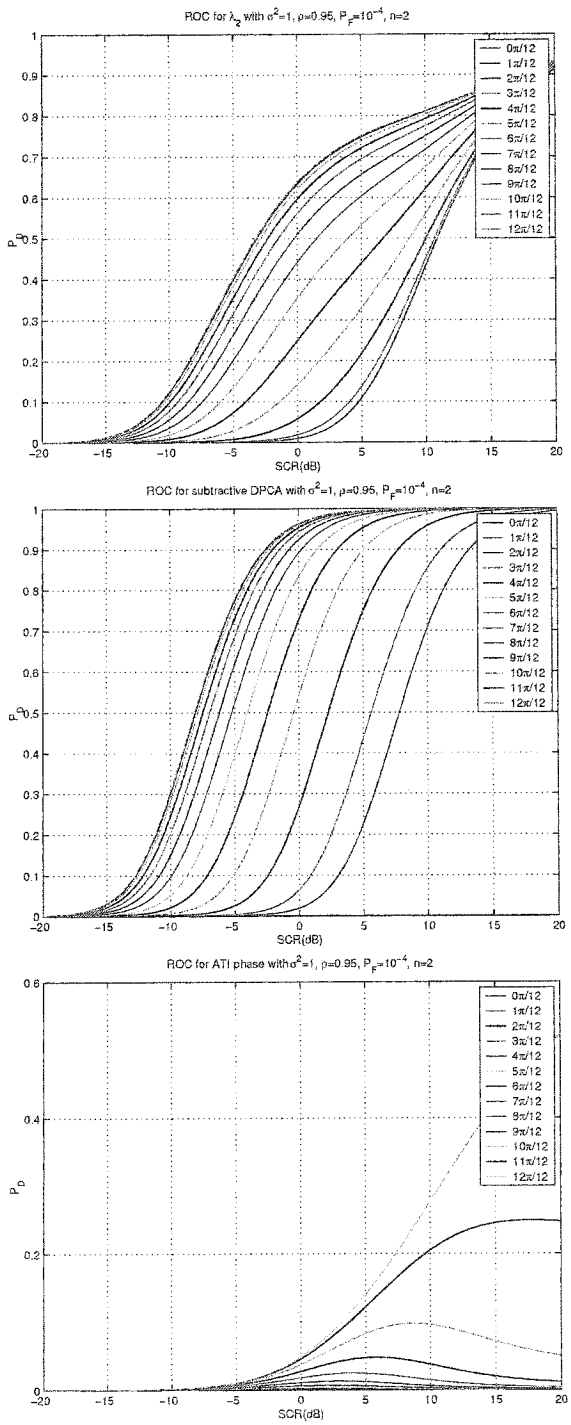

Figure C.1. ROC for Λ_2, subtractive DPCA, and ATI phase for $P_F = 10^{-4}$, $n = 2$.

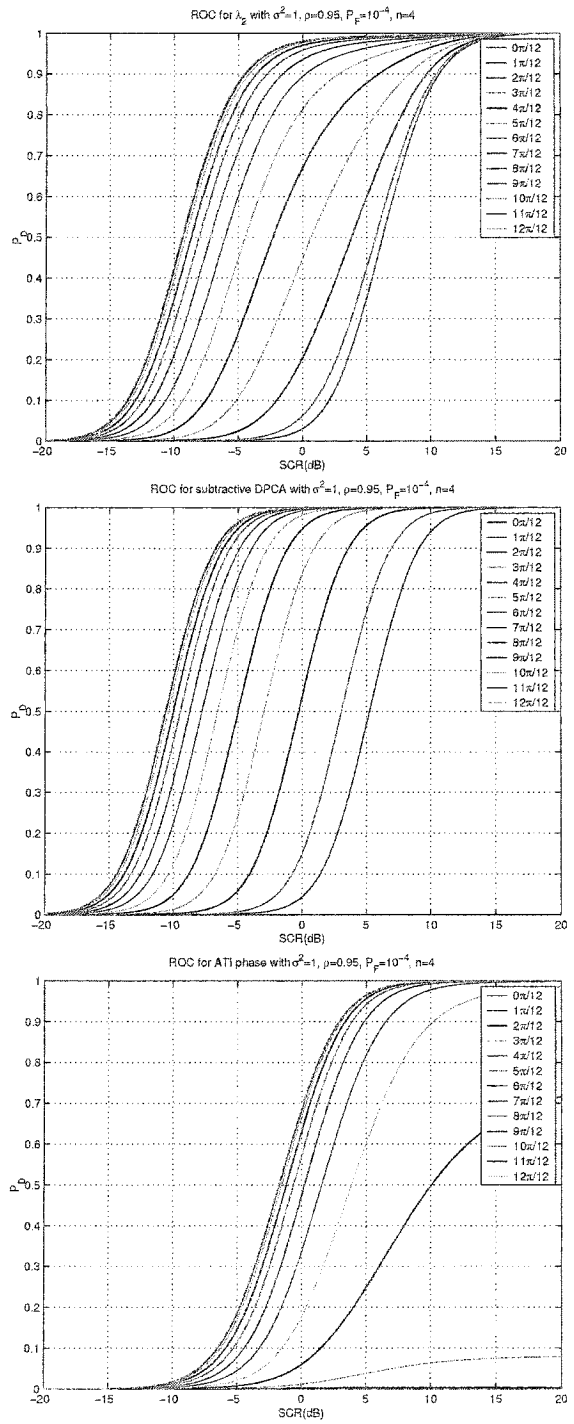

Figure C.2. ROC for A_2, subtractive DPCA, and ATI phase for $P_F = 10^{-4}$, $n = 4$.

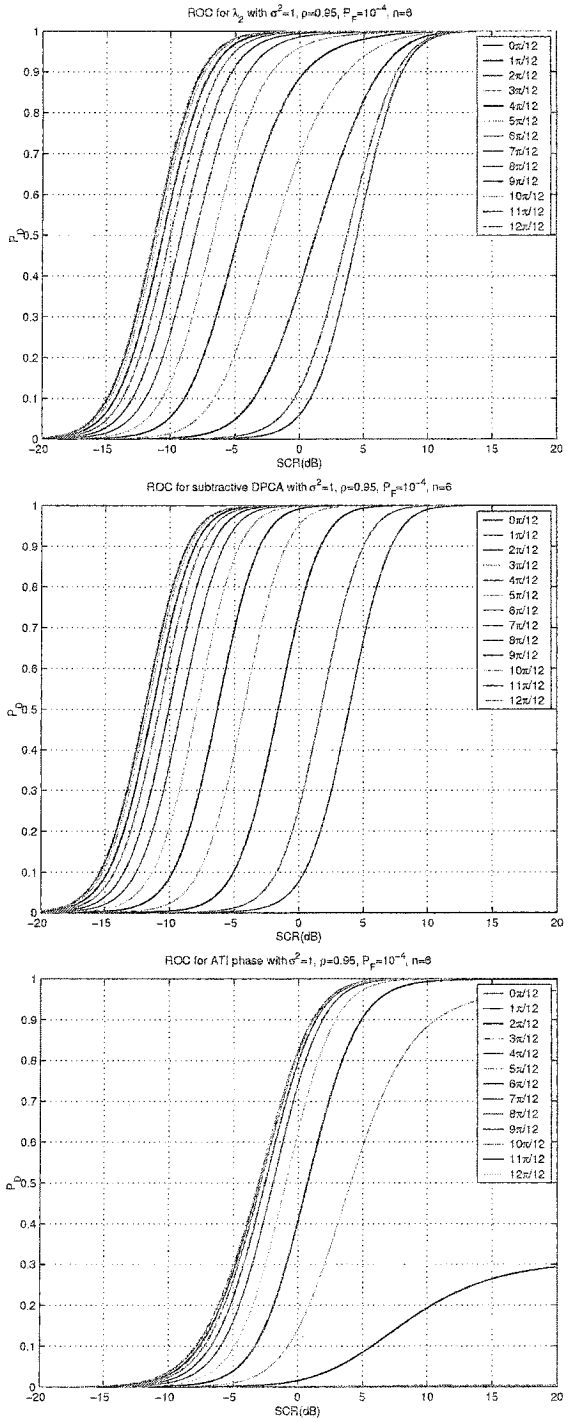

Figure C.3. ROC for Λ_2, subtractive DPCA, and ATI phase for $P_F = 10^{-4}$, $n = 6$.

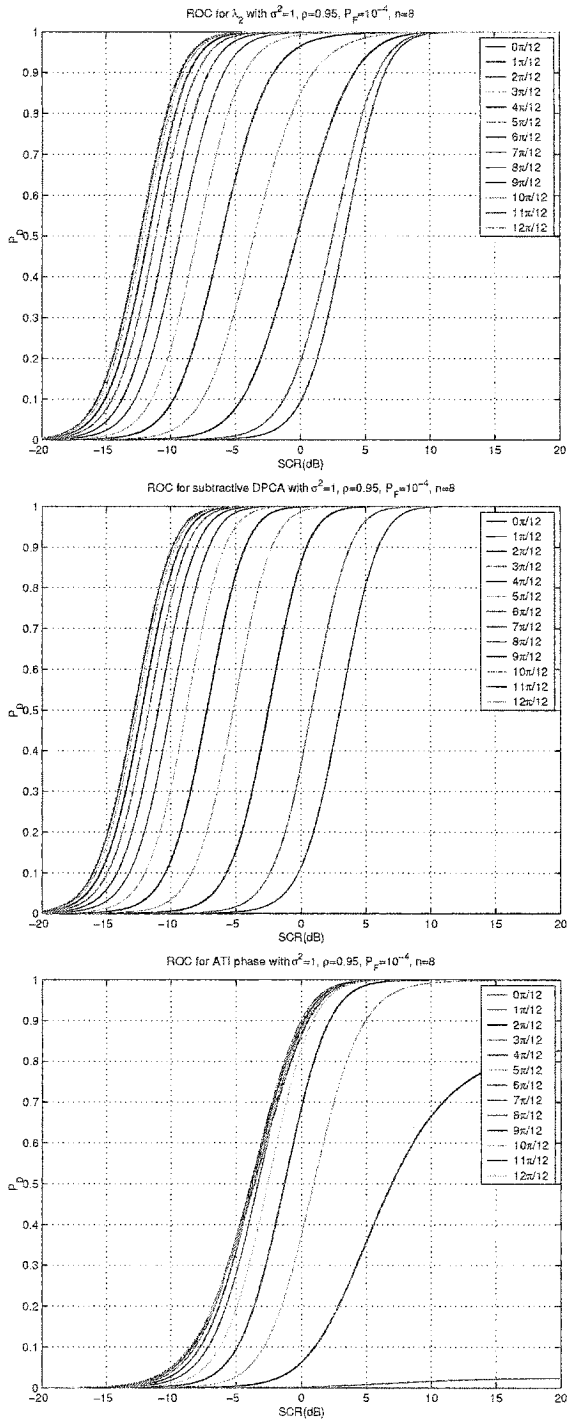

Figure C.4. ROC for Λ_2, subtractive DPCA, and ATI phase for $P_F = 10^{-4}$, $n = 8$.

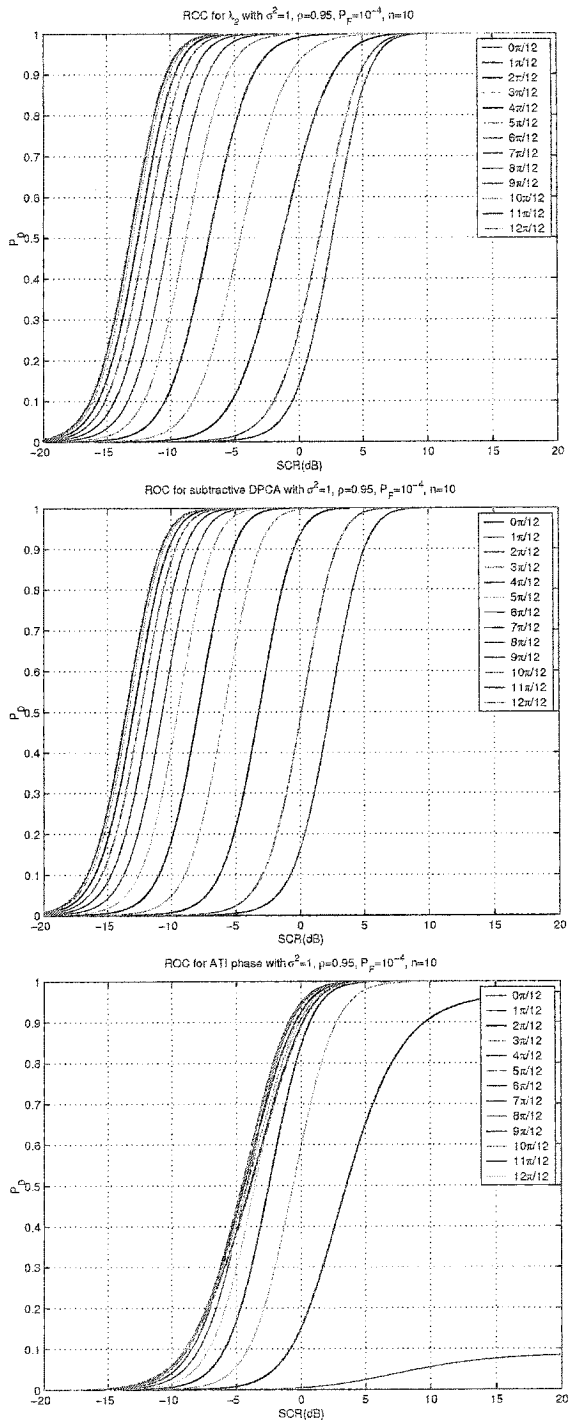

Figure C.5. ROC for Λ_2, subtractive DPCA, and ATI phase for $P_F = 10^{-4}$, $n = 10$.

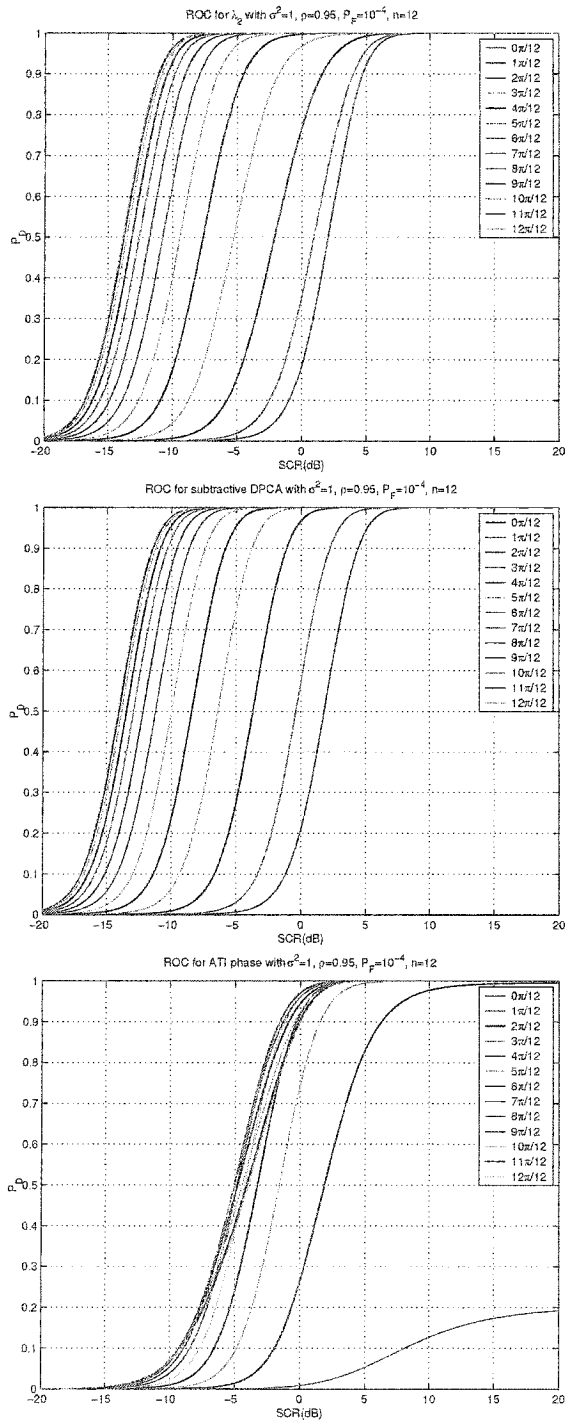

Figure C.6. ROC for Λ_2, subtractive DPCA, and ATI phase for $P_F = 10^{-4}$, $n = 12$.

APPENDIX D

MOMENTS OF $Z = \mathrm{EXP}(J\Psi)$

In this appendix, the moments of the probability distribution function of the complex exponential of the ATI phase are developed.

First rewrite the phase pdf (2.17) as a combined expression. The first term can be written as

$$\frac{\Gamma(n+1/2)(1-\rho^2)^n\beta}{2\sqrt{\pi}\Gamma(n)(1-\beta^2)^{(n+1/2)}} = \frac{(1-\rho^2)^n}{2\sqrt{\pi}}\sum_{l=0}^{\infty}\beta^{2l+1}\frac{\Gamma(n+1/2+l)}{\Gamma(n)\Gamma(l+1)}, \tag{D.1}$$

and the second term can be written as

$$\frac{(1-\rho^2)^n}{2\pi}{}_2F_1(n,1;1/2;\beta^2) = \frac{(1-\rho^2)^n}{2\sqrt{\pi}}\sum_{l=0}^{\infty}\beta^{2l}\frac{\Gamma(n+l)}{\Gamma(n)\Gamma(l+1/2)}. \tag{D.2}$$

Equations (D.1) and (D.2) have very similar form. Indeed,

$$\begin{aligned} f_\Delta(\delta) &= \frac{(1-\rho^2)^n}{2\sqrt{\pi}\Gamma(n)}\left[\sum_{l=0}^{\infty}\beta^{2l}\frac{\Gamma(n+l)}{\Gamma(l+1/2)} + \sum_{l=1/2}^{\infty+1/2}\beta^{2l}\frac{\Gamma(n+l)}{\Gamma(l+1/2)}\right] \\ &= \frac{(1-\rho^2)^n}{2\sqrt{\pi}\Gamma(n)}\sum_{l=0}^{\infty}\beta^{l}\frac{\Gamma(n+l/2)}{\Gamma(\frac{l+1}{2})}. \end{aligned} \tag{D.3}$$

Note that, because of the $\cos\delta$ term in β, the phase pdf is an even function. Furthermore, because the limits of Ψ are $-\pi < \delta \leq \pi$, the first term in (2.17) must integrate to zero (there are two anti-symmetry axis for $\cos\delta$ at $\delta = -\pi/2$ and $\delta = \pi/2$).

The Jacobian introduced by the variable transformation is

$$-j\frac{dz}{z} = d\delta, \tag{D.4}$$

and one can write

$$\cos(\delta) = \frac{1+z^2}{2z}. \tag{D.5}$$

The α^{th} moment of z is given by,

$$I_\alpha = \oint_C \frac{-j(1-\rho^2)^n}{2\sqrt{\pi}\Gamma(n)}\sum_{l=0}^{\infty}\frac{\rho^l\Gamma(n+l/2)}{2^l\Gamma(\frac{l+1}{2})}\frac{z^\alpha(1+z^2)^l}{z^{l+1}}\,dz, \tag{D.6}$$

where the contour of integration, C, is the unit circle as shown in figure D.1. Upon changing the

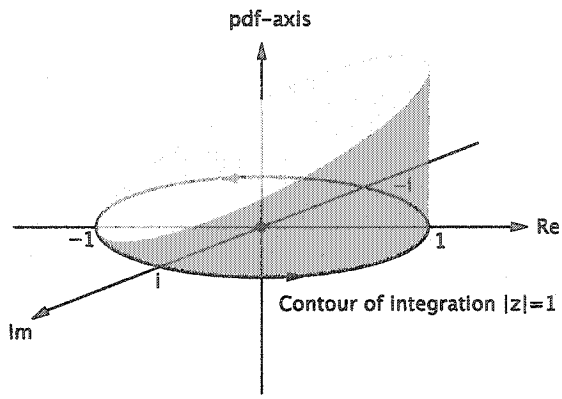

Figure D.1. Contour of integration, pole at $z = 0$, order $l - \alpha + 1$.

order of integration and summation, one must evaluate

$$I_\alpha = \frac{-j(1-\rho^2)^n}{2\sqrt{\pi}\Gamma(n)} \sum_{l=0}^{\infty} \frac{\rho^l \Gamma(n + l/2)}{2^l \Gamma(\frac{l+1}{2})} \oint_C \frac{(1+z^2)^l}{z^{l-\alpha+1}}\, dz. \tag{D.7}$$

A pole of order $l - \alpha + 1$ exists for the integral

$$I = \oint_C \frac{(1+z^2)^l}{z^{l-\alpha+1}}\, dz. \tag{D.8}$$

For $l < \alpha - 1$, the Cauchy integral theorem for analytic functions means that the integral evaluates to zero. For $l > \alpha - 1$, however, the residue of the pole is

$$a_{-1} = \lim_{z \to 0} \frac{1}{\Gamma(l - \alpha + 1)} \frac{d^{l-\alpha}}{dz^{l-\alpha}} \left\{ (1+z^2)^l \right\}. \tag{D.9}$$

A binomial expansion of $(1 + z^2)^l$ leads to

$$a_{-1} = \lim_{z \to 0} \frac{1}{\Gamma(l - \alpha + 1)} \sum_{l=0}^{l} \binom{l}{l} \frac{[2(l-l)]!}{(l + \alpha - 2l)!} z^{l+\alpha-2l}, \tag{D.10}$$

and in the limit $z \to 0$, the only term that survives is $l + \alpha - 2l = 0$. Thus,

$$a_{-1} = \frac{1}{\Gamma(l - \alpha + 1)} \binom{l}{\frac{l+\alpha}{2}} (l + \alpha)! \tag{D.11}$$

Therefore,

$$I = 2\pi j a_1 = \frac{2\pi j \Gamma(l+1)}{\Gamma(\frac{l+\alpha}{2}+1)\Gamma(\frac{l-\alpha}{2}+1)}, \tag{D.12}$$

and,

$$I_\alpha = \frac{(1-\rho^2)^n\sqrt{\pi}}{\Gamma(n)} \sum_{l=\alpha}^{\infty} \frac{\rho^{2l-\alpha}\Gamma(n+l-\alpha/2)\Gamma(2l+1-\alpha)}{2^{2l-\alpha}\Gamma(l+(1-\alpha)/2)\Gamma(l+1)\Gamma(l-\alpha+1)}, \tag{D.13}$$

where the substitution $l = 2l - \alpha$ has been made. Note that the sum must start at $l = \alpha$. By applying [Spi64]

$$2^{2z-1}\Gamma(z+1/2)\Gamma(z) = \sqrt{\pi}\Gamma(2z), \tag{D.14}$$

one obtains,

$$I_\alpha = \frac{(1-\rho^2)^n}{\Gamma(n)} \sum_{l=\alpha}^{\infty} \rho^{2l-\alpha} \frac{\Gamma(n+l-\alpha/2)\Gamma(1+l-\alpha/2)}{\Gamma(l+1)\Gamma(l-\alpha+1)}, \tag{D.15}$$

and, finally, by noting that

$${}_2F_1(a,b;c;z) \equiv 1 + \frac{\Gamma(c)}{\Gamma(a)\Gamma(b)} \sum_{l=1}^{\infty} z^l \frac{\Gamma(a+l)\Gamma(b+l)}{\Gamma(c+l)\Gamma(l+1)}, \tag{D.16}$$

one obtains

$$I_\alpha(n,\rho) = \frac{\Gamma(n+\alpha/2)\Gamma(1+\alpha/2)}{\Gamma(1+\alpha)\Gamma(n)} \rho^\alpha (1-\rho^2)^n {}_2F_1(n+\alpha/2, 1+\alpha/2; 1+\alpha; \rho^2). \tag{D.17}$$

D.1 Special cases

To calculate the higher order moments, the integral representation of the hypergeometric function is used, e.g. [AS70]:

$${}_2F_1(a,b;c;z) = \frac{\Gamma(c)}{\Gamma(b)\Gamma(c-b)} \int_0^1 t^{b-1}(1-t)^{c-b-1}(1-tz)^{-a} dt. \tag{D.18}$$

Alternatively, closed form expressions for the even moments[1] can be computed by repeated application of Gauss' relations for contiguous functions of the form ${}_2F_1(a+m, b+n; c+l; z)$ with integral m, n, l [AS70].

[1] For the even moments $m = 2k, k = 1, 2, 3, \ldots$, all of the coefficients of the hypergeometric function are integers.

D.2 Even multi-look moments

As an illustration, the method shall be outlined with the moment of order four. The required integrations are

$$I = \int_0^1 t^2(1-t)(1-tz)^{-n-2}dt = \int_0^1 t^2(1-tz)^{-n-2}dt - \int_0^1 t^3(1-tz)^{-n-2}dt, \tag{D.19}$$

where each of the two integrals may be evaluated by solving the integration by parts, in some cases, repeatedly. Special care must be taken when doing the integrations to avoid division by zero which can occur for special cases of n. After some algebraic manipulation and recombination, the moment for the particular case $m = 4$ is given by

$$I_4(n,\rho) = \begin{cases} \frac{2(1-\rho^2)(3-\rho^2)}{\rho^4}\ln(1-\rho^2) + \frac{6-5\rho^2}{\rho^2} & \text{if } n = 1, \\ 1 - \frac{4(1-\rho^2)}{\rho^2} - \frac{6(1-\rho^2)^2}{\rho^4}\ln(1-\rho^2) - \frac{2(1-\rho^2)^2}{\rho^2} & \text{if } n = 2, \\ 1 - \frac{4(1-\rho^2)}{\rho^2(n-1)} + \frac{6(1-\rho^2)^2}{\rho^4(n-2)(n-1)} + \frac{(4\rho^2-2n\rho^2-6)(1-\rho^2)^n}{\rho^4(n-2)(n-1)} & \text{elsewhere.} \end{cases} \tag{D.20}$$

Similarly, the moment of order two is given by

$$I_2(n,\rho) = \begin{cases} 1 + \frac{1-\rho^2}{\rho^2}\ln(1-\rho^2) & \text{if } n = 1, \\ \frac{(1-\rho^2)^n + (n\rho^2-1)}{(n-1)\rho^2} & \text{elsewhere.} \end{cases} \tag{D.21}$$

D.3 Expectation of integral odd number of looks

For special cases of odd moments, it is also possible to calculate closed form solutions, e.g. the mean value of Z for integral n. Inserting $m = 1$ into the hypergeometric function in (6.2) and using the differentiation identity [AS70] (p. 557, 15.2.3) yields

$${}_2F_1(n+1/2, 3/2; 2; z) = \frac{\sqrt{z}\Gamma(1/2)}{\Gamma(n+1/2)}\frac{d^n}{dz^n}\left[z^{n-1/2}{}_2F_1(1/2, 3/2; 2; z)\right]. \tag{D.22}$$

Using the integral representation (D.18) and the identity in Gradshteyn [GR00] (p. 263, 3.141, 14), the hypergeometric function on the right hand side can be expressed as

$$\begin{aligned} {}_2F_1(1/2, 3/2; 2; z) &= \frac{\Gamma(2)}{\Gamma(3/2)\Gamma(1/2)} z^{-1/2}\int_0^1 \sqrt{\frac{t}{(t-1)(t-1/z)}}dt \\ &= \frac{4}{\pi z}\left(\mathrm{K}(\sqrt{z}) - \mathrm{E}(\sqrt{z})\right), \end{aligned} \tag{D.23}$$

where $\mathbf{K}(\cdot)$ and $\mathbf{E}(\cdot)$ denote the complete elliptic integrals of the first and the second kind. Using the functional relationships between elliptic integrals of Gradshteyn [GR00] (p. 855, 8.123, 2. and 4.) the n-th derivative of (D.23) can be calculated. As an example, the first derivative is given as

$$\frac{d}{dz}\left[\frac{4}{\pi\sqrt{z}}\left(\mathbf{K}(\sqrt{z})-\mathbf{E}(\sqrt{z})\right)\right]=\frac{2}{\pi z^{3/2}}\left[\frac{\mathbf{E}(\sqrt{z})}{\sqrt{1-z}}-\mathbf{K}(\sqrt{z})\right], \tag{D.24}$$

which leads to the one-look mean value of

$$I_1(1,\rho)=\frac{1}{\rho}\left(\mathbf{E}(\rho)-\left(1-\rho^2\right)\mathbf{K}(\rho)\right). \tag{D.25}$$